MOLECULAR DYNAMICS SIMULATIONS OF METAL ALLOYS: STRUCTURE, THERMODYNAMIC PROPERTIES AND SOLID-LIQUID PHASE TRANSITIONS

A THESIS SUBMITTED TO
THE GRADUATE SCHOOL OF NATURAL AND APPLIED SCIENCES
OF
THE MIDDLE EAST TECHNICAL UNIVERSITY

BY

RAŞİT ÇAKIR

IN PARTIAL FULFILLMENT OF THE REQUIREMENTS FOR THE DEGREE OF

MASTER OF SCIENCE

IN

THE DEPARTMENT OF PHYSICS

January 2001

Approval of the Graduate School of Natural and Applied Sciences.

Prof. Dr. Tayfur Öztürk
Director

I certify that this thesis satisfies all the requirements as a thesis for the degree of Master of Science.

Prof. Dr. Sinan Bilikmen
Head of Department

This is to certify that we have read this thesis and that in our opinion it is fully adequate, in scope and quality, as a thesis for the degree of Master of Science.

Assoc. Prof. Dr. Gülay Dereli
Supervisor

Examining Committee Members

Assoc. Prof. Dr. Gülay Dereli

Prof. Dr. İshak Karakaya

Assoc. Prof. Dr. Demet Gülen

Assoc. Prof. Dr. Raşit Turan

Assoc. Prof. Dr. Bülent Akınoğlu

ABSTRACT

MOLECULAR DYNAMICS SIMULATIONS OF METAL ALLOYS: STRUCTURE, THERMODYNAMIC PROPERTIES AND SOLID-LIQUID PHASE TRANSITIONS

Çakır, Raşit
M.Sc., Department of Physics
Supervisor: Assoc. Prof. Dr. Gülay Dereli

January 2001, 105 pages.

Thermodynamic properties of solid and liquid forms of Ag-Cu, Ag-Pb and Ag-Pd metal alloys are studied for various temperatures and concentrations using the molecular dynamics (MD) algorithms based on constant temperature, constant pressure (TPN) MD method. We have tested the emprical many-body potential of Sutton and Chen in simulations of solid and liquid forms of these fcc metal alloys. From simulations those quantities which can be compared with real experiments are obtained. They include thermodynamical and structural properties. From the thermodynamic properties of solid and liquid forms phase diagrams of these alloys are obtained. Results are compared with experiment whenever possible.

Keywords: Simulation, Molecular Dynamics, Metals, Metal Alloys, Liquid Metals, Thermal Properties, Many Body Potentials and Binary Phase Diagrams.

ÖZ

METAL ALAŞIMLARIN MOLEKÜLER DİNAMİK SİMÜLASYONLARI:
YAPI, TERMODİNAMİK ÖZELLİKLER VE
KATI-SIVI FAZ GEÇİŞİ

Çakır, Raşit
Yüksek Lisans , Fizik Bölümü
Tez Yöneticisi: Assoc. Prof. Dr. Gülay Dereli

Ocak 2001, 105 sayfa.

Katı ve sıvı Ag-Cu, Ag-Pb ve Ag-Pd metal alaşımlarının termodinamik özellikleri çeşitli sıcaklık ve konsantrasyonlarda sabit sıcaklık ve basınçtaki (TPN) moleküler dinamik (MD) metoduna dayanan MD algoritmaları kullanılarak çalışılmıştır. Bu fcc metal alaşımlarının katı ve sıvı haldeki simulasyonlarında Sutton ve Chen'nin deneysel çok cisimler potansiyeli test edilmiştir. Simulasyonlardan gerçek deneyler ile karşılaştırılabilecek değerler elde edilmiştir. Bunlar termodinamik ve yapısal özellikleri içermektedir. Katı ve sıvı haldeki termodinamik özelliklerden bu alaşımların faz diyagramları elde edildi. Sonuçlar mümkün olduğunca deneysel değerlerle karşılaştırılmıştır.

Anahtar Sözcükler: Simulasyon, Moleküler Dinamik, Metaller, Metal Alaşımlar, Sıvı Metaller, Termal Özellikler, Çok Cisimli Potansiyeller ve İkili Faz Diyagramları .

ACKNOWLEDGMENTS

I would like to thank my supervisor, Assoc. Prof. Dr. Gülay Dereli for her valuable guidance and support throughout my work.

Special thanks to Prof. Dr. İshak Karakaya and Prof. Dr. Tahir Çağın for their technical support.

TABLE OF CONTENTS

LIST OF TABLES

LIST OF FIGURES

CHAPTER 1

INTRODUCTION

In any branch of science, most of the researches are done both by using experimental and theoretical techniques. Simulations, which is a new way of doing science, is another alternative in science. Computer simulation is an important research area, complementing the traditional approaches of theory and experiment. Simulation cannot be considered as an experiment because no measurements are done in real systems. Molecular simulations are pure calculation. On the other hand, simulation results are used like experiments, to test theories. It is not sensible to test one theory with another, so simulations offer a new tool. So what is the use of simulations? To understand the properties of physical phenomena, they perform some kind of experiments and also make some theoretical models. But usually the theories may not be compared with the experimental results because there may not be analytical solutions or approximations may not be good enough. For this reason, this theoretical consideration is carried into simulations and the results are compared with the experiments to test the theoretical model. And also, they can be compared with approximation theories to test the correctness of the approximation.

Molecular dynamics (MD) simulation method is a useful method for simulating atomic scale of matter. These methods were originally devised in the

1950's and they began to receive widespread attention in the middle of 1970's, when digital computers become powerful and affordable. With the advances in computational speed and emerging new computational algorithms, development of advanced high performance materials became important. The high performance metallic alloys find use in various segments of materials and chemical industry as catalysts, low weight and high strength structural materials.

In this thesis we have done a computer simulation study on solid and liquid forms of Ag-Pd,Ag-Pb and Ag-Cu systems using a MD algorithm based on extended Hamiltonian formalism ([1]-[17]).

This thesis is organized as follows: In Chapter 2, the introductory descriptions of MD simulation is given. In Chapter 3, many-body potentials in the simulation of fcc metals are discussed along with the potential we have used. In Chapter 4, the idea to get the static properties of the system is briefly explained. Chapter 5 gives MD simulations in different types of ensembles. Phase diagrams and Gibbs free energies are discussed in Chapter 6. In Chapter 7 our simulation results are presented and discussed.

CHAPTER 2

MOLECULAR DYNAMICS

MD simulation are in many respects very similar to real experiments. When we perform a real experiment: i) we prepare a sample of the material we wish to study ii) we connect this sample to a measuring instrument iii) we measure the property of interest during a certain time interval. In order to avoid the statistical noise we average longer and our measurements becomes more accurate. In MD simulation we follow the same approach in the initialization, equilibrium and property runs. First we prepare a sample, that is, we select a model system consisting of N particles and we solve the equations of motions for this system until the properties of the system no longer change with time. This is equilibration of the system. After that we compute the averages of the measured quantities.

MD method computes phase space trajectories of a collection of atoms by solving equations of motion and using these equations calculates the macroscopic properties of physical systems. The calculations are done by setting initial conditions for several hundred particles interacting with some pair potential and restricted to a box with periodic boundaries. It is assumed that time averages of volume energy and number of particles of the simulated fluid are equal to microcanonical ensemble averages of the same properties. In some

cases, it is desirable to perform simulations of a fluid for constant values of temperature and/or pressure or under conditions in which the energy or volume of the fluid can fluctuate. Several books can be found about MD [18], [19], [20], [21].

2.1 Equations of Motion

The classical equations of motion may be written in various ways. Perhaps the most fundamental form is Lagrangian equations of motion:

$$\frac{d}{dt}\left(\frac{\partial L}{\partial \dot{q}_k}\right) - \left(\frac{\partial L}{\partial q_k}\right) = 0 \quad . \tag{2.1}$$

The Lagrangian $L(\mathbf{q}, \dot{\mathbf{q}})$ is defined in terms of kinetic and potential energies

$$L = K - U \quad . \tag{2.2}$$

If we consider a system of atoms with Cartesian coordinates $\vec{\mathbf{r}}_i$

$$L = \sum_i \frac{1}{2} m_i \dot{r}_i^2 - U(r_i) \tag{2.3}$$

so

$$m_i \ddot{\mathbf{r}}_i = \mathbf{F}_i = -\nabla_{\mathbf{r}_i} U \tag{2.4}$$

where m_i is the mass of the atom i and $\mathbf{F}_i$ is the force on that atom.

An alternative formulation of equations of motion is Hamiltonian equations of motion. Hamiltonian is defined by the equation

$$H(\mathbf{p}, \mathbf{q}) = \sum_k \dot{q}_k p_k - L(\mathbf{q}, \dot{\mathbf{q}}) \tag{2.5}$$

where it is assumed that we can write $\dot{\mathbf{q}}$ as a function of the momenta $\mathbf{p}$. Since the potential U is independent of velocity and time this reduces to

$$H(\mathbf{p}, \mathbf{q}) = K(\mathbf{p}) + U(\mathbf{q}) \tag{2.6}$$

and H is automatically equal to the energy. For Cartesian coordinates Hamiltonian's equations become

$$\dot{\mathbf{r}}_i = \mathbf{p_i}/m_i \tag{2.7}$$

$$\dot{\mathbf{p}}_\mathbf{i} = -\nabla_{\mathbf{r_i}} U = \mathbf{F_i} \tag{2.8}$$

Computing the centre of mass trajectories of N particles involves solving either a system of $3N$ second order differential equations (Eq. 2.4) or an equivalent set of $6N$ first order equations (Eq. 2.7 and 2.8) .

2.2 Gear Predictor-Corrector Method

The classical tool for attacking initial value problems are finite-difference methods. These methods replace differentials, such as dx and dt, with finite differences Δx and Δt . They replace differential equations with finite difference equations, and over a small finite time Δt, they assume the rate is constant.

The idea is generally as follows: the positions, velocities and accelerations at initial time t are given and the new positions, velocities and accelerations are going to be obtained for time $t + \Delta t$. The equations are solved step-by-step. The choice of the time interval Δt depends on the method of the solution, but $t + \Delta t$ should be smaller than the typical time taken for a particle to travel its own length.

There are several algorithms designed to integrate the equations of motion. The simplest and the oldest one is the Verlet algorithm [22]. It uses a Taylor expansion of the coordinate of a particle around time t. The estimate of the

new position contains an error that is of order Δt^4 where Δt is the time step of the MD program and the expression for the velocity is accurate to order Δt^2. The accuracy of the trajectories generated with the Verlet algorithm is not impressive. One can mention several algorithms that are equivalent to the Verlet. These are Euler, leapfrog, velocity-Verlet algorithms. Higher order integration schemes includes the predictor-corrector algorithms. In our simulations we have made use of 5th order predictor-corrector integration scheme [18].

In this scheme, the prediction of the positions $\mathbf{r}(t)$, velocities $\mathbf{v}(t)$ and accelerations $\mathbf{a}(t)$, $\mathbf{b}(t)$, $\mathbf{c}(t)$ and $\mathbf{d}(t)$ at time $t+\Delta t$ may be obtained by Taylor expansion about time t. The accelerations $\mathbf{b}(t)$,$\mathbf{c}(t)$ and $\mathbf{d}(t)$ are respectively third, fourth and fifth derivatives of position. We have

$\mathbf{r}^p(t+\Delta t) =$

$$\mathbf{r}(t) + \Delta t\ \mathbf{v}(t) + \frac{1}{2}(\Delta t)^2\mathbf{a}(t) + \frac{1}{6}(\Delta t)^3\mathbf{b}(t) + \frac{1}{24}(\Delta t)^4\mathbf{c}(t) + \frac{1}{120}(\Delta t)^5\mathbf{d}(t) \quad (2.9)$$

$$\mathbf{v}^p(t+\Delta t) = \mathbf{v}(t) + \Delta t\ \mathbf{a}(t) + \frac{1}{2}(\Delta t)^2\mathbf{b}(t) + \frac{1}{6}(\Delta t)^3\mathbf{c}(t) + \frac{1}{24}(\Delta t)^4\mathbf{d}(t) \quad (2.10)$$

$$\mathbf{a}^p(t+\Delta t) = \mathbf{a}(t) + \Delta t\ \mathbf{b}(t) + \frac{1}{2}(\Delta t)^2\mathbf{c}(t) + \frac{1}{6}(\Delta t)^3\mathbf{d}(t) \quad (2.11)$$

$$\mathbf{b}^p(t+\Delta t) = \mathbf{b}(t) + \Delta t\ \mathbf{c}(t) + \frac{1}{2}(\Delta t)^2\mathbf{d}(t) \quad (2.12)$$

$$\mathbf{c}^p(t+\Delta t) = \mathbf{c}(t) + \Delta t\ \mathbf{d}(t) \quad (2.13)$$

$$\mathbf{d}^p(t+\Delta t) = \mathbf{d}(t) \quad (2.14)$$

The superscript 'p' means the predicted values so these values are going to be corrected. An equation like 2.14 will not give the correct trajectories of the

particles as time goes on, because there is no equation of motion. In order to correct these values, the forces at time $t+\Delta t$ are evaluated using the predicted positions. For continuous potential energy function $U(r_{ij})$ that acts between the atoms i and j, the force on each molecule is given by

$$\mathbf{F}_i = -\sum_{i \neq j} \frac{\partial U(r_{ij})}{\partial r_{ij}} \hat{\mathbf{r}}_{ij} \quad . \tag{2.15}$$

And so the correct accelerations $\mathbf{a}^c(t+\Delta t)$ are calculated from the new positions $\mathbf{r}^p$. The correct acceleration $\mathbf{a}^c$ is compared with the predicted one $\mathbf{a}^p$ to see the size of error:

$$\delta\mathbf{a}(t+\Delta t) = \mathbf{a}^c(t+\Delta t) - \mathbf{a}^p(t+\Delta t) \tag{2.16}$$

Using these errors, the results of the predictor step go into the corrector step:

$$\mathbf{r}^c(t+\Delta t) = \mathbf{r}^p(t+\Delta t) + c_0\delta\mathbf{a}(t+\Delta t) \tag{2.17}$$

$$\mathbf{v}^c(t+\Delta t) = \mathbf{v}^p(t+\Delta t) + c_1\delta\mathbf{a}(t+\Delta t) \tag{2.18}$$

$$\mathbf{a}^c(t+\Delta t) = \mathbf{a}^p(t+\Delta t) + c_2\delta\mathbf{a}(t+\Delta t) \tag{2.19}$$

$$\mathbf{b}^c(t+\Delta t) = \mathbf{b}^p(t+\Delta t) + c_3\delta\mathbf{a}(t+\Delta t) \tag{2.20}$$

$$\mathbf{c}^c(t+\Delta t) = \mathbf{c}^p(t+\Delta t) + c_4\delta\mathbf{a}(t+\Delta t) \tag{2.21}$$

$$\mathbf{d}^c(t+\Delta t) = \mathbf{d}^p(t+\Delta t) + c_5\delta\mathbf{a}(t+\Delta t) \tag{2.22}$$

The values $\mathbf{r}^c$, $\mathbf{v}^c$, $\mathbf{a}^c$, $\mathbf{b}^c$, $\mathbf{c}^c$, and $\mathbf{d}^c$ for each atom are now better approximations to the true values. The best choice for the coefficients c_0, c_1, c_2, c_3,

c_4 and c_5 are evaluated for optimum stability and accuracy of the trajectories (Table 2.1). Depending on the order of the derivatives in the series, different values of the coefficients are required. The coefficients also depend upon the order of the differential equation being solved. Here it is second order because the second order time derivative of position, **a**, is being compared with the acceleration computed from the forces.

The simple predictor-corrector algorithm can be summarized as follows:

a. Prediction of the positions, velocities and accelerations at time $t + \Delta t$ from the values of these quantities at time t

b. Evaluation of forces and accelerations $\mathbf{a}_i = \mathbf{F}_i/m_i$, from the new positions.

c. Correcting the predicted positions, velocities and accelerations using the new accelerations.

Table 2.1: Gear predictor-corrector coefficients for a second order equation.

order	c_0	c_1	c_2	c_3	c_4	c_5
3	1/6	5/6	1	1/3	-	-
4	19/120	3/4	1	1/2	1/2	-
5	3/20	251/360	1	11/18	1/6	1/60

The last two steps of evaluation and correction can be repeated to any required order to get much better results but usually one step is enough. Since evaluation of forces is the most time consuming part in the simulations, this is rarely done.

Using these types of algorithms, the values and time dependence of the positions and velocities of every atom are found and these give us a trajectory in the $6N$ dimensional phase space. This trajectory is used to evaluate the

bulk properties of the system.

2.3 Periodic Boundary Conditions

In systems of macroscopic size, only a very small fraction of the atoms is close enough to a wall to experience any deviation from the environment. Consider, for example, a three-dimensional system with $N = 10^{21}$ at liquid density. Since the number of atoms near the walls is of the order $N^{2/3}$, This amounts to 10^{14} atoms, ie. only one atom for 10^7. But for a more typical MD value, for example, in our simulation $N = 500$ atoms in a cubicle system, roughly 378 atoms are immediately adjacent to a wall, leaving very few interior atoms. Thus the simulation will fail to capture the typical state of an interior atom and the measurements will reflect this fact. Unless the goal is the study of behaviour near real walls, a problem that is actually of considerable importance, walls are best eliminated.

A system that is bounded but free of physical walls can be constructed by resorting to periodic boundary conditions, shown schematically in Figure 2.1 for a two dimensional system. The introduction of periodic boundaries is equivalent to considering an infinite space-filling array of identical copies of the simulation region. There are two consequences of this periodicity. The first is that an atom that leaves the simulation region through a particular bounding face immediately reenters the region through the opposite face so the number of atoms is kept constant. The second is that atoms lying within a distance r_c of a boundary interact with atoms near the opposite boundary - a wraparound effect. In this way it is possible to model systems that are effectively bounded

but that are nevertheless spatially homogeneous in so far as boundaries are concerned.

The wraparound effect of the periodic boundaries must be taken into account in both the evaluation of the equations of motion and the interaction computations. After each evaluation step the coordinates must be examined. If an atom is found to have moved outside the region its coordinates must be adjusted to bring it back inside. If, for example, the x coordinate is defined to lie between $-L_x/2$ and $L_x/2$, where L_x is the region size in the x coordination, the tests are: if $r_{x_i} \geq L_x/2$ then replace r_{x_i} by $r_{x_i} - L_x$ and if $r_{x_i} \leq L_x/2$ then replace it by $r_{x_i} + L_x$ [20].

The calculation of potential energy of a particular configuration and the forces acting on all atoms are the essential steps of MD programs. When the force acting on atom 1 (Figure 2.1), for example, is going to be calculated, the interaction between atom 1 and every other atoms in the simulation box must be calculated. However, in principle, all interactions between atom 1 and image particles must also be included. These become infinite numbers of terms impossible to calculate. In this case, the largest contributions to the potential and forces came from neighbors close to the atom of interest (in this case from particles 2, 3 and 4) and a spherical cut-off is applied. The dashed circle in the Figure 2.1 represents a cut-off distance r_c in simulation box. The cutoff distance must not be greater than half of the length of the box.

Our MD simulations started from a cubic box with 500 atoms subject to periodic boundary conditions. There are 5 fcc lattices in each x, y and z directions. The system totally has 125 lattice cells and each fcc lattice cell

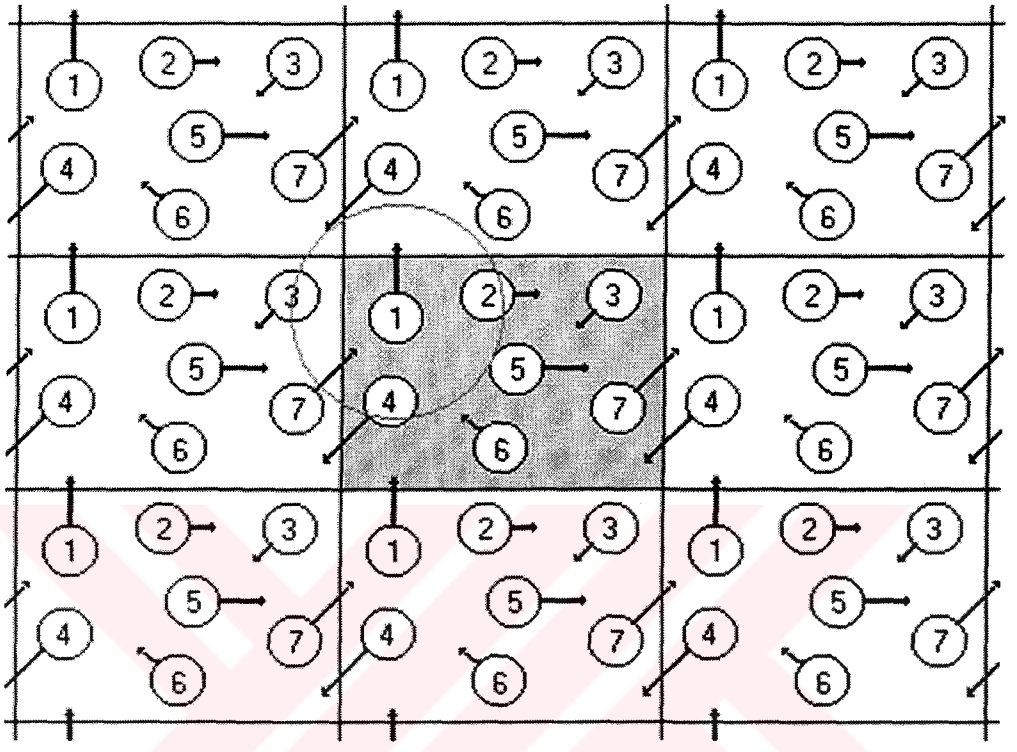

Figure 2.1: Periodic boundary condition for two dimensional case.

has 4 atoms. The cut-off distance for the interactions is taken as 2 lattice parameters.

CHAPTER 3

SUTTON-CHEN POTENTIAL

The most elementary microscopic model for a substance that can exist in any of the three states of the matter is based on spherical particles that interact with one another. The interaction occurs between pairs of atoms. The atoms must attract each other over a range of separation to bind the atoms in the solid and liquid states and also for resistance to compression, the interaction must be repulsive at close range. Potential function having these characteristics can adopt a variety of forms and, when chosen carefully, provides a useful model for real substances.

Computer simulations on various model systems usually use simple pair potentials. However, the interactions in metals and metal alloys cannot be represented by simple pairwise interactions. In these systems electron density plays a dominant role in the interaction and resulting physical properties. Therefore interactions in metals and metal alloys are dominated by many-body interactions [23]. The many-body potential developed by Sutton and co-workers [24], [25] for fcc transition metals has been used in our simulations. The Sutton-Chen interaction potential is given as the sum of pairwise repulsion terms and a many-body density dependent cohesion term. The functional form

of the potential for pure metals is as follows:

$$U = \sum_i U_i \tag{3.1}$$

$$U_i = \epsilon \left(\frac{1}{2} \sum_{j \neq i} U(r_{ij}) - c\rho_i \right) \tag{3.2}$$

$$U(r_{ij}) = \left(\frac{a}{r_{ij}} \right)^n \tag{3.3}$$

$$\rho_i = \left(\sum_{i \neq j} \phi(r_{ij}) \right)^{1/2} \tag{3.4}$$

$$\phi(r_{ij}) = \left(\frac{a}{r_{ij}} \right)^m \tag{3.5}$$

where the Sutton-Chen potential parameters ϵ, c, m and n are optimized to fit the cohesive energy, zero pressure and bulk modules of fcc metals [24]. These parameters are listed in Table 3.1.

Table 3.1: Sutton-Chen potential parameters for Ag, Cu, Pd and Pb computed for a cutoff radius of 2 lattice parameters.

	atom no	$a(\mathring{A})$	$\epsilon(10^{-2}eV)$	c	m	n
Ag	47	4.0856	0.25415	145.658	6	12
Cu	29	3.6153	1.23860	39.755	6	9
Pd	46	3.8902	0.41790	108.526	7	12
Pb	82	4.9495	0.55772	45.882	7	10

Equations 3.1 to 3.5 can be generalized to describe binary $A - B$ alloys. If we consider the interactions of A with A, B with B, A with B and B with A, then

$$U_i = \frac{1}{2} \sum_{j \neq i} \hat{p}_i \hat{p}_j U^{AA}(r_{ij}) + \frac{1}{2} \sum_{j \neq i} (1 - \hat{p}_i) \hat{p}_j U^{BA}(r_{ij}) \tag{3.6}$$

$$+\frac{1}{2}\sum_{j\neq i}\hat{p}_i(1-\hat{p}_j)U^{AB}(r_{ij})+\frac{1}{2}\sum_{j\neq i}(1-\hat{p}_i)(1-\hat{p}_j)U^{BB}(r_{ij})$$

$$-d^{AA}\left(\sum_{j\neq i}\hat{p}_i\hat{p}_j\phi^{AA}(r_{ij})\right)^{1/2}-d^{BA}\left(\sum_{j\neq i}(1-\hat{p}_i)\hat{p}_j\phi^{BA}(r_{ij})\right)^{1/2}$$

$$-d^{AB}\left(\sum_{j\neq i}\hat{p}_i(1-\hat{p}_j)\phi^{AB}(r_{ij})\right)^{1/2}-d^{BB}\left(\sum_{j\neq i}(1-\hat{p}_i)(1-\hat{p}_j)\phi^{BB}(r_{ij})\right)^{1/2}$$

The side occupancy operator $\hat{p}_i$ is defined as follows:

$$\hat{p}_i=\begin{cases}1 & \text{if site } i \text{ is occupied by an atom A}\\ 0 & \text{if site } i \text{ is occupied by an atom B}\end{cases} \tag{3.7}$$

The potentials defined as follows:

$U^{AA}=\epsilon^{AA}\left(\frac{a^{AA}}{r}\right)^{n^{AA}}$, $U^{BB}=\epsilon^{BB}\left(\frac{a^{BB}}{r}\right)^{n^{BB}}$, $U^{AB}=U^{BA}=\epsilon^{AB}\left(\frac{a^{AB}}{r}\right)^{n^{AB}}$,

$\phi(r)^{AA}=\left(\frac{a^{AA}}{r}\right)^{m^{AA}}$, $\phi(r)^{BB}=\left(\frac{a^{BB}}{r}\right)^{m^{BB}}$, $\phi(r)^{AB}=\phi(r)^{BA}=\left(\frac{a^{AB}}{r}\right)^{m^{AB}}$.

The constants ϵ^{AA}, a^{AA}, m^{AA} and n^{AA} are equated with the parameters ϵ, a, m and n of the pure metal A. Similarly, ϵ^{BB}, a^{BB}, m^{BB} and n^{BB} are equated with the parameters ϵ, a, m and n of the pure metal B. The remaining constants are: $\epsilon^{AB}=(\epsilon^{AA}\epsilon^{BB})^{1/2}$, $a^{AB}=(a^{AA}a^{BB})^{1/2}$, $m^{AB}=\frac{1}{2}(m^{AA}+m^{BB})$, $n^{AB}=\frac{1}{2}(n^{AA}+n^{BB})$. Finally, $d^{AA}=\epsilon^{AA}c^{AA}$, $d^{BB}=\epsilon^{BB}c^{BB}$ and $d^{AB}=d^{BA}=(d^{AA}d^{BB})^{1/2}$, where c^{AA} and c^{BB} are the constant c of metal A and B respectively. These assumptions on the constants and potentials are made on purely empirical grounds.

CHAPTER 4

STATIC PROPERTIES

The analysis of the computed trajectories involves evaluating macroscopic properties. These properties are thermodynamic properties and the static structure of the system. Thermodynamic quantities are divided into three classes: simple functions of the Hamiltonian, thermodynamic response functions, which are derivatives of simple functions, and entropy and free energies. The simple functions, internal energy, temperature, pressure and enthalpy will be discussed since these are obtained in the simulations. Also static structure will be explained.

For a system of N particles the phase space point in time step k is represented as $[\mathbf{r}^N(k\Delta t), \mathbf{p}^N(k\Delta t)]$, $k = 1, ..., M$, where $\mathbf{r}^N$ is the set of N position vectors and $\mathbf{p}^N$ is the set of N momentum vectors. The trajectory has been obtained from a simulation performed over M discrete times using the time step Δt. From this, trajectory time average $\langle A \rangle$ of some function of the trajectory can be estimated by the sum

$$\langle A \rangle = \frac{1}{M} \sum_{k=1}^{M} A[\mathbf{r}^N(k\Delta t), \mathbf{p}^N(k\Delta t)] \quad . \tag{4.1}$$

The instantaneous value $A[\mathbf{r}^N(k\Delta t), \mathbf{p}^N(k\Delta t)]$ is the average of the values of each particle. The finite time interval is an approximation to the infinite time average so the summation is used rather than integral over time.

4.1 Internal Energy and Temperature

For an isolated system (EVN ensemble), the total internal energy E is just the Hamiltonian $\mathcal{H}$,

$$E = \mathcal{H}(\mathbf{r}^N, \mathbf{p}^N) = \text{constant} \tag{4.2}$$

which divides into a kinetic part E_k and a configurational part U,

$$E = E_k + U \quad . \tag{4.3}$$

From the kinetic theory [26], the average kinetic energy is proportional to the absolute temperature

$$\langle E_k \rangle = \frac{3}{2} N k_B T \tag{4.4}$$

where k_B is the Boltzmann constant. It is convenient to define an instantaneous kinetic temperature function

$$\mathcal{T} = \frac{1}{3Nk_B} \sum_{i=1}^{N} \frac{1}{m_i} |\mathbf{p}_i|^2 \tag{4.5}$$

so the average temperature

$$T = \langle \mathcal{T} \rangle = \frac{1}{3Nk_B} \frac{1}{M} \sum_{k=1}^{M} \sum_{i=1}^{N} \frac{1}{m_i} |\mathbf{p}_i(k\Delta t)|^2 \tag{4.6}$$

The configurational internal energy is the average of pair potential functions

$$U_c = \langle U \rangle = \frac{1}{M} \sum_{k=1}^{M} \left(\sum_i \sum_{j>i} U[r_{ij}(k\Delta t)] \right) \tag{4.7}$$

4.2 Pressure

The ideal gas contribution to the pressure is

$$P^{id} = \rho k_B T \tag{4.8}$$

where $\rho = N/V$ is the number density. This part of pressure is determined from the atomic motion using Eq. 4.4 and Eq. 4.6:

$$P^{id} = \frac{1}{3V}\left[\frac{1}{M}\sum_{k=1}^{M}\sum_{i=1}^{N}\frac{1}{m_i}|\mathbf{p}_i(k\Delta t)|^2\right] = \frac{2}{3V}\langle E_k\rangle \quad . \tag{4.9}$$

From the intermolecular forces, assuming a pairwise additive potential $U(r)$, the pressure P_f should be calculated to find the total pressure $P = P^{id} + P_f$. If we consider the energy due to intermolecular forces, $\frac{1}{2}r_{ij}F_{ij}$, (the indices i and j are equivalent) the pressure P_f is

$$P_f = \frac{1}{3V}\sum_i\sum_{j>i} r_{ij}F_{ij} = -\frac{1}{3V}\left\langle\sum_i\sum_{j>i} r_{ij}\frac{dU(r_{ij})}{dr_{ij}}\right\rangle \quad , \tag{4.10}$$

so defining instantaneous pressure $\mathcal{P}$

$$\mathcal{P} = \rho k_B\mathcal{T} - \frac{1}{3V}\left\langle\sum_i\sum_{j>i} r_{ij}\frac{dU(r_{ij})}{dr_{ij}}\right\rangle \quad . \tag{4.11}$$

The average pressure $P = \langle\mathcal{P}\rangle$ can be calculated from the phase space trajectory via

$$\frac{P}{\rho k_B T} = 1 - \frac{1}{3MNk_BT}\sum_{k=1}^{M}\left[\sum_i\sum_{j>i} r_{ij}(k\Delta t)\frac{dU[r_{ij}(k\Delta t)]}{dr_{ij}(k\Delta t)}\right] \tag{4.12}$$

4.3 Enthalpy

The enthalpy of a system at constant pressure is defined by

$$H = E + PV \quad . \tag{4.13}$$

For a closed system undergoing a change of state, at constant pressure P, from the state 1 to the state 2, the first law of thermodynamics gives

$$U_2 - U_1 = q_P - P(V_2 - V_1) \tag{4.14}$$

from which

$$(U_2 + PV_2) - (U_1 + PV_1) = q_P \quad , \tag{4.15}$$

therefore

$$\Delta H = H_2 - H_1 = q_P \tag{4.16}$$

where q_P is the heat entering or leaving the system.

Thus, in the case of an isobaric process in a closed system the heat exchanged with the surroundings is equal to the change in enthalpy of the system. For this reason enthalpy is an important state function in applied thermodynamics. H is a state function and for a closed system described by

$$H = H(P,T) \; , \qquad dH = \left(\frac{\partial H}{\partial P}\right)_T dP + \left(\frac{\partial H}{\partial T}\right)_P dT \quad . \tag{4.17}$$

Although the enthalpy is dependent on pressure and temperature, the pressure dependency of H for substances occurring in condensed phases is normally small enough to be neglected in most applications which involve pressure variation in the range of 0 to 1 atmosphere.

In our simulations, the volume change is so small that $P\Delta V$ has a small value with respect to ΔE so it is assumed that enthalpy change is approximately equal to the total internal energy change.

$$\Delta H = \Delta E + P\Delta V \simeq \Delta E \quad . \tag{4.18}$$

4.4 Static Structure

The radial distribution function $g(r)$ measures how atoms organize themselves around one another . It gives local structure of the system at equilibrium. Specifically, it is proportional to the probability of finding two atoms

separated by distance $r \pm \Delta r$. Since MD provides positions of individual atoms as functions of time, $g(r)$ can be readily computed from MD trajectories.

The radial distribution function is defined by [26]

$$\rho\, g(\mathbf{r}) = \frac{1}{N} \left\langle \sum_{i}^{N} \sum_{j \neq i}^{N} \delta[\mathbf{r} - \mathbf{r}_{ij}] \right\rangle \tag{4.19}$$

where the angular brackets represents time average. For homogeneous uniform substances, the structural arrangement of atoms depends only on the distance r between atoms and is independent of the orientation of the separation vector r. Furthermore the double sum contains $N(N-1)$ terms but the distance r_{ij} is invariant under interchange of labels i and j, so only $\frac{1}{2}N(N-1)$ of those terms are independent. Therefore Eq. 4.19 can be written as

$$\rho\, g(r) = \frac{2}{N} \left\langle \sum_{i}^{N} \sum_{j>i}^{N} \delta[r - r_{ij}] \right\rangle \quad . \tag{4.20}$$

The normalization of $g(r)$ is obtained by integrating over all possible separations of two atoms

$$\rho \int g(r) d\mathbf{r} = \frac{2}{N} \left\langle \sum_{i}^{N} \sum_{j>i}^{N} \int \delta[r - r_{ij}] d\mathbf{r} \right\rangle \tag{4.21}$$

The normalization condition of δ-symbol is

$$\int \delta[r - r_{ij}] d\mathbf{r} = 1 \tag{4.22}$$

so Eq. 4.21 reduces to

$$\rho \int g(r) d\mathbf{r} = \frac{2}{N} \sum_{i}^{N} \sum_{j>i}^{N} 1 = \frac{2}{N} \frac{1}{2} N(N-1) = N - 1 \tag{4.23}$$

Eq.4.23 simply says that if we sit on one atom and count the atoms in the system, we find $N-1$ other atoms.

For separations less than about one atomic diameter, $g(r) = 0$. For large separations in fluids, one atom should have no influence on the positions of another, the density will then be uniform and $g(r) = 1$.

The shape of radial distribution function depends on temperature, and therefore, in computer simulation studies, $g(r)$ serves as a helpful indicator of the nature of the phase assumed by the simulated system. For atoms frozen onto the sites of regular crystal at 0K lattice structures -such as fcc, bcc, hcp- $g(r)$ takes the form of sequence of delta symbols. Since regular crystalline solids are periodically repeating structures, the one dimensional quantity $g(r)$ is sufficient to discriminate among various three dimensional structures. If the atoms are vibrating rather than fixed to the lattice sites, then the delta symbols in $g(r)$ resolve into Gaussians but the positions and relative heights of those Gaussian distributions still allow determination of the crystalline structure.

The behaviour of $g(r)$ in crystalline solids is very different from that for gases at low density. In a gas, atoms move freely throughout the container and only weak local structures form around any one atom. Therefore after the first peak $g(r)$ exponentially decays to unity at larger distances.

For liquids the behaviour of $g(r)$ is intermediate between those of a solid and a gas. Liquids show short-range order similar to that in solids but no long range order like that in gases.

For simulations near liquid-solid phase boundaries, the behaviour of $g(r)$ can be used to help identify the phase of the simulated system. For crystalline solids, $g(r)$ contains deeper valleys and higher narrower peaks (particularly after the first peak) than does $g(r)$ for liquids. In addition, for a partially

crystallized substance, $g(r)$ can contain secondary peaks not found in $g(r)$ for a liquid.

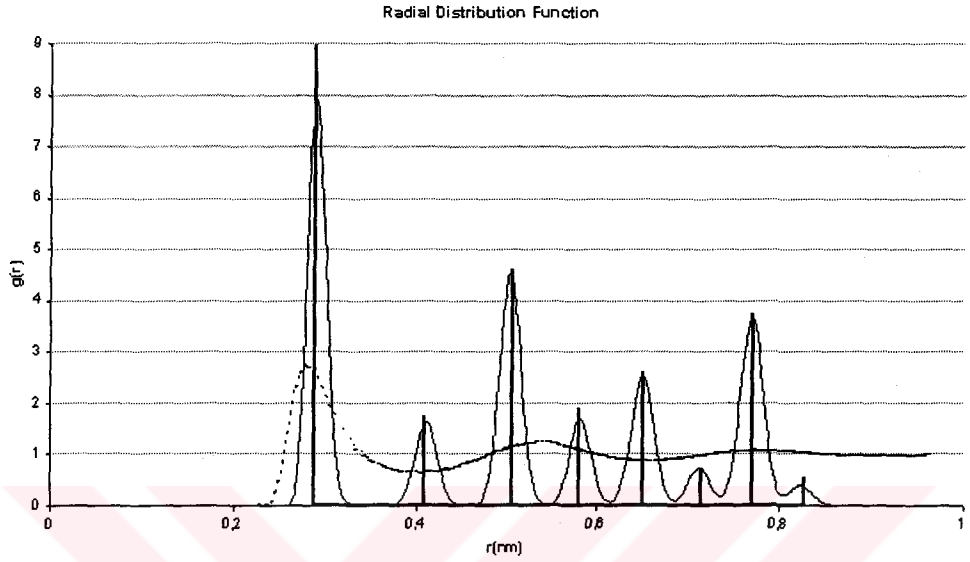

Figure 4.1: Radial distribution function for solid and liquid phase. The delta functions represent fixed atoms at lattice points.

CHAPTER 5

ENSEMBLES

5.1 Microcanonical Ensemble

A system under the constrains of fixed energy E, volume V and number of particles N defines an isolated system. The ensemble corresponding to this system is called a *microcanonical ensemble* or *EVN ensemble.*

In statistical mechanics the probability density for the microcanonical ensemble is proportional to $\delta(\mathcal{H}(p,q) - E)$. The quantity Q_{EVN} is the total number of microstates satisfying the given constrains and is given by

$$Q_{EVN} = \frac{1}{N!}\frac{1}{h^{3N}}\int_{6N} dp^{3N}dq^{3N}\delta(\mathcal{H}(p,q) - E) \quad . \tag{5.1}$$

Here the integration is over all $6N$ dimensional phase space and the integral is the volume of constant energy surface E. Microcanonical ensemble is the cloud of points on this surface. Considering the smallest possible volume in the $q^{3N}p^{3N}$ phase space as h^{3N}, because of the uncertainty principle, and the indistinguishable of the phase points, Eqn. 5.1 gives the total number of microstates of particles for a given macrostates with constant E, V and N values [27].

The quantity Q_{EVN} is related to physical properties by using the well known formula

$$S = k_B \ln Q_{EVN} \tag{5.2}$$

and the other properties obtained using thermodynamic formulas.

However, in MD simulations all the possible microstates contributing to Q_{EVN} can not be obtained. For a specific time t there is only one phase point in the phase space and this point moves with time giving a trajectory in the phase space.

In order to calculate the thermodynamic properties of the system, MD uses kinetic theory rather than statistical mechanics. As explained in the previous chapter, for a classical system, Newton's equation of motion conserve energy and so provide a suitable method for generating a succession of stable points sampled from this microcanonical ensemble.

5.2 Isothermal-Isobaric Ensemble

This system is not isolated but has a thermal contact with a larger system i.e. heat reservoir, so that the temperature is kept constant. Additionally, it is under constant pressure and there is volume fluctuation. The ensemble with constant temperature T, pressure P and number of particles N is called a *isothermal-isobaric ensemble* or *TPN ensemble.*

The probability density is proportional to $\exp(-(\mathcal{H} + PV)/k_BT)$. The quantity appearing in the exponent, when averaged, gives the thermodynamic enthalpy $H =< \mathcal{H} > +P < V >$.

The appropriate partition function is

$$Q_{TPN} = \frac{1}{N}\frac{1}{h^{3N}}\frac{1}{V_0}\int_{6N} dp^{3N}dq^{3N}\exp(-(\mathcal{H} + PV)/kBT) \tag{5.3}$$

The corresponding thermodynamic function is the Gibbs free energy

$$G = -k_B T \ln Q_{TPN} \quad . \tag{5.4}$$

The prescription for generating state points in this ensemble must clearly provide for changes in the sample volume as well as energy. Because all values of the energy are allowed and energy fluctuations are nonzero, the corresponding mechanical equations of motions are not satisfactory as a method of sampling states in this ensemble since they conserve energy. Normal time evaluation occurs on a set of independent constant energy surfaces, each of which should be approximately weighted by the factor $\exp(-(\mathcal{H}+PV)/kBT)$. The prescription for generating a succession of states must make provision for transitions between the energy surfaces, so that a single trajectory can probe all the accessible phase space, and give the correct relative weighting [19].

5.2.1 Constant Temperature Molecular Dynamics

A way to treat the dynamics of a system in contact with a thermal reservoir is to include a degree of freedom which represents that reservoir and carry out a simulation of this extended system. Energy is allowed to flow dynamically from the reservoir to the system and back. The reservoir has a certain thermal inertia associated with it, and the whole technique is rather like controlling the volume of a sample by using a piston. Nosé [28] has described the implementation of this method. The extra degree of freedom is denoted s, and it has a conjugate momentum p_s. The real particle velocities are related to the

time derivatives of the piston by

$$\mathbf{v} = s\dot{\mathbf{r}} = \mathbf{p}/ms \quad . \tag{5.5}$$

An extra potential energy is associated with s, that is

$$U_s = (f+1)k_BT \ln s \tag{5.6}$$

where f is the numbers of degrees of freedom ($3N-3$ if the momentum is fixed) and T is the specified temperature. There is also kinetic energy term

$$K_s = \frac{1}{2}Q\dot{s}^2 = p_s^2/2Q \tag{5.7}$$

where Q is the thermal inertia parameter with dimensions $(energy)(time)^2$ which controls the rate of temperature functions.

The Lagrangian of the system will be

$$L_s = K + K_s - U - U_s \tag{5.8}$$

where $K = \sum_i \frac{1}{2}m_i v_i^2$ and U is evaluated as a function of $\mathbf{r}$ in the usual way. The equations of motion can be readily derived:

$$\ddot{\mathbf{r}} = \mathbf{f}/ms^2 - 2\dot{s}\dot{\mathbf{r}}/s \quad , \tag{5.9}$$

$$Q\ddot{s} = \sum_i m_i\dot{r}_i^2 - (f+1)k_BT/s \quad . \tag{5.10}$$

The extended system Hamiltonian $\mathcal{H}_s = K + K_s + U + U_s$ is conserved, and the extended system is microcanonical.

Manipulation of the delta functions and the integration over the variables s and p_s give a canonical distribution of the variables $\mathbf{r}$ and $\mathbf{p}/s$. Nosé shows how this result depends upon the logarithmic dependence of U_s on s. The equations

of motion are solved using standard predictor-corrector methods, and $\mathcal{H}_s$ is constant. Since temperature is fixed rather than energy, the corresponding ensemble is the canonical ensemble or TVN ensemble.

5.2.2 Constant Pressure Molecular Dynamics

Andersen [29] originally proposed a method for constant pressure MD, which involves coupling the system to an external variable V, the volume of the simulation box. This coupling mimics the action of a piston on a real system.

The piston has a mass W (with actual units of $(mass)(length)^{-4}$) and is associated with a kinetic energy

$$K_V = \frac{1}{2} W \dot{V}^2 \quad . \tag{5.11}$$

The potential energy associated with the additional variable is

$$U_V = PV \tag{5.12}$$

where P is the specified pressure.

The potential and kinetic energies associated with the molecules are written with $\mathbf{r}$ and $\mathbf{v}$ given in terms of scaled variables $\mathbf{r} = V^{1/3}\mathbf{s}$ and $\mathbf{v} = V^{1/3}\dot{\mathbf{s}}$ so that

$$U = U(V^{1/3}\mathbf{s}) \quad , \tag{5.13}$$

$$K = \frac{1}{2} m \sum_i v_i^2 = \frac{1}{2} m V^{2/3} \sum_i \dot{s}_i^2 \quad . \tag{5.14}$$

The equations of motion can be readily obtained from the Lagrangian

$$L_V = K + K_V - U - U_V \tag{5.15}$$

and are given by

$$\ddot{\mathbf{s}} = \frac{\mathbf{f}}{mV^{1/3}} - \frac{2}{3}\frac{\dot{V}}{V}\dot{\mathbf{s}} \quad , \tag{5.16}$$

$$\ddot{V} = (\mathcal{P} - P)/W \tag{5.17}$$

where the forces $\mathbf{f}$ and pressure function $\mathcal{P} = \frac{2}{3V}\frac{1}{2}m\dot{\mathbf{r}}^2 - \frac{1}{3V}\mathbf{f}\cdot\mathbf{r}$ are calculated using coordinates and momenta (Eqn. 4.11).

The Hamiltonian of this system

$$\mathcal{H}_V = K + K_V + U + U_V \tag{5.18}$$

is conserved, being equal to the enthalpy of the system plus an additional factor of $\frac{1}{2}k_BT$ associated with the kinetic energy of the volume fluctuation. These equations of motion generate trajectories which sample the *isobaric-isoenthalpic ensemble* or *HPN ensemble* .

In our work we have used the MD algorithm developed by Çağın [32]. This algorithm is based on the extended Hamiltonian formalism emerging from the constant pressure work of Andersen [29], constant stress work of Parinello and Rahman [30] and the constant temperature work of Nosé [28] and Hoover [31]. Whether adiabatic or isothermal all these forms of MD method represent closed physical systems. In this thesis we have made use of isotermal-isobaric and isobaric-isoenthalpic MD methods.

CHAPTER 6

BINARY PHASE DIAGRAMS

Phase diagrams are visual representations of the state of a material as a function of temperature, pressure, and concentrations of the constituent components and are, therefore, frequently used as guide for alloy design, development, processing, and understanding. A phase diagram of a substance is a map of the ranges at which each phase of a substance is the most stable at equilibrium.

There are several kinds of phase diagrams that can be developed using various thermodynamic variables [36]. The state of a two-component material at constant pressure can be presented in the well-known graphical form of binary phase diagrams. Since binary alloys are studied in this thesis with respect to temperature and concentrations under constant pressure, our phase diagrams will contain variations of atomic concentrations X and temperature $T(K)$.

The simplest type of phase diagrams is illustrated in Figure 6.6. The *solidius* line and *liquidus* line saperate the figure into three regions:

1. Below the solidius line, the alloy is in a homogeneous solid solution phase for every composition.

2. Above the liquidus line, the alloy is in a homogeneous liquid solution

phase for every composition.

3. Between these lines, solid and a liquid phases of the alloy coexist in equilibrium with each other.

Unlike pure metal, for which there is a fixed well defined melting point, an alloy of a fixed composition does not melt at a fixed temperature. The melting takes place over a range of temperatures that usually varies over a few degrees. This is also evident in the phase diagram, because the solidius and liquidus lines converge only at the end points at which the alloys reduces to one or the other of the two pure metals.

6.1 Gibbs Free Energy

Gibbs free energy enables the spontaneity of a process to be expressed only in terms of the properties of a system and allows one to predict the maximum work that process may achieve. Gibbs free energy equation relates the free energy change to the entropy (disorder), temperature, and enthalpy:

$$\Delta G = \Delta H - T\Delta S \tag{6.1}$$

where ΔH is the change in enthalpy and ΔS is the change in entropy. At constant pressure, a phase is thermodynamically stable over the range of temperatures at which it has a lower chemical potential than any other phase. A solid phase has the lowest chemical potential as long as the pressure is not too low and is the most stable at low temperatures. Chemical potentials of phases change with temperature in different ways, and when the temperature is raised, the potential of another phase will fall below that of the solid. When

this happens, a phase transition occurs if it is kinetically feasible to do so.

Above the melting point, the Gibbs free energy of the liquid phase is lower than that of the solid phase. The Gibbs free energies of two phases can be compared by

$$\Delta G_{melt} = G_L - G_S = H_L - H_S - T(S_L - S_S) = \Delta H_{melt} - T\Delta S_{melt} \quad (6.2)$$

The enthalpy difference $\Delta H = \Delta E + P\Delta V$ is positive because in the liquid phase many of the atoms occupy interstitial positions, which results in a high energy. The volume is also larger in the liquid than in the solid phase so that atoms are pulled away from each other with some expenditure of energy. But ΔS is also positive because the liquid phase, being more disordered than solid, has a higher entropy. For $T < T_{melt}$ the term ΔH dominates, that is $\Delta G > 0$ and no melting takes place, while for $T > T_{melt}$, the entropy term $T\Delta S$ dominates and the solid melts completely. At $T = T_{melt}$ the energy and entropy terms exactly balance each other, so that $\Delta G_{melt} = 0$, and two phases are in equilibrium with each other.

The stability of an alloy as the concentration $X_i = N_i/N$ is varied over a wide range is determined with minimum Gibbs free energy. Suppose that for a solid mixture the Gibbs free energy of the alloy has a lowest U-shaped curve as in Figure 6.1. In this phase, the alloy is homogeneous and is a primary solid solution throughout the concentration range. The homogeneous solid solution phase is more stable than any other structure.

When the Gibbs free energy curve has the lowest W-shaped as in Figure 6.2, there are three possibilities: If $X < X'$ the lowest free energy is given

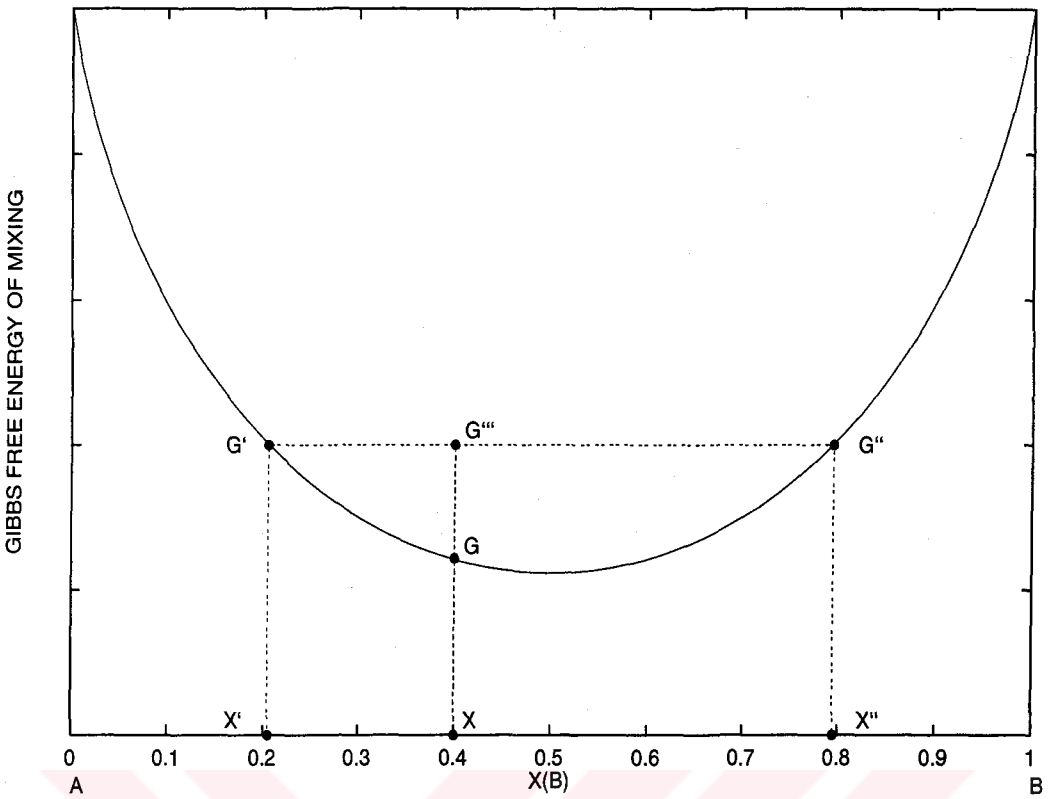

Figure 6.1: Gibbs free energy of mixing of binary components which form a complete range of solutions.

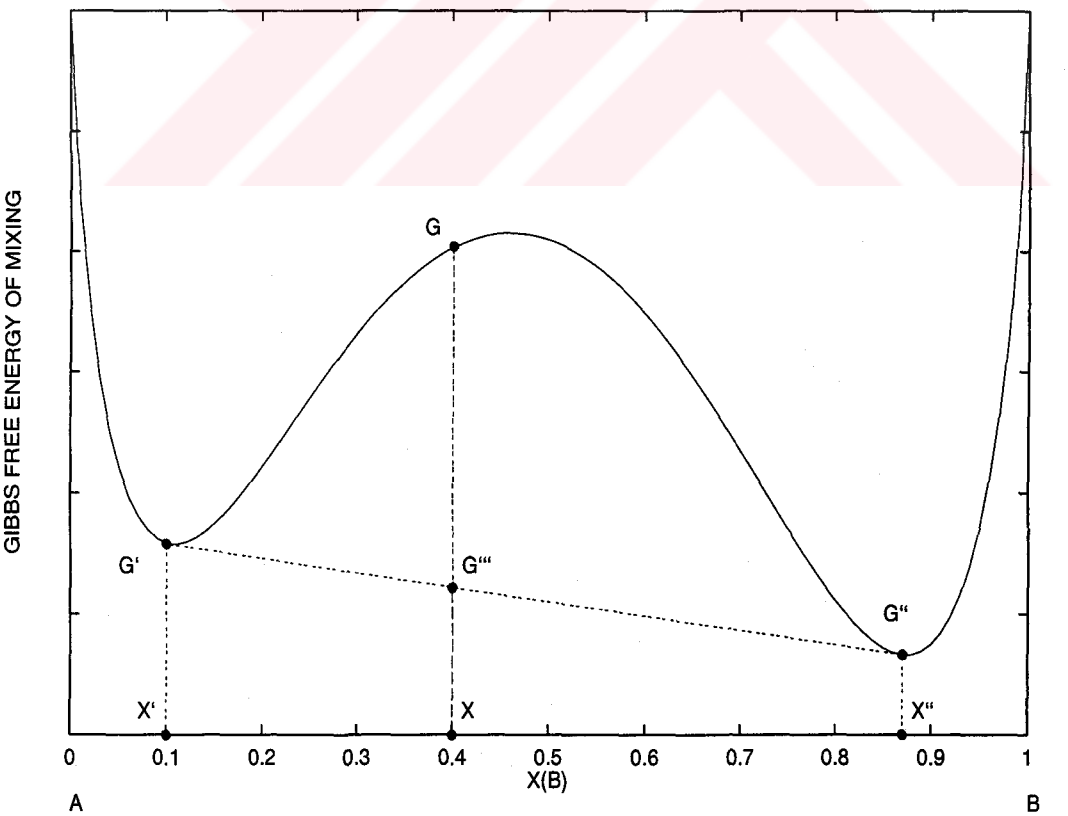

Figure 6.2: Gibbs free energy of mixing of binary components in a system which exhibits an immiscibility gap.

by the curve G_AG', that is, the system is a primary solid solution rich in A. Similarly, if $X > X''$ the Gibbs free energy is given by $G''G_B$ and the system is a solid solution rich in B. However, in the range $X' < X < X''$, the lowest free energy curve is not given by the solid curve $G'GG''$, but rather by the straight line $G'G'''G''$. Physically this means that in this concentration range the system breaks into a phase mixture whose components have concentrations X' and X''. The alloy contains the grains of these different phases which have enormous effect on the properties of the alloy.

6.2 Entropy of Mixing

When two type of metals are mixed at the same temperature to form an alloy, the entropy of the system increases because the system becomes more disordered. This increase is the *entropy of mixing.* Using the statistical definition $S = k_b \ln \Omega$, entropy of mixing, ΔS_{mix}, can be calculated.

Suppose that one mole of A-B alloy has N atoms of which N_A are A type and the remaining $N_B = N - N_A$ are B type. To calculate Ω we need to count the number of different microstates, i.e., the number of atomic arrangements consistent with the macrostate. The number of distinct arrangements of microstates, for N atoms is

$$\Omega = \frac{N!}{N_A!N_B!} \quad . \tag{6.3}$$

Using the Stirling formula, an approximation valid for the large number of atoms, $\ln N! \simeq N \ln N - N$, the entropy of mixing for one mole of atom

$$\Delta S_{mix} = -R[X_A \ln X_A + X_B \ln X_B] \tag{6.4}$$

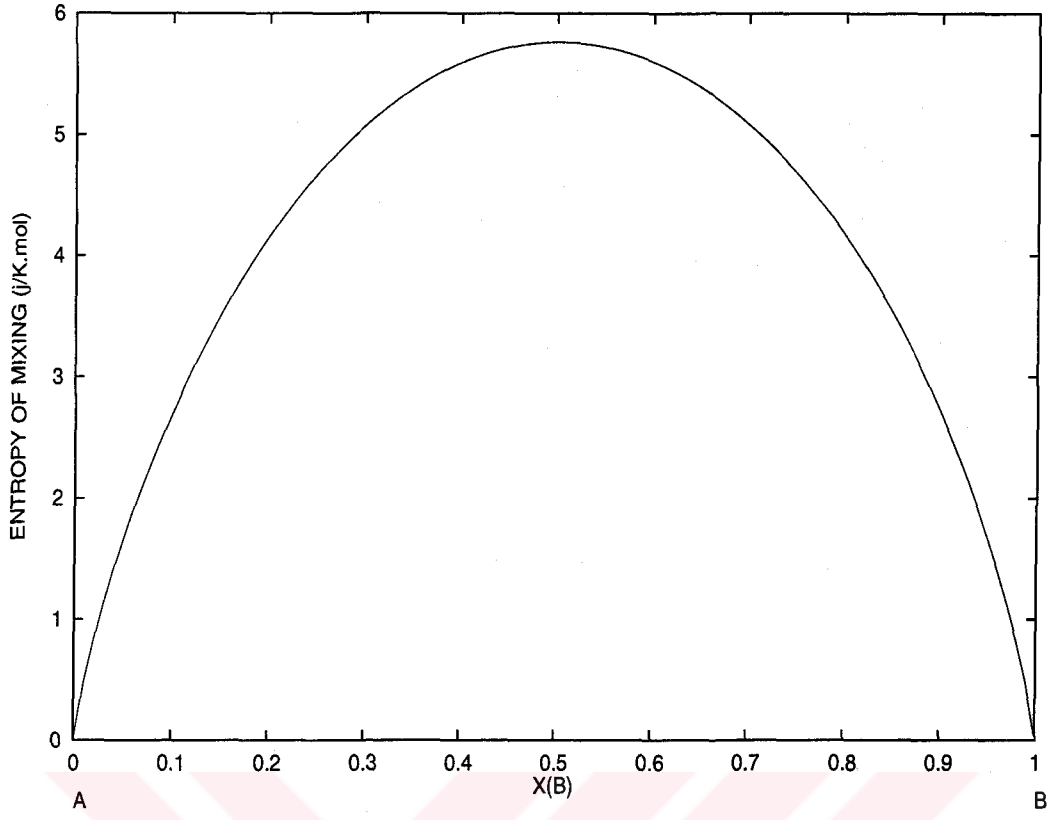

Figure 6.3: Entropy of mixing for a random mixing of binary components .

where $X_A = N_A/N$ is the concentration of A atoms and $X_B = 1 - X_A$ is the concentration of B atom, and $R = k_B N$ is the gas constant. Since the logarithmic terms are negative, $X_A, X_B < 1$, ΔS_{mix} is positive.

The variation of entropy with concentration is indicated in Figure 6.3, where ΔS_{mix} has a maximum at $X = 0.5$, the point of maximum disorder, and decreases on either side of this point. It reaches zero at the end point at which a state of complete order prevails. Near the end points ΔS_{mix} increases very rapidly as the other element is added. This means that there is a strong tendency toward solution at low concentrations, regardless of other possibilities unfavorable factors.

6.3 Development of Phase Diagram

The concept of Gibbs free energy leads readily to the phase diagram. The relation between the phase diagram and Gibbs free energies can be seen in Figures 6.7, 6.4 and 6.5. This shows a typical binary diagram involving complete solubilities of components in both solid and liquid phases, and the corresponding Gibbs free energy versus concentration diagrams at temperatures for solid, liquid and intermediate phase are presented.

At temperature T'', the Gibbs free energy curve of solid lies entirely below that of liquid curve and therefore the alloy is in the solid phase (Figure 6.4). At temperature T', the alloy is completely melted because the liquid curve lies entirely below that of the solid (Figure 6.5). However, at some temperature T, the liquid's Gibbs free energy curve crosses solid curve in Figure 6.7. In this situation, the structure of the system depends on the average concentration X. Once X is known the structure of the alloy can be inferred by using the rules explained previously for minimizing Gibbs free energy. This is the lowest common tangent line, which touches the curve at concentration values X' and X'', is chosen as minimum Gibbs free energy rather than solid or liquid Gibbs free energies. The amount of liquid phase and solid phase can be found by the appropriate lever formula.

If the Gibbs free energy curves for the solid and liquid phases are given at all temperatures at which they cross each other, then the solidius and liquidus lines of the phase diagram of the alloy can be obtained. And the reason why the melting processes of an alloy extends over a range of temperatures is that

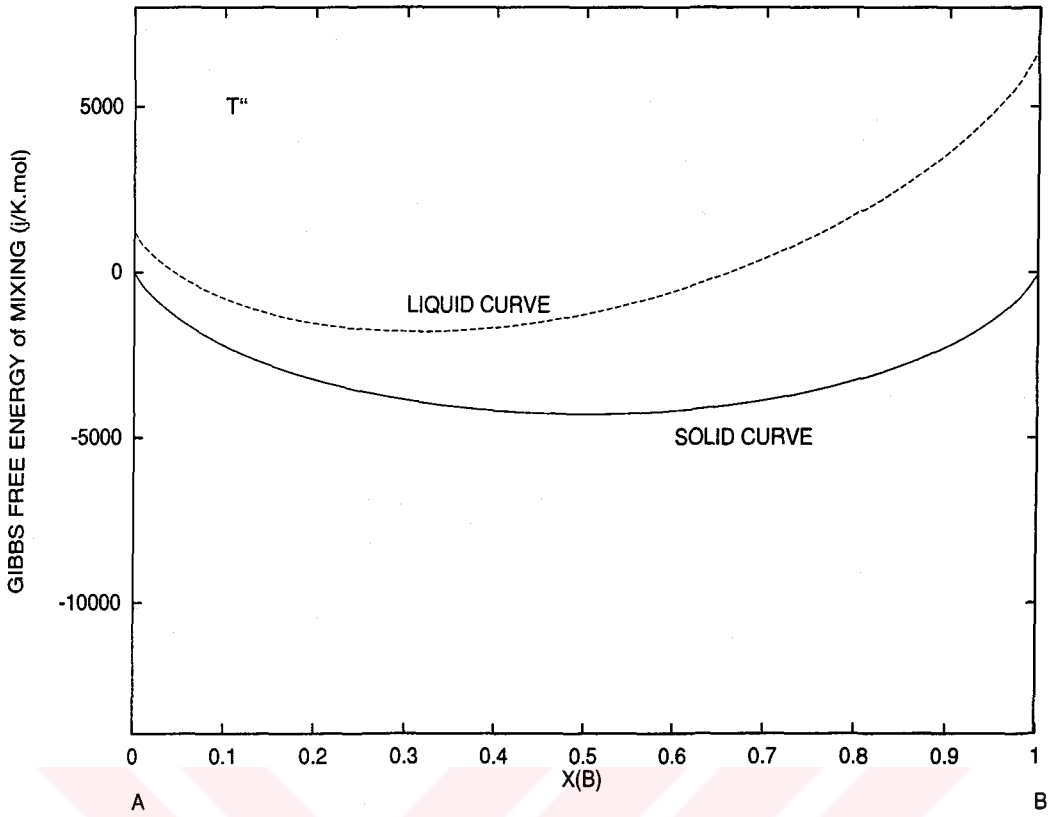

Figure 6.4: Gibbs free energy of mixing of solid and liquid phases at temperature T".

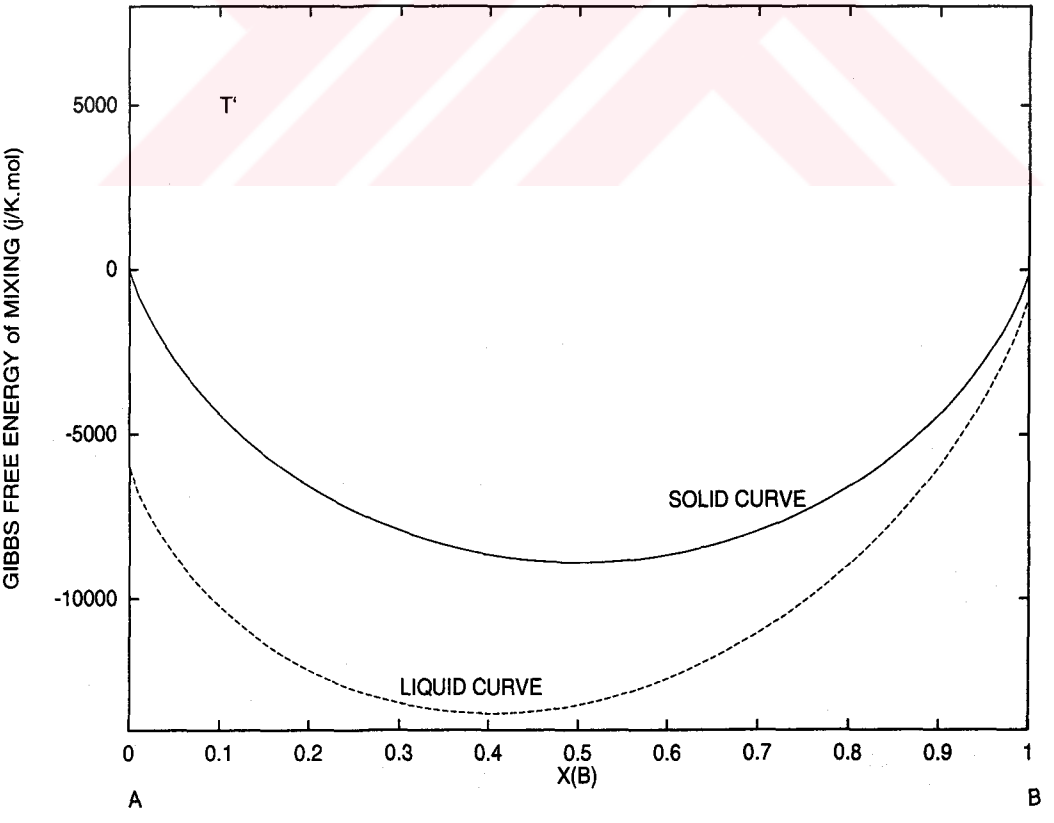

Figure 6.5: Gibbs free energy of mixing of solid and liquid phases at temperature T'.

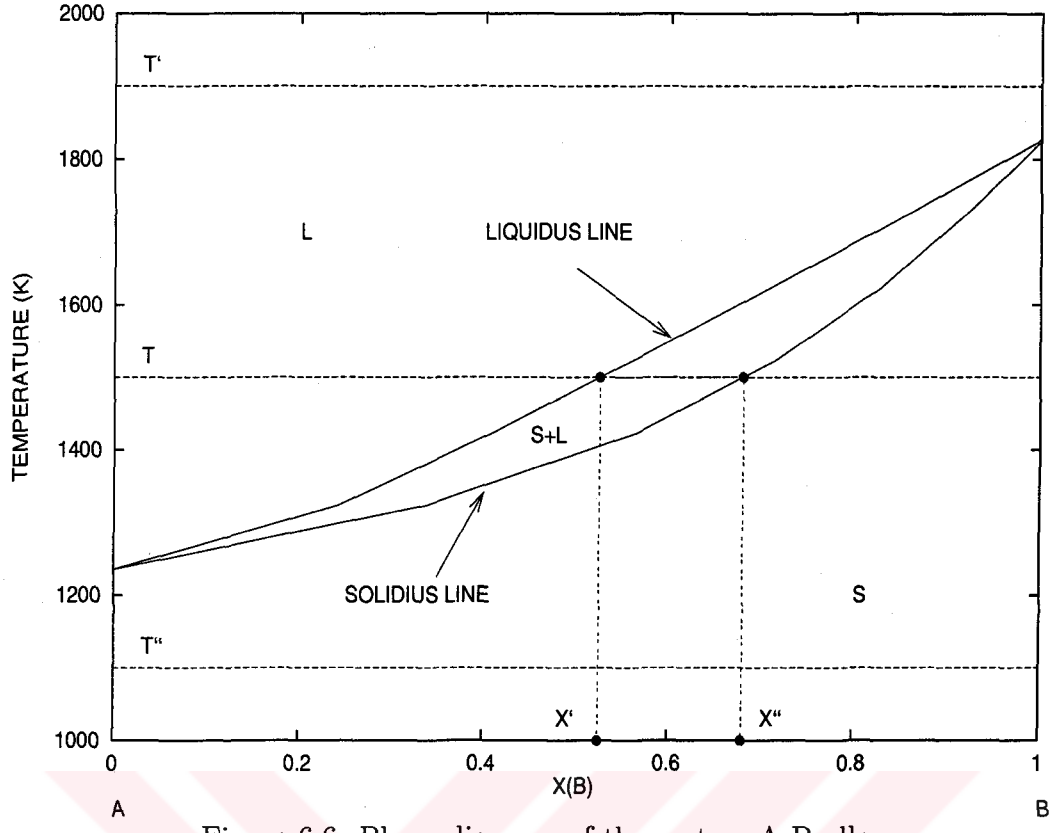

Figure 6.6: Phase diagram of the system A-B alloy.

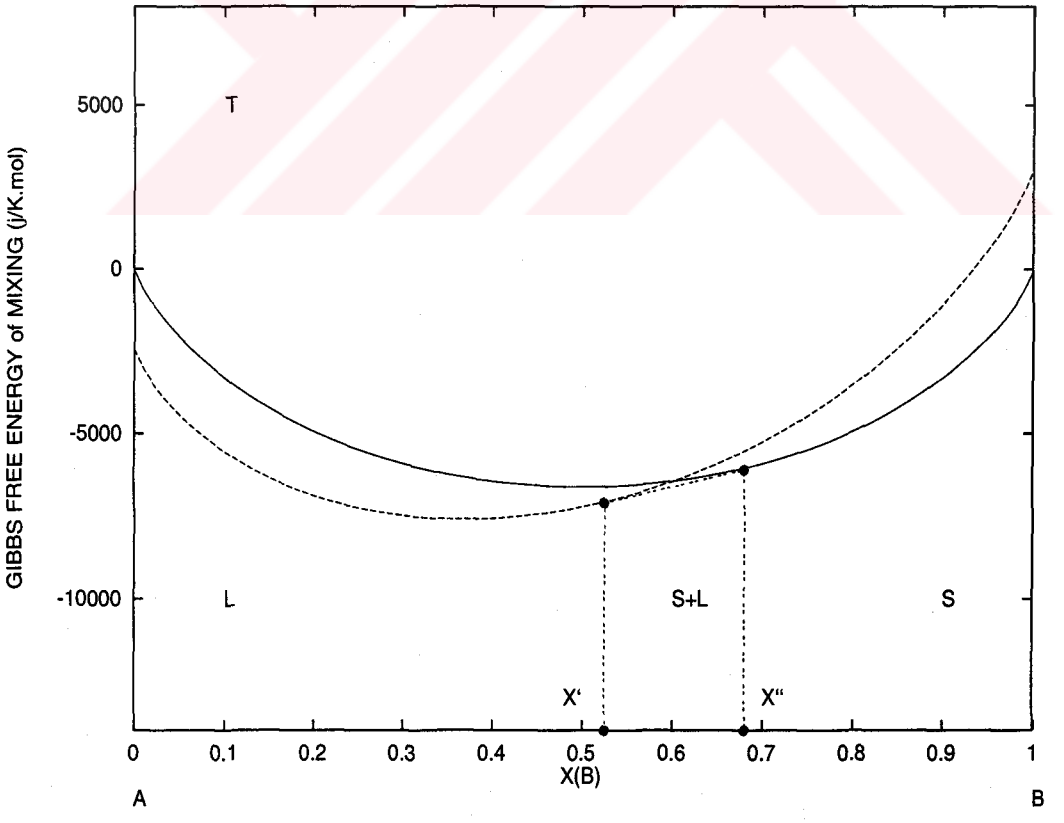

Figure 6.7: Gibbs free energy of mixing of solid and liquid phases at temperature T .

the crossing and uncrossing of the solid and liquid Gibbs free energy curves are accomplished over a finite range of temperatures.

In order to find the Gibbs free energy curves for both liquid and solid phases, the enthalpy of mixing and entropy of mixing for these phases should be determined. The entropy of mixing value for random mixing is temperature independent and obtained previously as

$$\Delta S_{mix} = -R[X \ln X + (1 - X) \ln(1 - X)] \tag{6.5}$$

where X is the concentration. ΔH_{mix} values for liquid and solid mixtures are calculated at any temperature from the simulation results of the enthalpies as

$$\Delta H_{mix} = H_{AB} - X_A H_A - X_B H_B \tag{6.6}$$

where H_{AB}, H_A and H_B are enthalpy values of the alloy, pure metal A and pure metal B, respectively.

The enthalpy of mixing for solid phase ΔH^S_{mix} is calculated by averaging the values of ΔH_{mix} at temperatures of solid phase and an analytic form depending on concentration X is obtained. Similarly for liquid phase, we can get ΔH^L_{mix}. As a result, both Gibbs free energy curves for solid and liquid mixtures are found.

$$\Delta G^S_{mix} = \Delta H^S_{mix} - T\Delta S_{mix} \tag{6.7}$$

$$\Delta G^L_{mix} = \Delta H^L_{mix} - T\Delta S_{mix} \tag{6.8}$$

The relative positions of solid and liquid curves in the Figures 6.7, 6.4 and 6.5 are drawn by using Gibbs free energy of melting $\Delta G_{melt}(T)$ of pure metals

A and B. Once we know Gibbs free energy change in melting and mixing of both pure metals A and B, both curves can be drawn. The differences in the end points is the value of $\Delta G_{melt}(T)$ at that temperature so the liquid curve has the form

$$\Delta G'^{L}_{mix} = \Delta G^{L}_{mix} + X_A \Delta G^{A}_{melt} + X_B \Delta G^{B}_{melt} \tag{6.9}$$

Therefore, this value is the total Gibbs free energy change when the system comes from solid metals to the liquid alloy at temperature T.

CHAPTER 7

RESULTS AND DISCUSSION

7.1 Procedure

In this work, we have done a computer simulation study on solid and liquid solutions of Ag-Pd, Ag-Pb and Ag-Cu systems using a MD algorithm based on extended Hamiltonian formalism. The properties of the metals silver (Ag), paladium (Pd), lead (Pb) and copper (Cu), are also obtained since they are the end values in graphs drawn with respect to concentration. The effective potential is chosen as the Sutton-Chen type many-body empirical potential which is described in Chapter 3. This potential is very simple in its form and contains only 4 parameters to fit the properties of the crystal. During our simulation we have made use of the original Sutton-Chen parameters. Although the parameters were fitted to the properties of the crystal at low temperature, still it gave reasonable results for the liquid state.

The simulations started with 500 atoms randomly distributed on fcc lattice. We have thermalized the system in HPN ensemble. The system is heated from 1 K to the target temperature using HPN ensemble by slowly heating while scaling the velocities to increment the temperature by 1 K/step over the specific number of steps depending on the target temperature. This is followed by strict velocity scaling at each temperature, keeping the system at this temperature

in HPN ensemble 2000 steps (4ps of simulation) . Then using the TPN ensemble at this temperature for 20000 steps (40ps of simulation), volume, density, enthalpy, potential energy values and radial distribution functions are calculated. A fifth order Gear predictor-corrector algorithm is used with time step, $\Delta t = 2\ fs$. While using the Parinello-Rahman constant pressure ensemble the piston mass parameter is kept as $W = 400$ in TPN runs and the Nosé-Hoover parameter is set to $Q = 100$.

7.2 Results

Simulation results are grouped in two sections. In section 7.2.1 structure and thermodynamical properties of Ag-Pd, Ag-Pb and Ag-Cu alloys are presented for solid and liquid forms and for various concentrations. In this section radial distribution functions and density, enthalpy, potential energy and volume values are presented, lattice distances are calculated. From the enthalpy results we have calculated the enthalpy of mixing values for these concentrations. Results are compared with experimental values whenever it is possible.

In section 7.2.2 Gibbs free energy of mixing are obtained for solid and liquid phases of these alloys. Phase diagrams are drawn and compared with the phase diagrams obtained from the experimental data [37].

7.2.1 Structure and Thermodynamical Properties

In Figure 7.1 radial distribution functions of Ag, Pd, Pb and Cu are given in the solid and liquid temperature range. For these metals at room temperature fcc structure is maintained. But as the temperature is increased, a continuing

broadening of the peaks and loss of long range order is observed. Ag melts at 1235K. The radial distribution function drawn at 1300K indicates that Ag is about to melt when we compare it with a typical liquid form of 2000K radial distribution function. Ag is completely in liquid form at 2000K since we observe only one peak corresponding to the nearest neighbor atoms. Long range is completely destroyed. Melting point of Pd is 1827K. From Figure 7.1 at 1700K we observe the solid liquid transition is still taking place whereas at 2000K Pd is completely in liquid form. Pb is completely melted at 1500K. Melting point of Cu is 1358K. At 1100K it has not yet melted and at 1500K it is completely in liquid form.

The radial distribution functions of the alloys are given in Figures 7.2, 7.3 and 7.4. Only one concentration of, 40% of Ag and 60% of Pd, Pb or Cu, is chosen as an example to see the structure of the alloys. The behaviour is the same at the other concentrations. The change of the radial distribution functions of the alloys with temperature are given at the top figures. And, the radial distribution for the same type and different type of atoms can be seen in the following graphs.

In Figure 7.2 radial distribution functions of Pd6Ag4 alloy at temperatures 300K, 1500K and 2000K for total pair interactions and for pairs Ag-Pd, Pd-Pd and Ag-Ag interactions are given. The effect of heating on structural changes can easily be followed in these graphs. The relative distances between Ag and Pd atoms, between Pd atoms and between Ag atoms are approximately equal, and the shape of the total radial distribution function of Pd6Ag4 is not changed. In Figure 7.3 radial distribution functions of Pb6Ag4 at temperatures

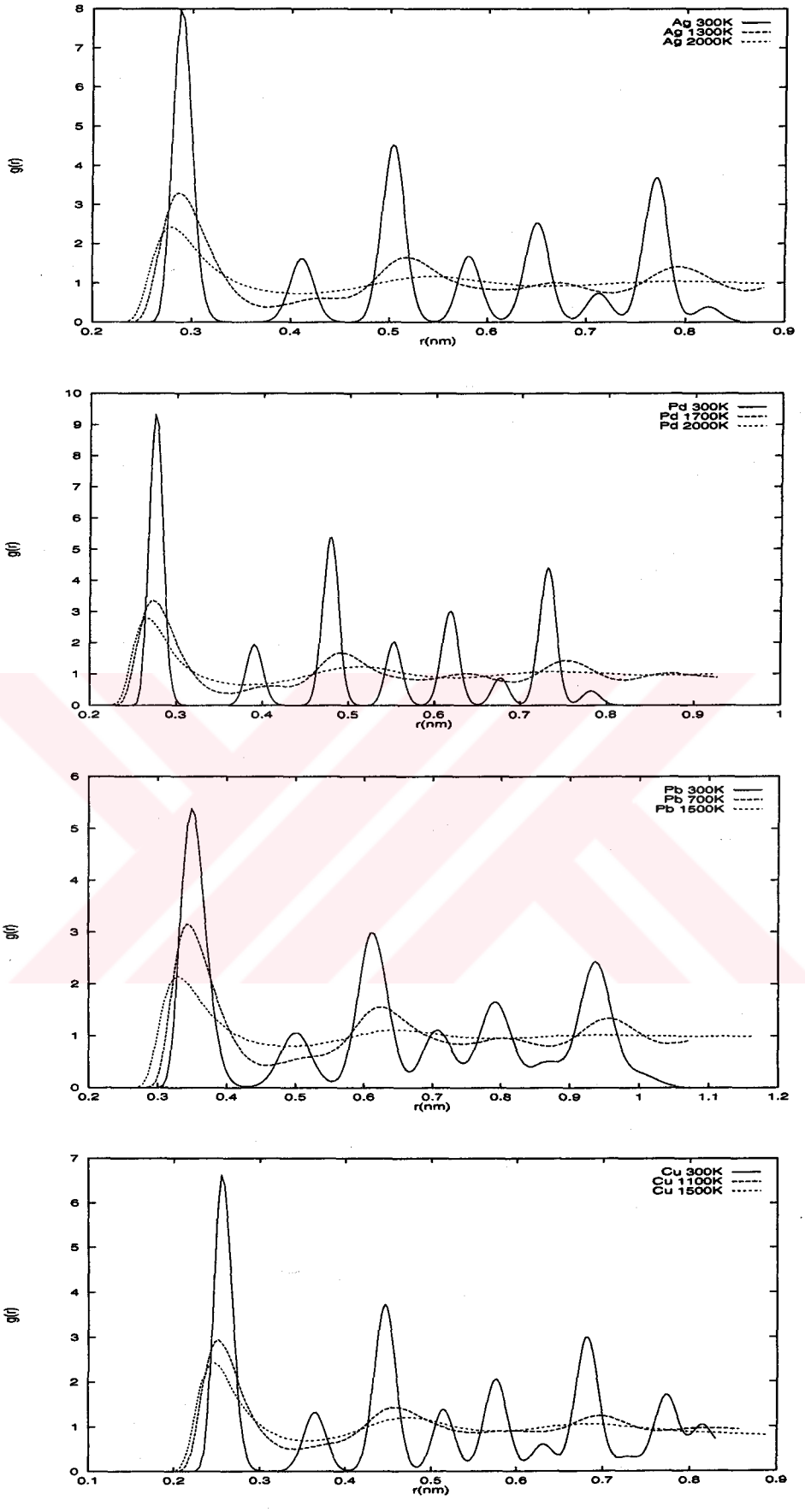

Figure 7.1: Radial distribution functions for Ag, Pd, Pb and Cu.

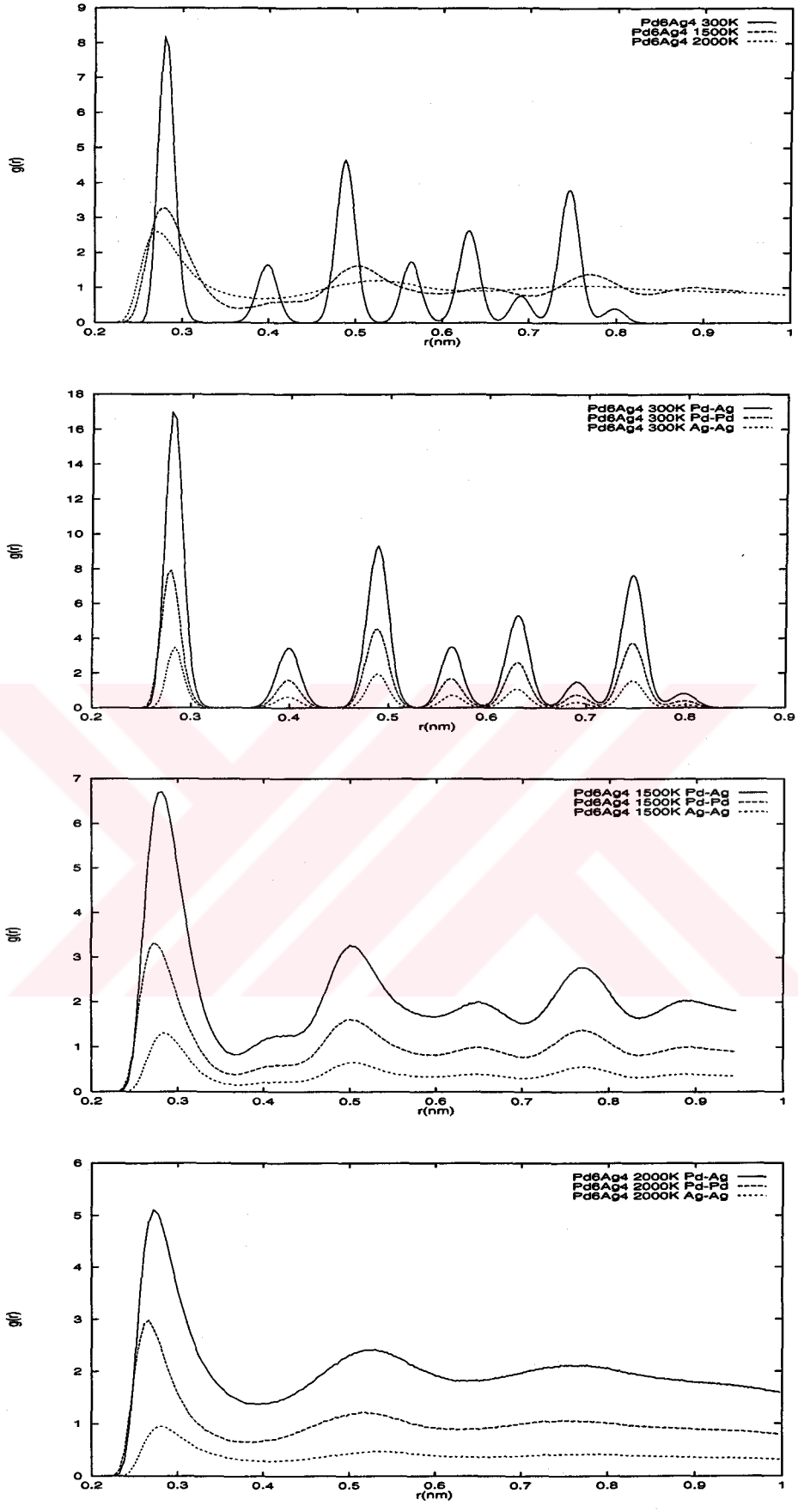

Figure 7.2: Radial distribution functions of Pd6Ag4 alloy at temperatures 300K, 1500K and 2000K for total pair interactions and for pairs Ag-Pd, Ag-Ag and Pd-Pd interactions .

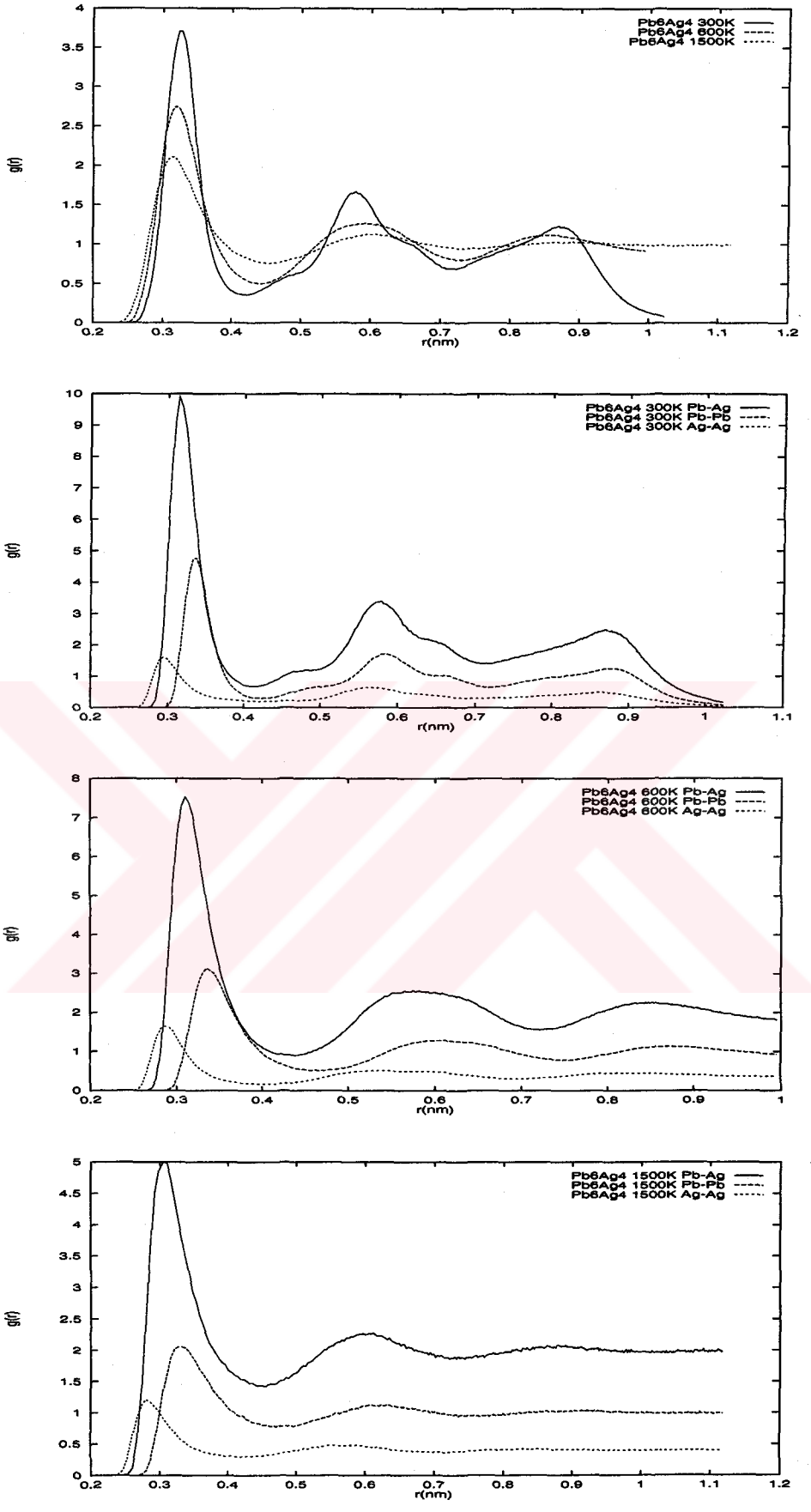

Figure 7.3: Radial distribution functions of Pb6Ag4 alloy at temperatures 300K, 600K and 1500K for total pair interactions and for pairs Ag-Pb, Ag-Ag and Pb-Pb interactions .

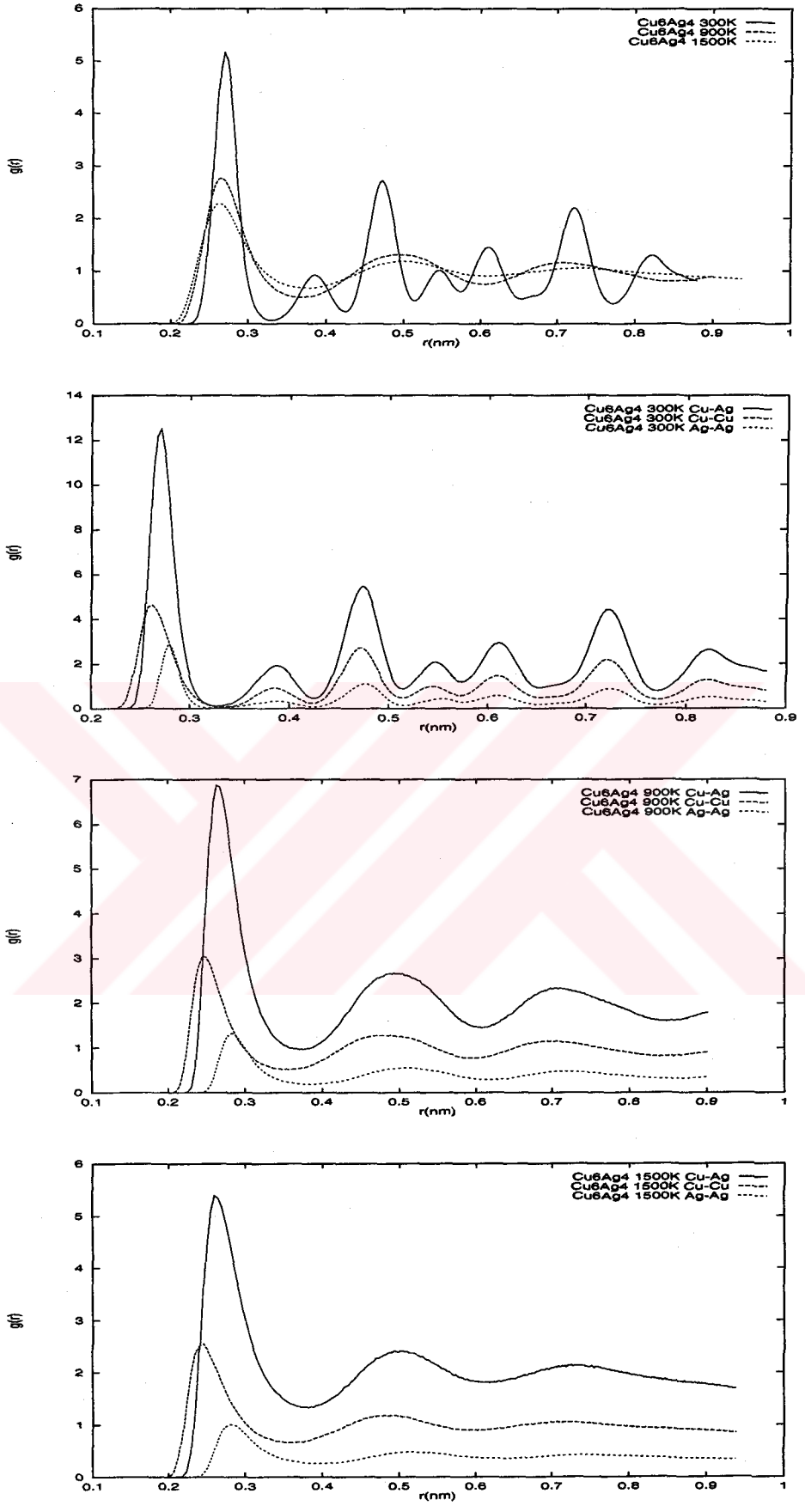

Figure 7.4: Radial distribution functions of Cu6Ag4 alloy at temperatures 300K, 900K and 1500K for total pair interactions and for pairs Ag-Cu, Ag-Ag and Cu-Cu interactions .

at 300K, 600K and 1500K are given. Looking at the first peaks, we see that Ag atoms are closer to each other. Pd atoms have longer distances between them. The shape of the total radial distribution function in 300K is changed so that the fcc structure of the alloy is not kept. There we may expect that Ag and Pb do not show tendency to mix in solid form. In Figure 7.4 we can see radial distribution functions of the Cu6Ag4 alloy at 300K, 900K and 1500K for total pair interactions and for pair Ag-Cu, Cu-Cu and Ag-Ag interactions. The relative distances between Ag and Cu atoms, between Cu atoms and Ag atoms are different but the shape of the total fcc structure of the Cu6Ag4 alloy is not changed much.

The results of TPN MD simulation of the Ag-Pd,Ag-Pb and Ag-Cu alloys can be seen in Tables 7.1 to 7.12. These give density, enthalpy, potential energy and volume values of these alloys. We have examined the effects of temperature and change of concentration on these properties.

In Figure 7.5 we have plotted density values of the Ag-Pd alloy with respect to % of Pd for the temperature range from 300K to 2000K. In solid form of Ag-Pd from 300K to 1300K, density increases linearly as the paladium concentration is increased. Also in the liquid form, from 1800K to 2000K we observe the density increase with Pd concentration. On the other hand from 1400K to 1700K we can see the effect of Pd concentration on solid liquid transformation. Since Pd has a high melting point, as the Pd concentration increases, change from solid phase to liquid phase is observed as expected. In Figure 7.6 variation of density values of Ag-Pd alloy with respect to temperature is given. The solid liquid transition for Ag is observed between 1300K and 1400K and

for Pd between 1700K and 1800K so the melting points of these metals should be in this range. For alloys depending on the concentration of the pure metals, solid to liquid transition may occur at a temperature range of more than 100K since the alloy has no definite melting point and it has a solid liquid mixture intermediate phase.

Since enthalpy is only a potential function, the actual values of the enthalpies are not important but only the enthalpy changes have a physical importance. In fact, these values include total kinetic and potential energies and because potential energy is dominant in condensed phases they have negative values. The value of PV is ignored and we assumed that $\Delta H \simeq \Delta E$.

In Figure 7.7 the enthalpy change of the Ag-Pd with the concentration of Pd is decreasing linearly in solid and liquid form. We can see the enthalpy differences in liquid and solid phase. The enthalpy of Ag-Pd alloy in Figure 7.8 is increasing with temperature as expected. The slope gives the specific heat of the alloy. When solid-liquid transition occurs, the enthalpy increase gives the value of enthalpy of melting. At the other end, simulation results potential energy and volume per mole are plotted with respect to concentration and temperature. We can see the effects of solid liquid phase transition on the properties. Since the atomic radius of Pd is less than that of Ag, volume of the Ag-Pd alloy decreases with increasing Pd concentration.

Figure 7.13 gives the density variation of Ag-Pb alloy with respect to the change of concentration of Pb. Pb atom is heavier than Ag atom, so density increases with the increasing Pb concentration. However, volume increase in Figure 7.19 sometimes dominates and we can see decrease in density of Ag-Pb

alloy, That is, density does not show a linear change. In Figure 7.14 gives the density change of Ag, Pb and its alloys with respect to temperature. In Figure 7.20 solid Pb expends more rapidly than Ag, therefore density of Pd decreases more than density of Ag.

Enthalpy and potential energy changes with respect to concentration and temperature are given in Figures 7.15, 7.16, 7.17 and 7.18. They show linear change but again we can see the effect of solid liquid transition. Enthalpy changes of the alloys with respect to temperature in Figure 7.16 do not occur at a single step. Rather the change occurs on a long temperature range because of the solid-liquid intermediate phase of the Ag-Pb alloy.

In Figure 7.21 density values of the Ag-Cu alloy with respect to % of Cu for the temperature range 300K to 1500K are plotted. It is at solid state from 300K to 700K and at liquid state from 1400K to 1500K. Between the temperatures 700K and 1400K, density of the alloy drops when solid liquid transition occurs. Density change with respect to temperature is given in Figure 7.22. Density values may decreases slowly when intermediate phase occurs.

In our simulations Cu melts exactly at 1100K so the density value is the value of solid liquid mixture of Cu. In fact density of Cu should drop at 1100K but there should be enough data points around this temperature. The same properties can be seen in the enthalpy and potential energy graphs in Figures 7.23, 7.24, 7.25 and 7.26. Since Cu has smaller atomic radius than Ag, the volumes of Ag-Cu alloy are decreasing with increasing Cu concentrations in Figure 7.27. Figure 7.28 gives the decrease of the volume with temperature.

Table 7.1: The density values in g/cm^3 for the Ag-Pd binary alloy at temperatures ranging from 300K to 2000K as obtained from TPN MD simulation after 20000 steps.

T(K)	Ag	Pd2Ag8	Pd4Ag6	Pd6Ag4	Pd8Ag2	Pd
300	10.2707	10.5709	10.8751	11.1832	11.4953	11.813
400	10.1873	10.4888	10.7972	11.1085	11.4244	11.7458
500	10.1020	10.4077	10.7185	11.0328	11.3520	11.6769
600	10.0136	10.3213	10.6361	10.9548	11.2775	11.6064
700	9.9214	10.2320	10.5514	10.8740	11.2014	11.5343
800	9.8255	10.1400	10.4622	10.7899	11.1211	11.4596
900	9.7233	10.0454	10.3699	10.7020	11.0387	11.3827
1000	9.6162	9.9388	10.2718	10.6099	10.9538	11.3029
1100	9.4987	9.8225	10.1679	10.5140	10.8631	11.2192
1200	9.3696	9.7100	10.0574	10.4127	10.7699	11.1320
1300	9.2230	9.5769	9.9342	10.3001	10.6677	11.0405
1400	8.3546	9.3491	9.7910	10.1738	10.5598	10.9403
1500	8.2159	8.5399	8.8798	10.0243	10.4384	10.8379
1600	8.0843	8.4082	8.7404	9.1850	10.2954	10.7225
1700	7.9328	8.2765	8.6155	8.9612	9.3217	10.5903
1800	7.7974	8.1355	8.4804	8.8372	9.1999	9.6332
1900	7.6662	8.0070	8.3524	8.6899	9.0911	9.4411
2000	7.5040	7.8538	8.1952	8.5498	8.9269	9.3090

Table 7.2: The enthalpy values in kj/mol for the Ag-Pd binary alloy at temperatures ranging from 300K to 2000K as obtained from TPN MD simulation after 20000 steps.

T(K)	Ag	Pd2Ag8	Pd4Ag6	Pd6Ag4	Pd8Ag2	Pd
300	-277.9558	-295.9030	-313.8334	-332.7346	-352.3116	-372.5576
400	-275.2383	-292.8840	-311.1512	-330.0588	-349.6632	-369.9200
500	-272.5634	-290.2294	-308.5072	-327.4161	-347.0273	-367.2970
600	-269.8308	-287.5114	-305.7819	-324.7242	-344.3491	-364.6250
700	-267.0307	-284.7268	-303.0323	-322.0018	-341.6375	-361.9359
800	-264.1720	-281.8673	-300.2102	-319.1974	-338.8547	-359.1784
900	-261.1898	-278.9860	-297.3147	-316.3256	-336.0220	-356.3888
1000	-258.1359	-275.8900	-294.3188	-313.3905	-333.1399	-353.5372
1100	-254.8961	-272.6420	-291.2241	-310.3704	-330.1580	-350.6123
1200	-251.4571	-269.4470	-288.0210	-307.2560	-327.1214	-347.6210
1300	-247.7127	-265.8927	-284.5828	-303.9490	-323.9248	-344.5374
1400	-232.1080	-260.7908	-280.8034	-300.4024	-320.6304	-341.2945
1500	-228.7469	-246.4785	-264.6674	-296.4464	-317.0772	-338.0022
1600	-225.4916	-243.1371	-261.1865	-281.2392	-313.1438	-334.4573
1700	-221.8417	-239.8341	-257.9234	-276.2069	-295.0039	-330.5976
1800	-218.5191	-236.2771	-254.3803	-272.9733	-291.6982	-311.8762
1900	-215.2197	-232.9684	-251.0603	-269.3222	-288.0714	-307.1155
2000	-210.9356	-228.8104	-246.7239	-265.1761	-284.2378	-303.3975

Table 7.3: The potential energy values in kj/mol for the Ag-Pd binary alloy at temperatures ranging from 300K to 2000K as obtained from TPN MD simulation after 20000 steps.

T(K)	Ag	Pd2Ag8	Pd4Ag6	Pd6Ag4	Pd8Ag2	Pd
300	-281.6949	-299.3454	-317.5764	-336.4759	-356.0625	-376.3003
400	-280.2294	-297.8724	-316.1392	-335.0489	-354.6539	-374.9108
500	-278.8016	-296.4651	-314.7384	-333.6528	-353.2651	-373.5317
600	-277.3153	-294.9943	-313.2688	-332.2101	-351.8332	-372.1104
700	-275.7614	-293.4568	-311.7636	-330.7298	-350.3668	-370.6609
800	-274.1456	-291.8440	-310.1853	-329.1735	-348.8327	-369.1590
900	-272.4145	-290.2097	-308.5366	-327.5508	-347.2464	-367.6127
1000	-270.6081	-288.3612	-306.7906	-325.8596	-345.6133	-366.0090
1100	-268.6152	-286.3610	-304.9433	-324.0883	-343.8770	-364.3329
1200	-266.4230	-284.4112	-302.9878	-322.2228	-342.0885	-362.5876
1300	-263.9270	-282.1052	-300.7974	-320.1599	-340.1386	-360.7502
1400	-249.5681	-278.2493	-298.2742	-317.8596	-338.0887	-358.7528
1500	-247.4536	-265.1840	-283.3746	-315.1517	-335.7847	-356.7092
1600	-245.4471	-263.0909	-281.1398	-301.1940	-333.0988	-354.4123
1700	-243.0445	-261.0359	-279.1266	-297.5000	-316.2054	-351.7983
1800	-240.9702	-258.7262	-276.8283	-295.4241	-314.1467	-334.3259
1900	-238.9142	-256.6633	-274.7582	-293.0160	-311.7683	-330.8118
2000	-235.8784	-253.7531	-271.6704	-290.1772	-309.1812	-328.3379

Table 7.4: The volume values in nm^3 for the Ag-Pd binary alloy at temperatures ranging from 300K to 2000K as obtained from TPN MD simulation after 20000 steps.

T(K)	Ag	Pd2Ag8	Pd4Ag6	Pd6Ag4	Pd8Ag2	Pd
300	8.7194	8.4490	8.1906	7.9434	7.7069	7.4792
400	8.7907	8.5152	8.2497	7.9968	7.7547	7.5220
500	8.8650	8.5815	8.3102	8.0517	7.8041	7.5664
600	8.9433	8.6535	8.3746	8.1090	7.8557	7.6123
700	9.0263	8.7289	8.4418	8.1693	7.9090	7.6599
800	9.1144	8.8080	8.5138	8.2330	7.9661	7.7098
900	9.2103	8.8910	8.5896	8.3005	8.0256	7.7619
1000	9.3128	8.9863	8.6716	8.3726	8.0878	7.8167
1100	9.4280	9.0927	8.7602	8.4490	8.1554	7.8751
1200	9.5579	9.1981	8.8564	8.5312	8.2259	7.9367
1300	9.7098	9.3259	8.9664	8.6205	8.3047	8.0025
1400	10.7192	9.5531	9.0974	8.7315	8.3896	8.0758
1500	10.9001	10.4584	10.0310	8.8617	8.4872	8.1521
1600	11.0776	10.6222	10.1910	9.6714	8.6050	8.2398
1700	11.2891	10.7912	10.3387	9.9131	9.5038	8.3427
1800	11.4851	10.9783	10.5034	10.0521	9.6297	9.1716
1900	11.6817	11.1544	10.6644	10.2225	9.7718	9.3582
2000	11.9342	11.3720	10.8689	10.3900	9.9242	9.4910

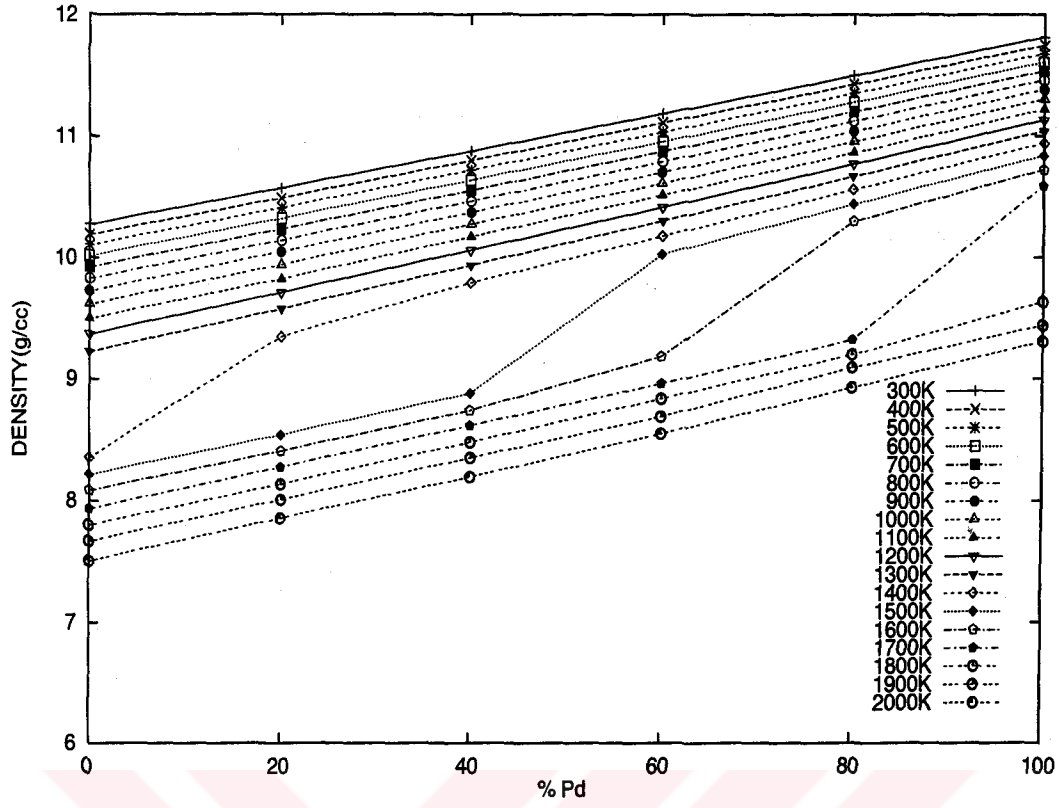

Figure 7.5: Density of Ag, Pd and their alloys with respect to percentage concentration of Pd in Ag .

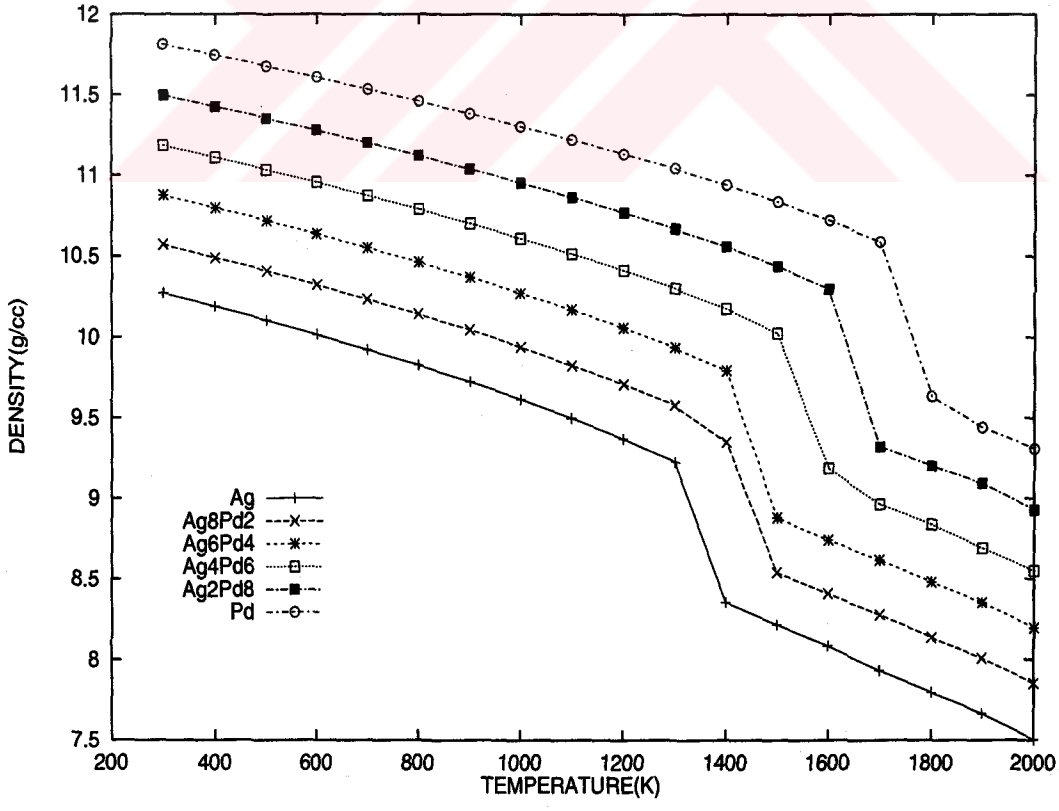

Figure 7.6: Density of Ag, Pd and their alloys with respect to temperatures ranging from 300K to 2000K.

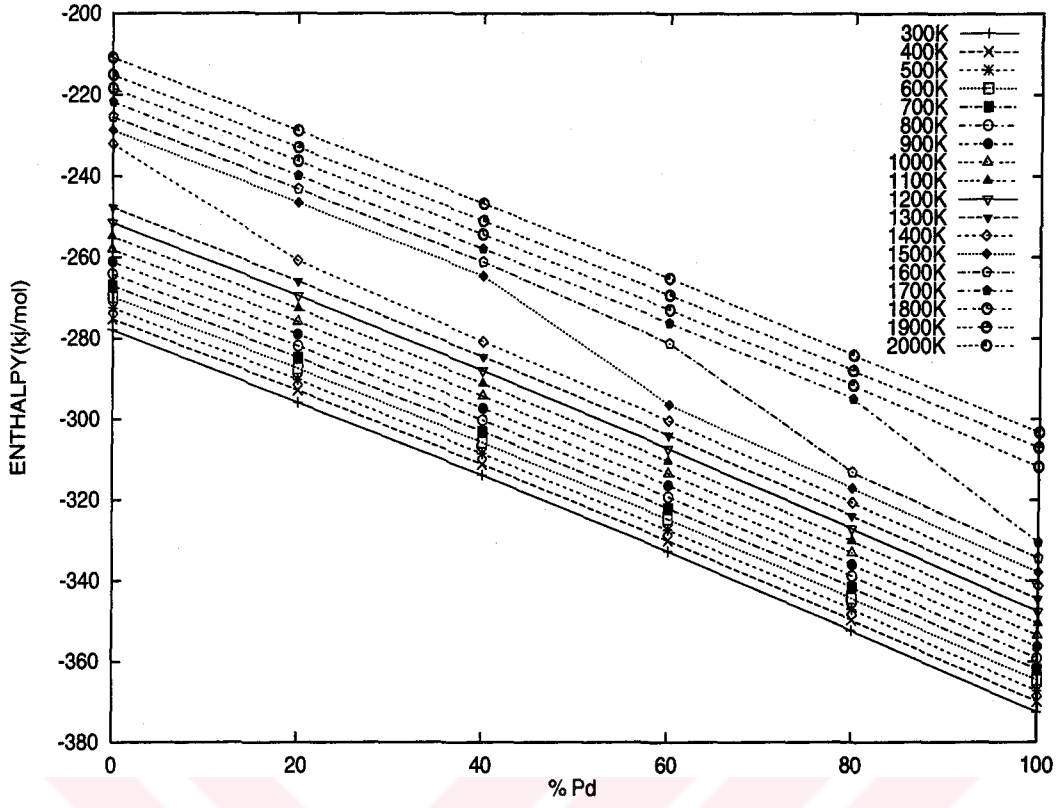

Figure 7.7: Enthalpy of Ag, Pd and their alloys with respect to percentage concentration of Pd in Ag .

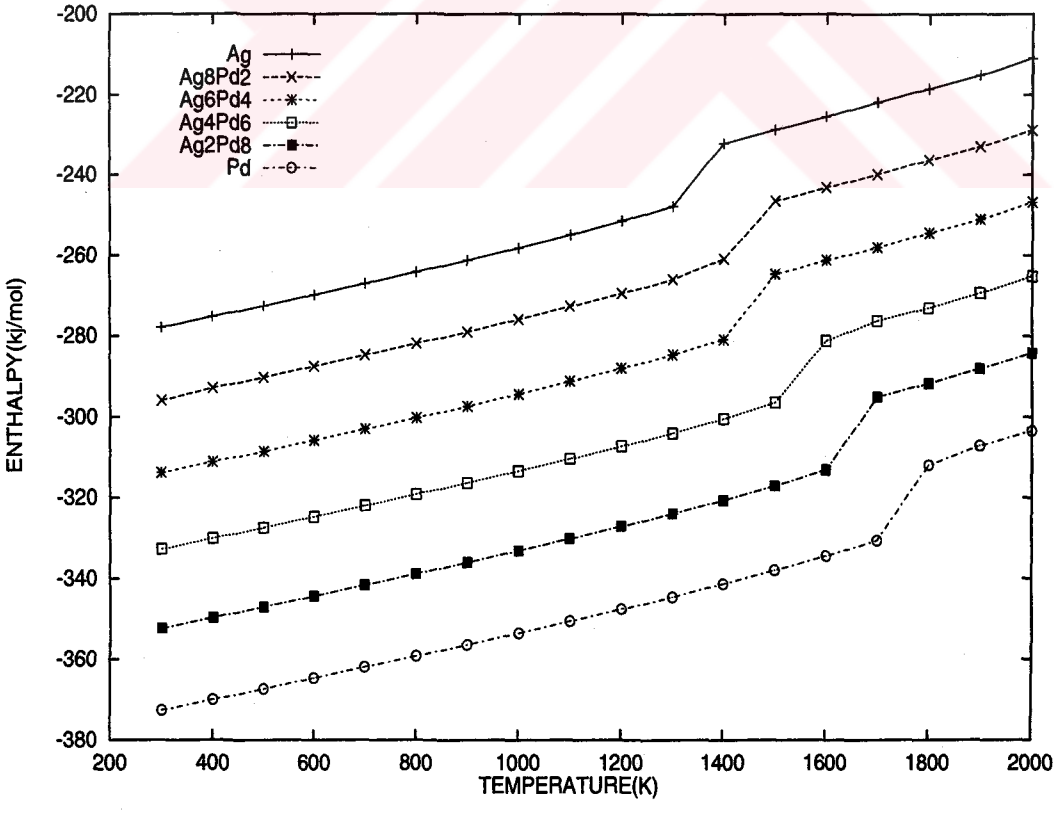

Figure 7.8: Enthalpy of Ag, Pd and their alloys with respect to temperatures ranging from 300K to 2000K.

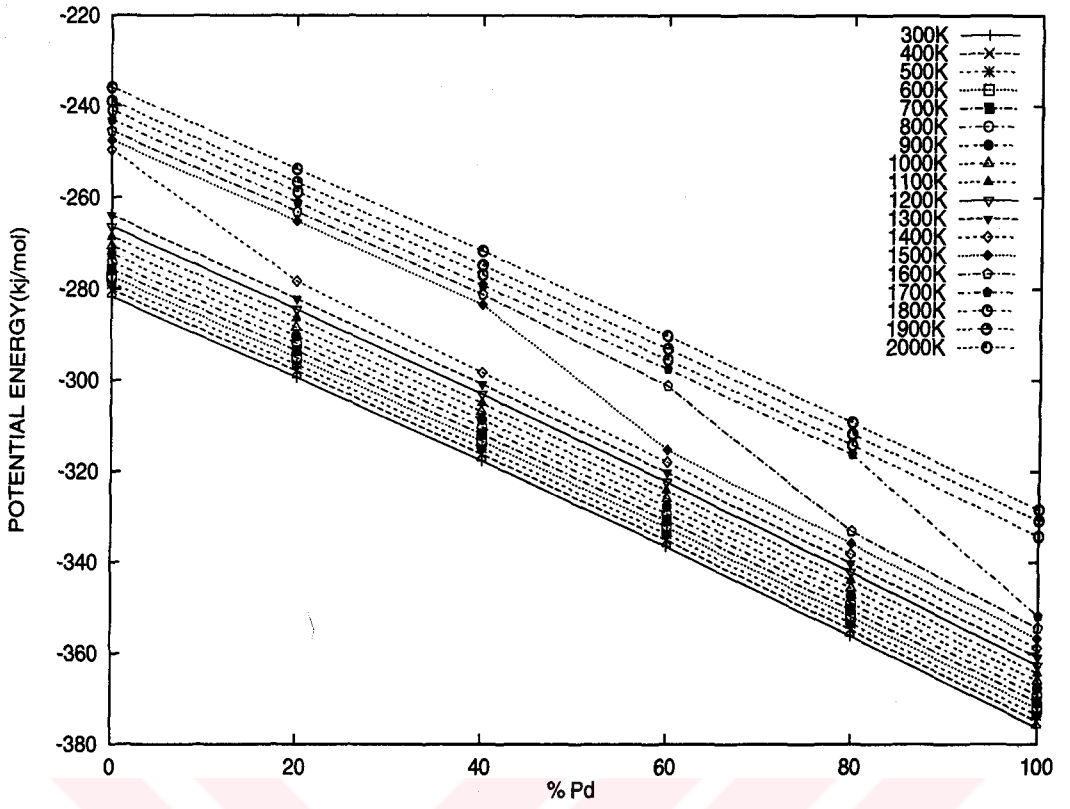

Figure 7.9: Potential energy of Ag, Pd and their alloys with respect to percentage concentration of Pd in Ag .

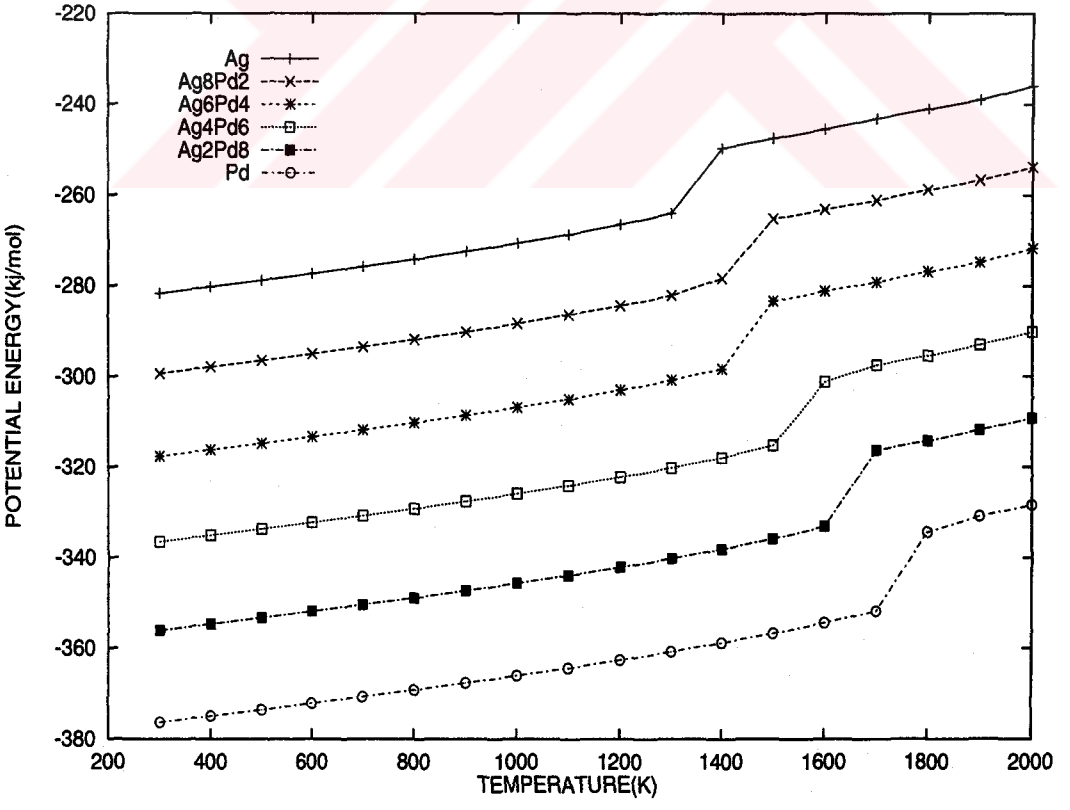

Figure 7.10: Potential energy of Ag, Pd and their alloys with respect to temperatures ranging from 300K to 2000K.

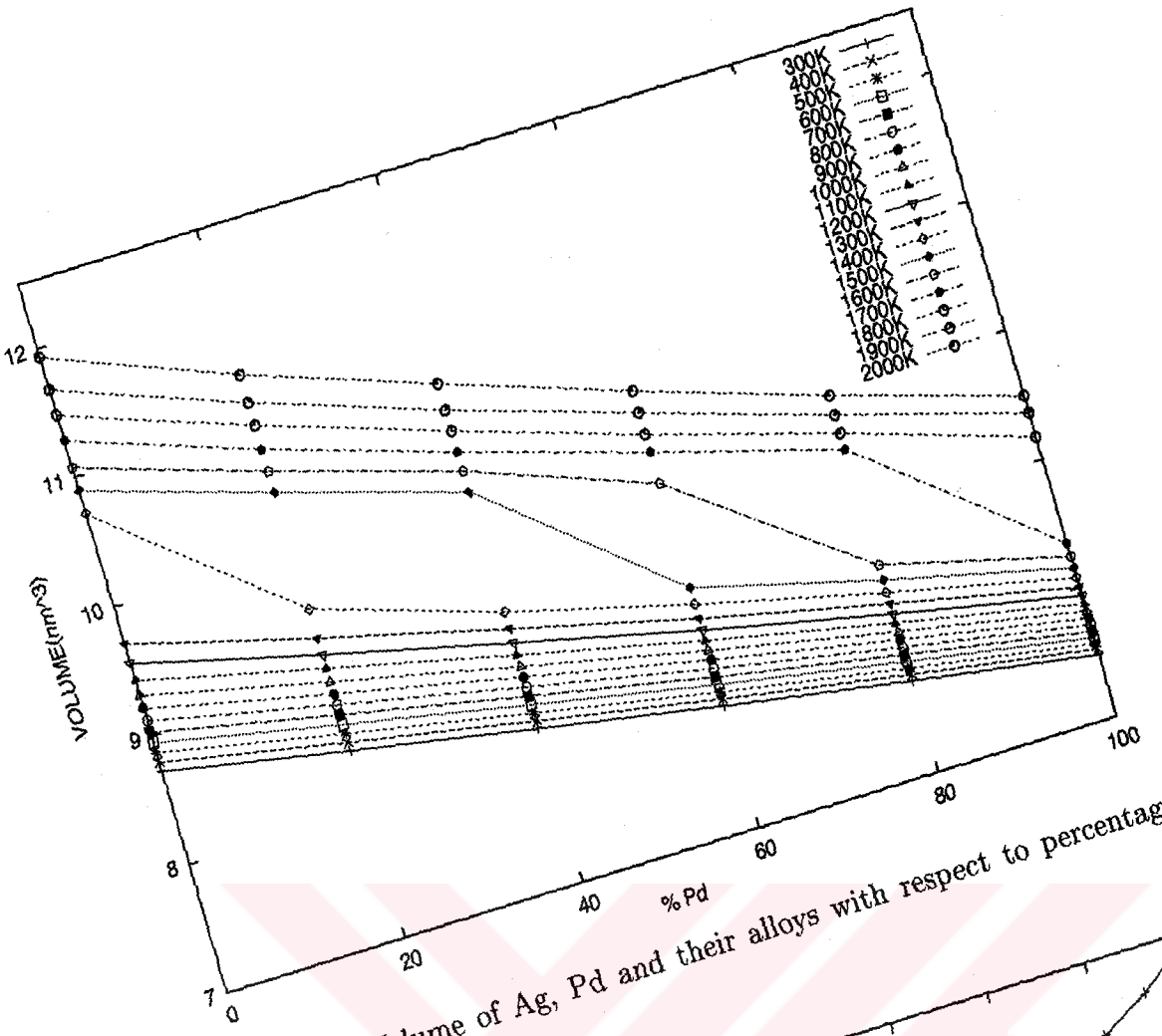

Figure 7.11: Volume of Ag, Pd and their alloys with respect to percentage concentration of Pd in Ag .

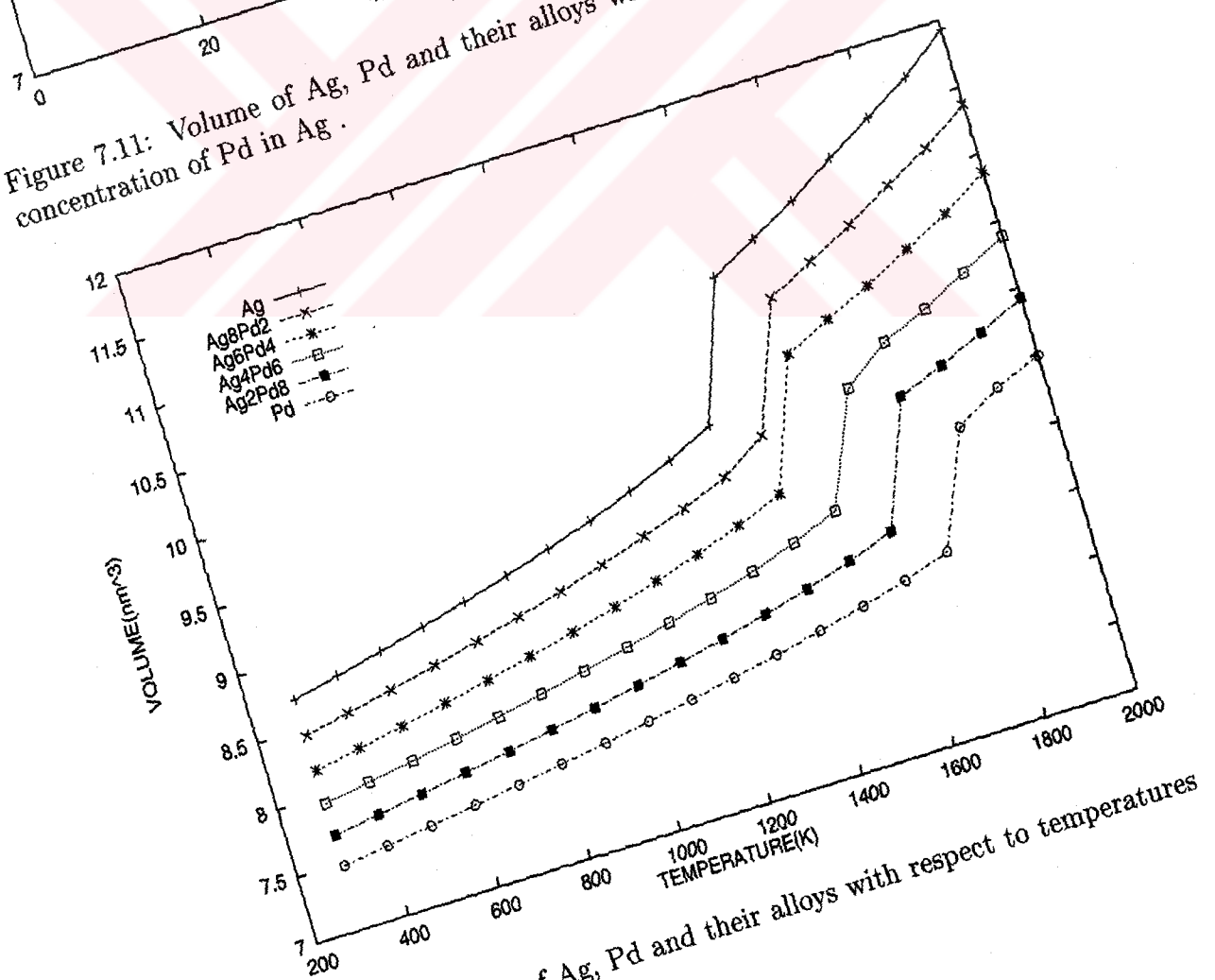

Figure 7.12: Volume of Ag, Pd and their alloys with respect to temperatures ranging from 300K to 2000K.

Table 7.5: The density values in g/cm^3 for the Ag-Pb binary alloy at temperatures ranging from 300K to 1500K as obtained from TPN MD simulation after 20000 steps.

T(K)	Ag	Pb2Ag8	Pb4Ag6	Pb6Ag4	Pb8Ag2	Pb
300	10.2707	10.4774	10.6246	10.7049	10.8128	10.9106
400	10.1873	10.3450	10.4970	10.5398	10.6221	10.7447
500	10.1020	10.2700	10.3318	10.3530	10.4749	10.5644
600	10.0136	10.1575	10.1187	10.0087	9.9590	10.3600
700	9.9214	10.0392	9.8260	9.7851	9.6382	10.0973
800	9.8255	9.9031	9.6098	9.5509	9.4270	9.2025
900	9.7233	9.4379	9.4241	9.3597	9.2095	8.9925
1000	9.6162	9.1856	9.2418	9.1582	8.9915	8.7493
1100	9.4987	9.0201	9.0592	8.9572	8.7840	8.5024
1200	9.3696	8.8768	8.8948	8.7854	8.5774	8.2773
1300	9.2230	8.6893	8.7104	8.5991	8.3753	8.0685
1400	8.3546	8.5528	8.5600	8.3886	8.1577	7.8414
1500	8.2159	8.3812	8.3804	8.2103	7.9441	7.5815

Table 7.6: The enthalpy values in kj/mol for the Ag-Pb binary alloy at temperatures ranging from 300K to 1500K as obtained from TPN MD simulation after 20000 steps.

T(K)	Ag	Pb2Ag8	Pb4Ag6	Pb6Ag4	Pb8Ag2	Pb
300	-277.9558	-255.0577	-235.8665	-218.6117	-202.9729	-189.0484
400	-275.2383	-252.3213	-233.0783	-215.9433	-200.0176	-186.2475
500	-272.5634	-249.6031	-230.2768	-212.8667	-197.2369	-183.3342
600	-269.8308	-246.7813	-226.8306	-208.3630	-191.6382	-180.1940
700	-267.0307	-243.8645	-222.2452	-204.6472	-187.4499	-176.5448
800	-264.1720	-240.7294	-218.3434	-200.8758	-184.1674	-167.5839
900	-261.1898	-233.5544	-214.8487	-197.4992	-180.8318	-164.5836
1000	-258.1359	-228.7830	-211.2781	-194.0142	-177.4949	-161.2977
1100	-254.8961	-225.2472	-207.7638	-190.7667	-174.3438	-158.0237
1200	-251.4571	-222.0002	-204.5054	-187.5482	-171.0846	-154.9791
1300	-247.7127	-218.2101	-201.0268	-184.3479	-167.9424	-151.9752
1400	-232.1080	-214.9813	-197.8778	-180.9561	-165.7136	-148.8658
1500	-228.7469	-211.3756	-194.5402	-177.6777	-161.4432	-145.5736

Table 7.7: The potential energy values in kj/mol for the Ag-Pb binary alloy at temperatures ranging from 300K to 1500K as obtained from TPN MD simulation after 20000 steps.

T(K)	Ag	Pb2Ag8	Pb4Ag6	Pb6Ag4	Pb8Ag2	Pb
300	-281.6993	-258.7662	-239.6064	-222.3738	-206.7151	-192.7896
400	-280.2294	-257.3113	-238.0667	-220.9323	-205.1637	-191.2361
500	-278.8016	-255.8378	-236.5131	-219.1017	-203.4729	-189.5681
600	-277.3153	-254.2636	-234.3137	-215.8450	-199.1214	-187.6770
700	-275.7614	-252.5949	-230.9746	-213.3776	-196.1800	-185.2557
800	-274.1456	-250.7061	-228.3210	-210.8522	-194.1457	-177.5602
900	-272.4145	-244.7780	-226.0739	-208.7243	-192.0576	-175.8075
1000	-270.6081	-241.2554	-223.7494	-206.4857	-189.9660	-173.7684
1100	-268.6152	-238.9651	-221.4828	-204.4848	-188.0623	-171.7413
1200	-266.4230	-236.9673	-219.4715	-202.5154	-186.0489	-169.9456
1300	-263.9270	-234.4227	-217.2410	-200.5622	-184.1547	-168.1888
1400	-249.5681	-232.4399	-215.3365	-198.4167	-182.1755	-166.3264
1500	-247.4536	-230.0820	-213.2494	-196.3854	-180.1507	-164.2761

Table 7.8: The volume values in nm^3 for the Ag-Pb binary alloy at temperatures ranging from 300K to 1500K as obtained from TPN MD simulation after 20000 steps.

T(K)	Ag	Pb2Ag8	Pb4Ag6	Pb6Ag4	Pb8Ag2	Pb
300	8.7194	10.1215	11.5337	12.9874	14.3837	15.7665
400	8.7907	10.2215	11.6739	13.1913	14.6006	16.0099
500	8.8650	10.3259	11.8605	13.4293	14.8477	16.2830
600	8.9433	10.4403	12.1103	13.8914	15.6169	16.6043
700	9.0263	10.5633	12.4711	14.2087	16.1367	17.0363
800	9.1144	10.7085	12.7517	14.5573	16.4981	18.6928
900	9.2103	11.2363	13.0029	14.8546	16.8877	19.1295
1000	9.3128	11.5449	13.2594	15.1814	17.2972	19.6612
1100	9.4280	11.7568	13.5266	15.5221	17.7057	20.2320
1200	9.5579	11.9466	13.7767	15.8256	18.1323	20.7822
1300	9.7098	12.2043	14.0684	16.1685	18.5699	21.3200
1400	10.7192	12.3991	14.3155	16.5742	19.0651	21.9376
1500	10.9001	12.6530	14.6223	16.9342	19.5779	22.6896

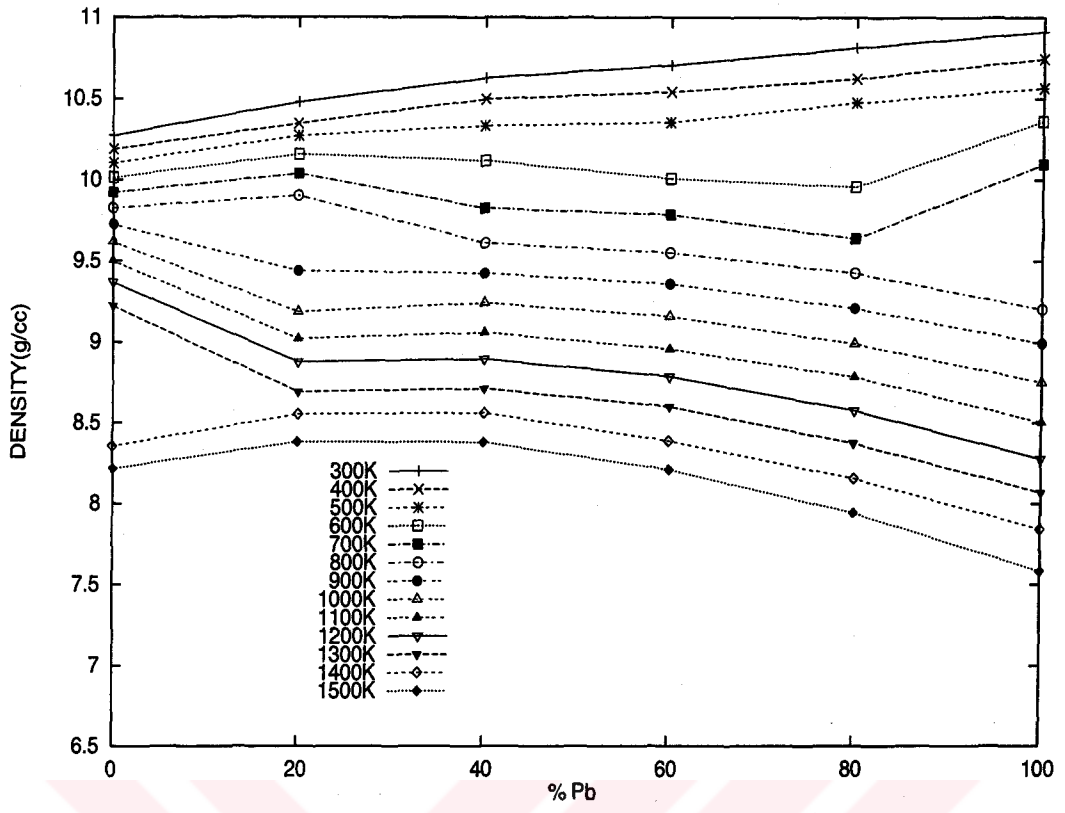

Figure 7.13: Density of Ag, Pb and their alloys with respect to percentage concentration of Pb in Ag .

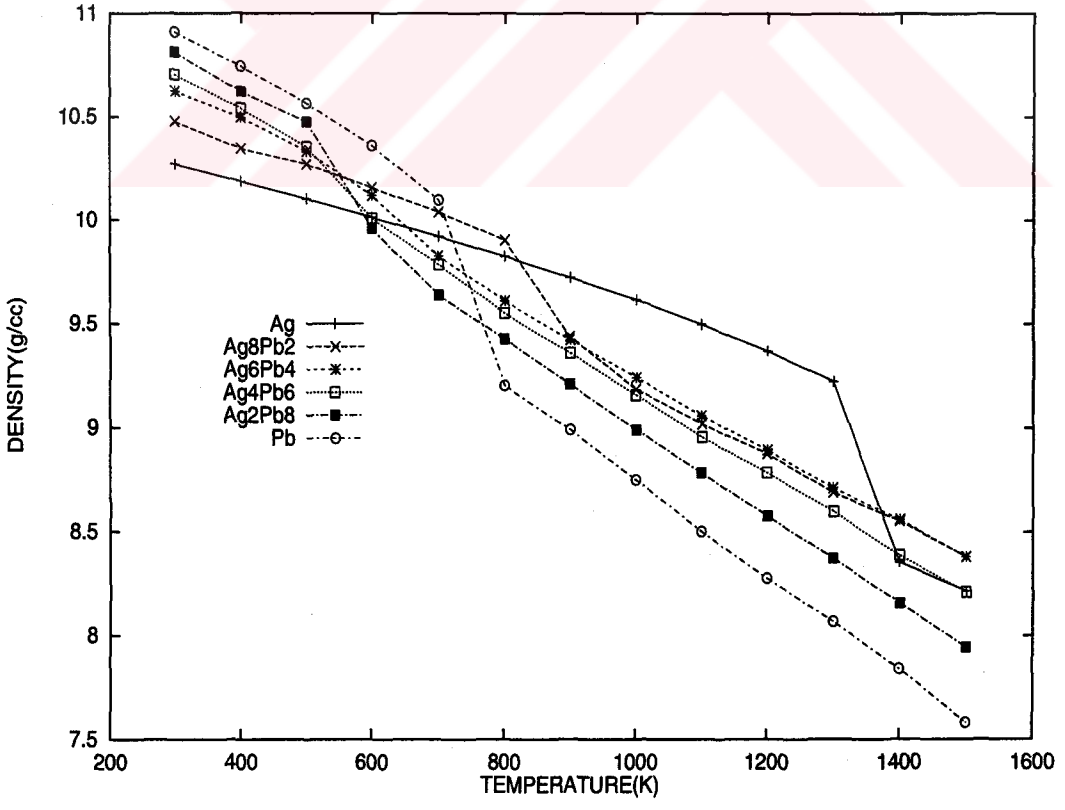

Figure 7.14: Density of Ag, Pb and their alloys with respect to temperatures ranging from 300K to 1500K.

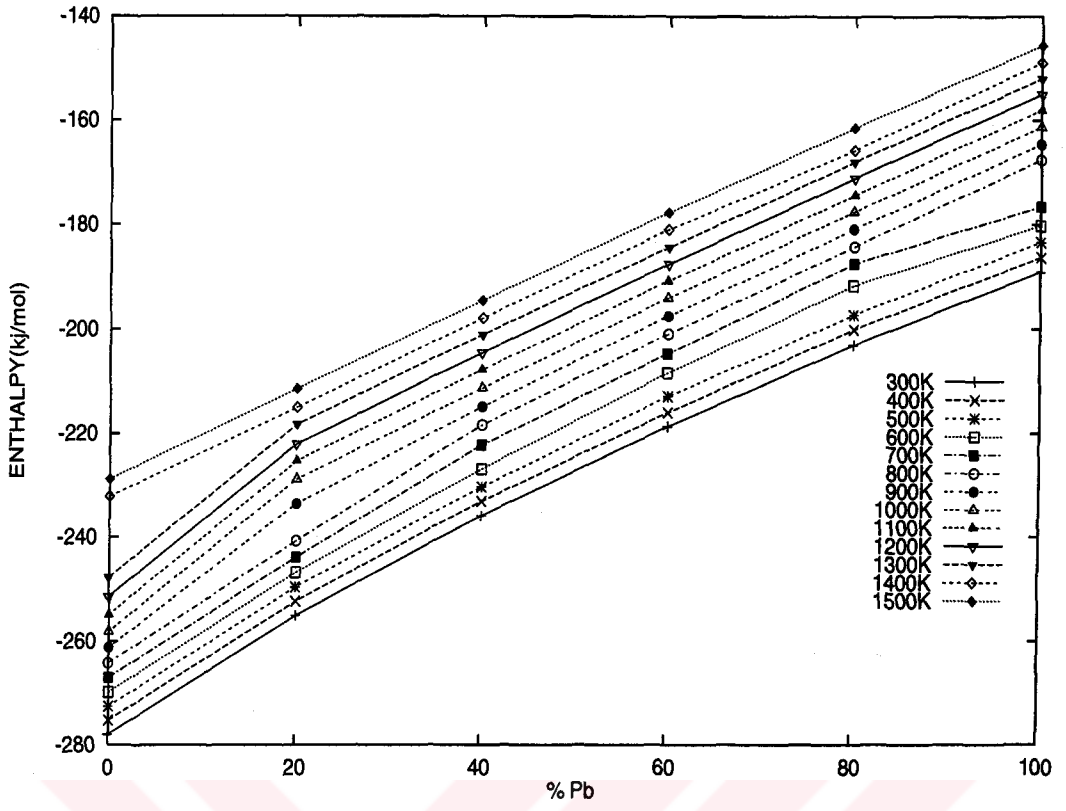

Figure 7.15: Enthalpy of Ag, Pb and their alloys with respect to percentage concentration of Pb in Ag .

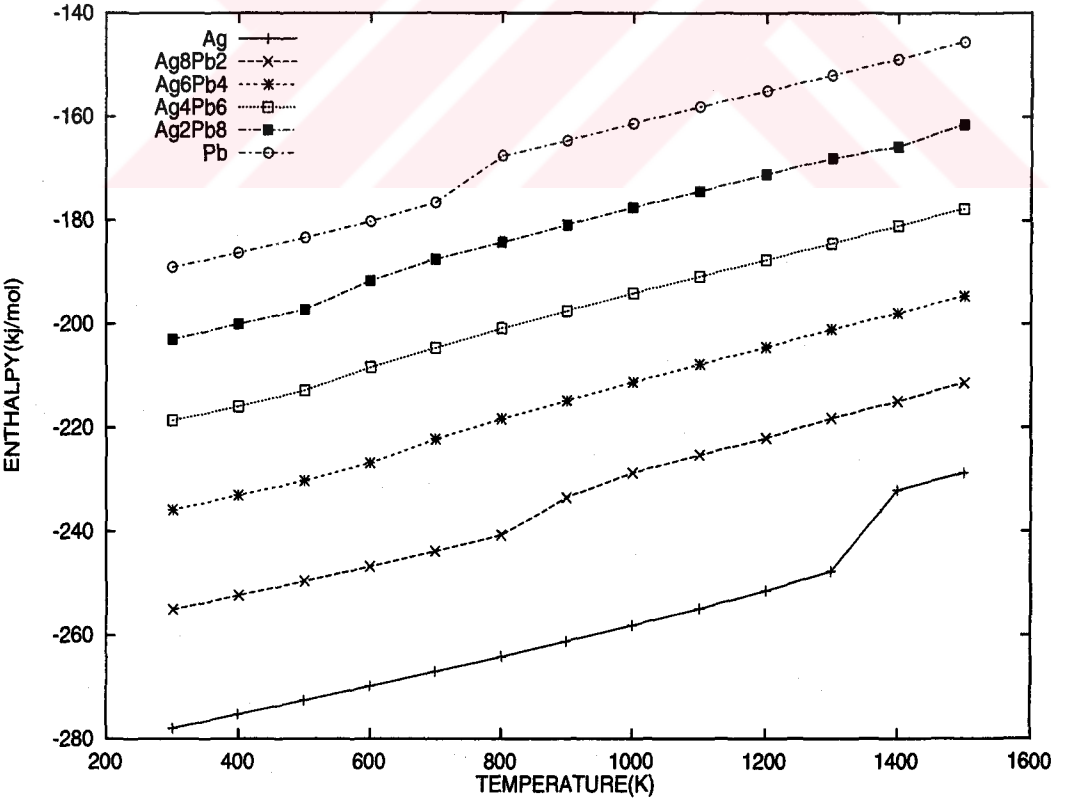

Figure 7.16: Enthalpy of Ag, Pb and their alloys with respect to temperatures ranging from 300K to 1500K.

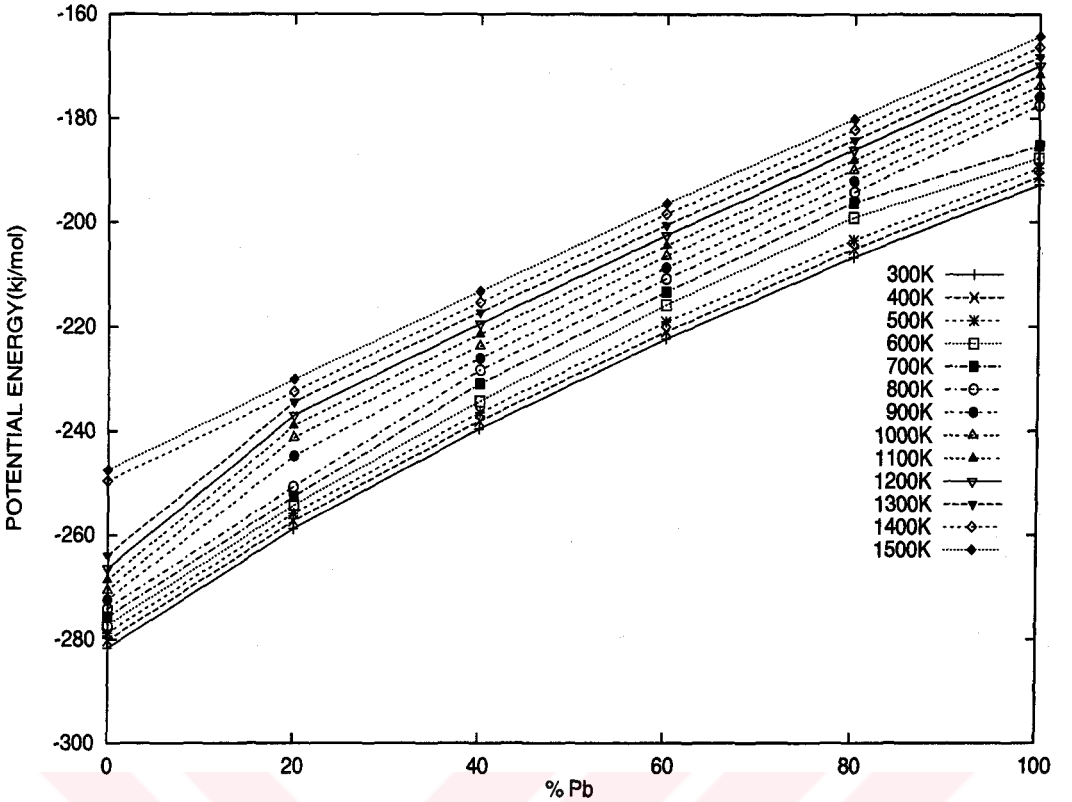

Figure 7.17: Potential energy of Ag, Pb and their alloys with respect to percentage concentration of Pb in Ag .

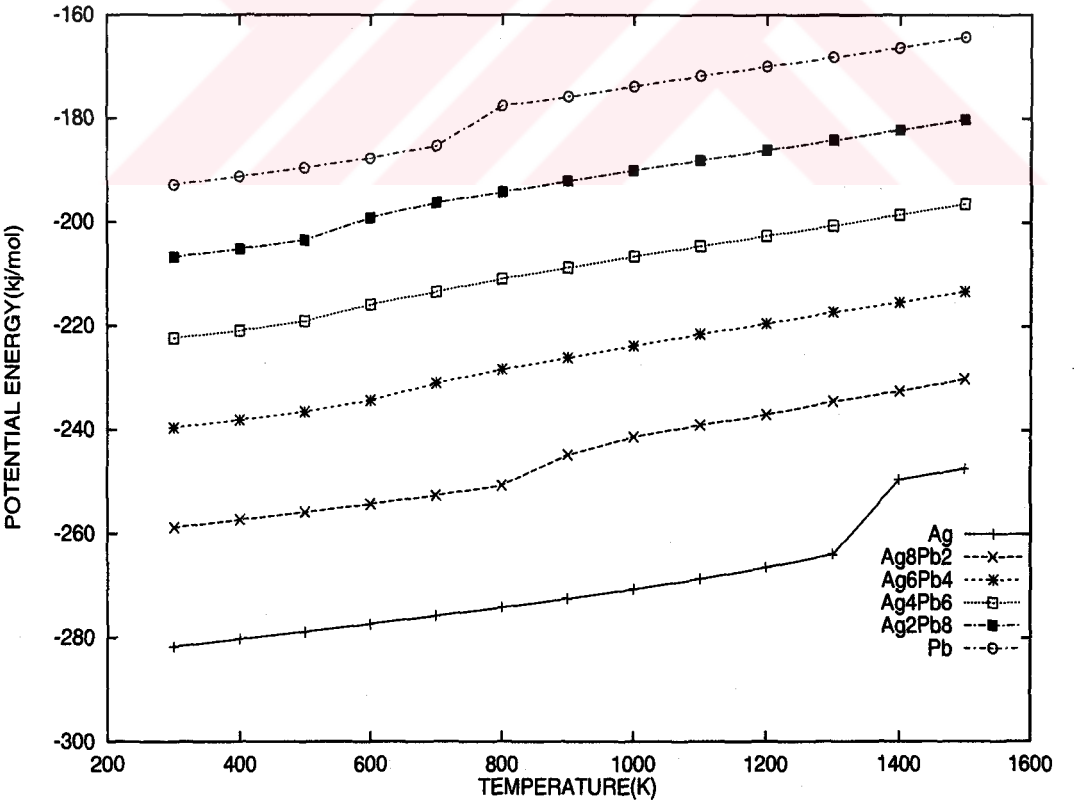

Figure 7.18: Potential energy of Ag, Pb and their alloys with respect to temperatures ranging from 300K to 1500K.

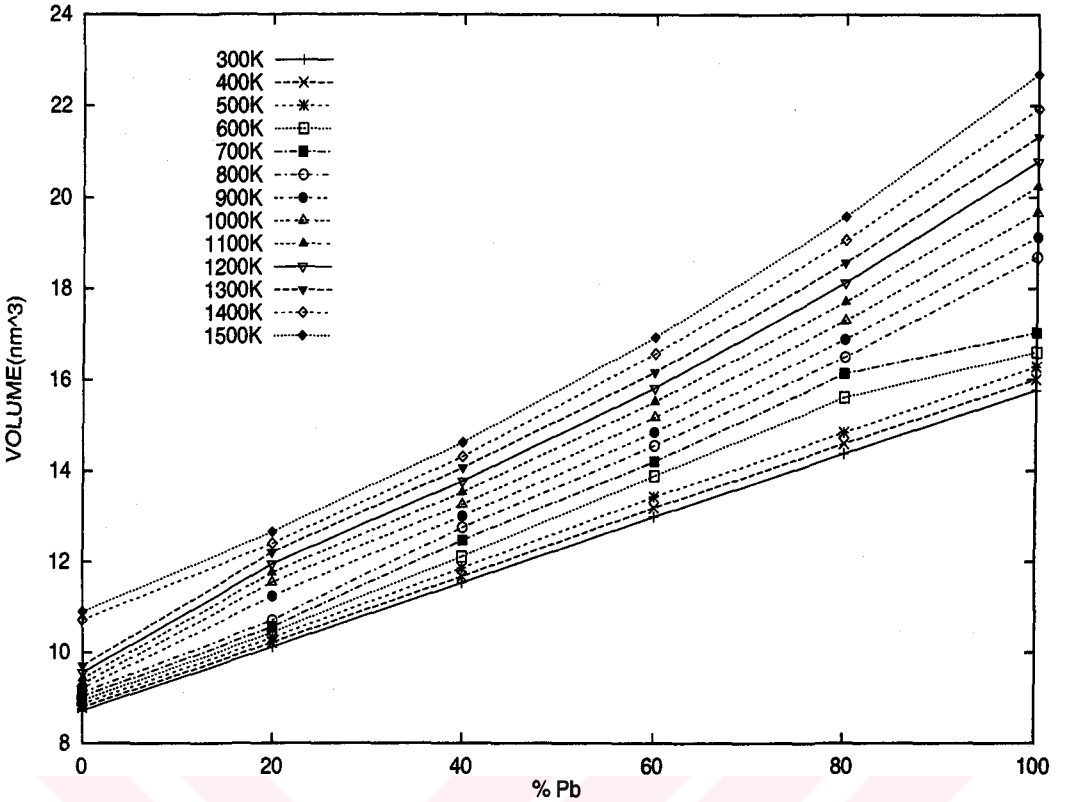

Figure 7.19: Volume of Ag, Pb and their alloys with respect to percentage concentration of Pb in Ag .

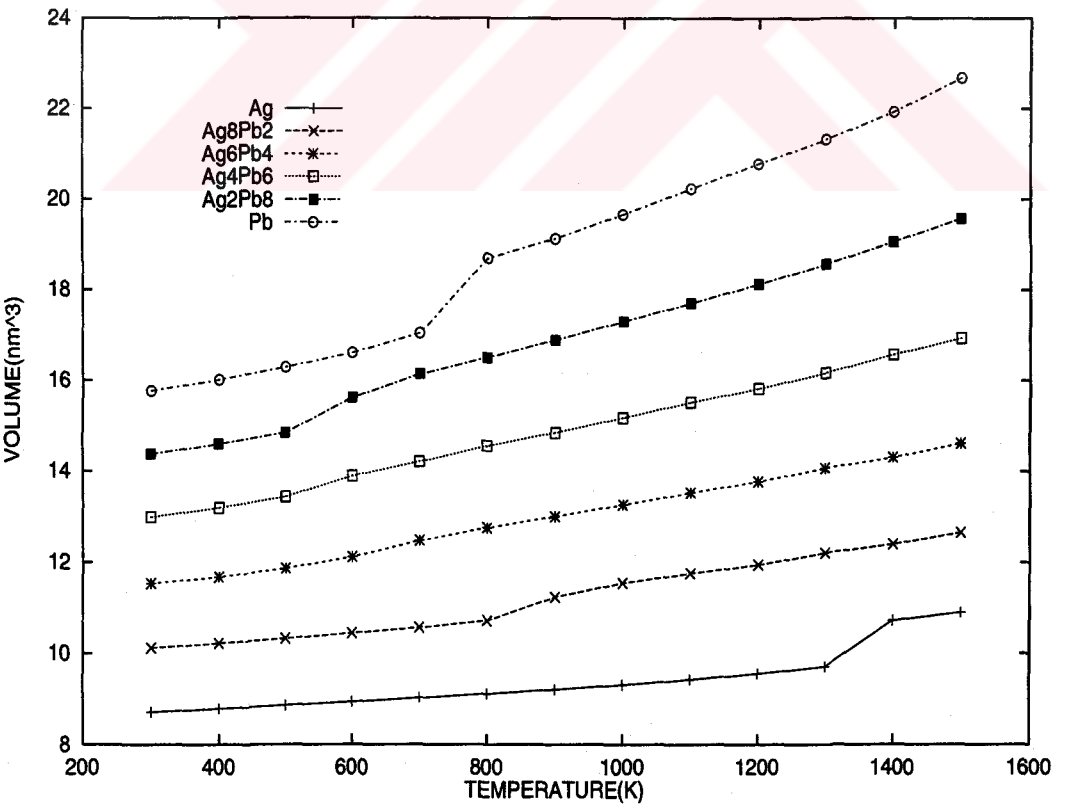

Figure 7.20: Volume of Ag, Pb and their alloys with respect to temperatures ranging from 300K to 1500K.

Table 7.9: The density values in g/cm^3 for the Ag-Cu binary alloy at temperatures ranging from 300K to 1500K as obtained from TPN MD simulation after 20000 steps.

T(K)	Ag	Cu2Ag8	Cu4Ag6	Cu6Ag4	Cu8Ag2	Cu
300	10.2707	9.9660	9.6675	9.3696	9.0534	8.7218
400	10.1873	9.8843	9.5869	9.2910	8.9773	8.6489
500	10.1020	9.7993	9.5027	9.2090	8.8973	8.5728
600	10.0136	9.7112	9.4148	9.1227	8.8151	8.4941
700	9.9214	9.6195	9.3232	9.0315	8.7268	8.4115
800	9.8255	9.5221	9.2239	8.8887	8.6326	8.3242
900	9.7233	9.4177	9.0483	8.5966	8.5296	8.2299
1000	9.6162	9.3051	8.6425	8.4094	8.1175	8.1280
1100	9.4987	9.1741	8.5133	8.2800	7.9727	7.8516
1200	9.3696	8.5506	8.3724	8.1615	7.8576	7.4774
1300	9.2230	8.3926	8.2429	8.0311	7.7522	7.3773
1400	8.3546	8.2603	8.1243	7.9187	7.6447	7.2750
1500	8.2159	8.1299	7.9962	7.8040	7.5263	7.1772

Table 7.10: The enthalpy values in kj/mol for the Ag-Cu binary alloy at temperatures ranging from 300K to 1500K as obtained from TPN MD simulation after 20000 steps.

T(K)	Ag	Cu2Ag8	Cu4Ag6	Cu6Ag4	Cu8Ag2	Cu
300	-277.9558	-287.1141	-297.0912	-307.6548	-318.4409	-329.8941
400	-275.2383	-284.5081	-294.4815	-305.0455	-315.8309	-327.2963
500	-272.5634	-281.8261	-291.7842	-302.3438	-313.1260	-324.5994
600	-269.8308	-278.4826	-289.0179	-299.5578	-310.3666	-321.8525
700	-267.0307	-276.2761	-286.1878	-296.6924	-307.4974	-319.0224
800	-264.1720	-273.3698	-283.2127	-292.8850	-304.5167	-316.1024
900	-261.1898	-270.3447	-278.9506	-286.5828	-301.3520	-313.0325
1000	-258.1359	-267.1668	-270.8681	-281.9782	-292.5366	-309.8119
1100	-254.8961	-263.6760	-267.4396	-278.5859	-288.6733	-303.2065
1200	-251.4571	-252.0630	-263.8408	-275.2737	-285.4053	-294.6124
1300	-247.7127	-248.2127	-260.4237	-271.7259	-282.3081	-291.6015
1400	-232.1080	-244.9085	-257.1339	-268.5297	-279.1407	-288.4868
1500	-228.7469	-241.5325	-253.7156	-265.2988	-275.6970	-285.4606

Table 7.11: The potential energy values in kj/mol for the Ag-Cu binary alloy at temperatures ranging from 300K to 1500K as obtained from TPN MD simulation after 20000 steps.

T(K)	Ag	Cu2Ag8	Cu4Ag6	Cu6Ag4	Cu8Ag2	Cu
300	-281.6993	-290.8569	-300.8334	-311.3981	-322.1834	-333.6365
400	-280.2294	-289.4965	-299.4682	-310.0303	-320.8202	-332.2840
500	-278.8016	-288.0611	-298.0210	-308.5758	-319.3607	-330.8369
600	-277.3153	-286.5670	-296.5014	-307.0431	-317.8511	-329.3365
700	-275.7614	-285.0068	-294.9109	-305.4220	-316.2274	-327.7517
800	-274.1456	-283.3468	-293.1901	-302.8623	-314.4928	-326.0804
900	-272.4145	-281.5692	-290.1765	-297.8081	-312.5773	-324.2590
1000	-270.6081	-279.6383	-283.3394	-294.4494	-305.0086	-322.2846
1100	-268.6152	-277.3951	-281.1581	-292.3048	-302.3908	-316.9253
1200	-266.4230	-267.0300	-278.8069	-290.2412	-300.3701	-309.5793
1300	-263.9270	-264.4254	-276.6356	-287.9408	-298.5177	-307.8141
1400	-249.5681	-262.3674	-274.5931	-285.9896	-296.5999	-305.9469
1500	-247.4536	-260.2400	-272.4217	-284.0054	-294.4047	-304.1677

Table 7.12: The volume values in nm^3 for the Ag-Cu binary alloy at temperatures ranging from 300K to 1500K as obtained from TPN MD simulation after 20000 steps.

T(K)	Ag	Cu2Ag8	Cu4Ag6	Cu6Ag4	Cu8Ag2	Cu
300	8.7194	8.2475	7.7409	7.2016	6.6402	6.0489
400	8.7907	8.3157	7.8060	7.2625	6.6965	6.0998
500	8.8650	8.3878	7.8751	7.3272	6.7567	6.1540
600	8.9433	8.4639	7.9487	7.3965	6.8197	6.2110
700	9.0263	8.5446	8.0268	7.4711	6.8887	6.2720
800	9.1144	8.6319	8.1132	7.5912	6.9639	6.3378
900	9.2103	8.7277	8.2706	7.8491	7.0480	6.4104
1000	9.3128	8.8333	8.6590	8.0238	7.4058	6.4908
1100	9.4280	8.9595	8.7904	8.1493	7.5403	6.7192
1200	9.5579	9.6127	8.9384	8.2676	7.6508	7.0549
1300	9.7098	9.7937	9.0788	8.4018	7.7548	7.1513
1400	10.7192	9.9505	9.2113	8.5211	7.8638	7.2518
1500	10.9001	10.1101	9.3588	8.6464	7.9875	7.3506

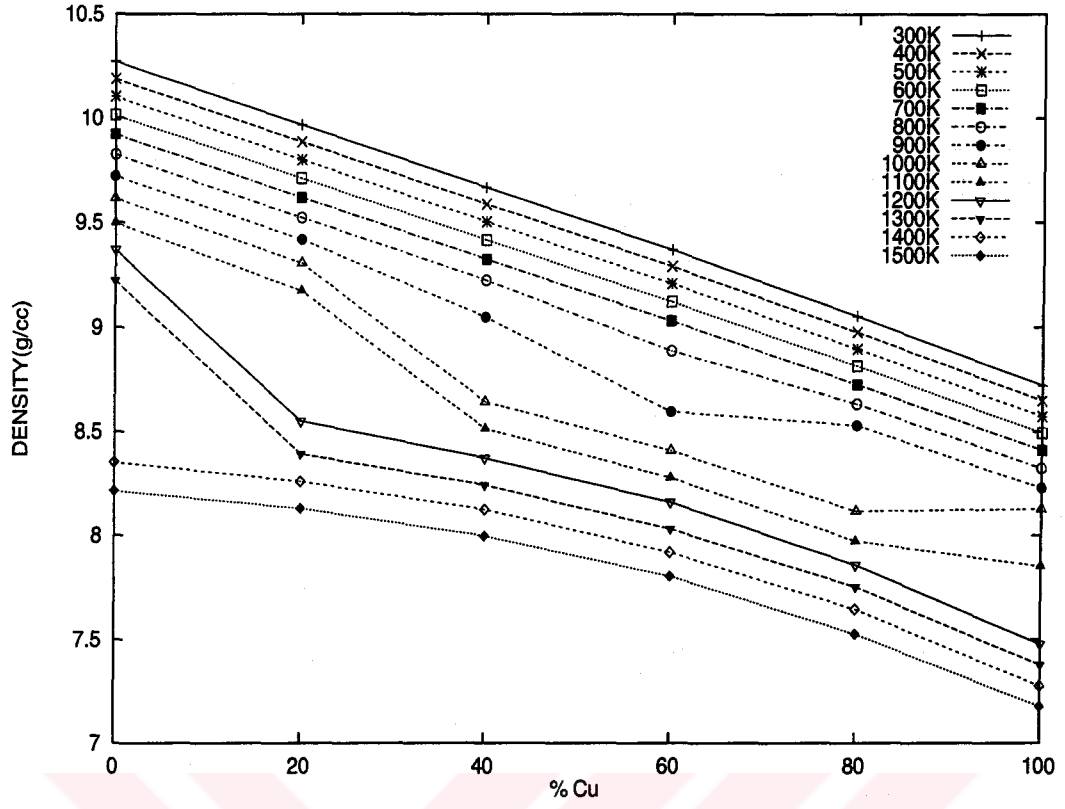

Figure 7.21: Density of Ag, Cu and their alloys with respect to percentage concentration of Cu in Ag .

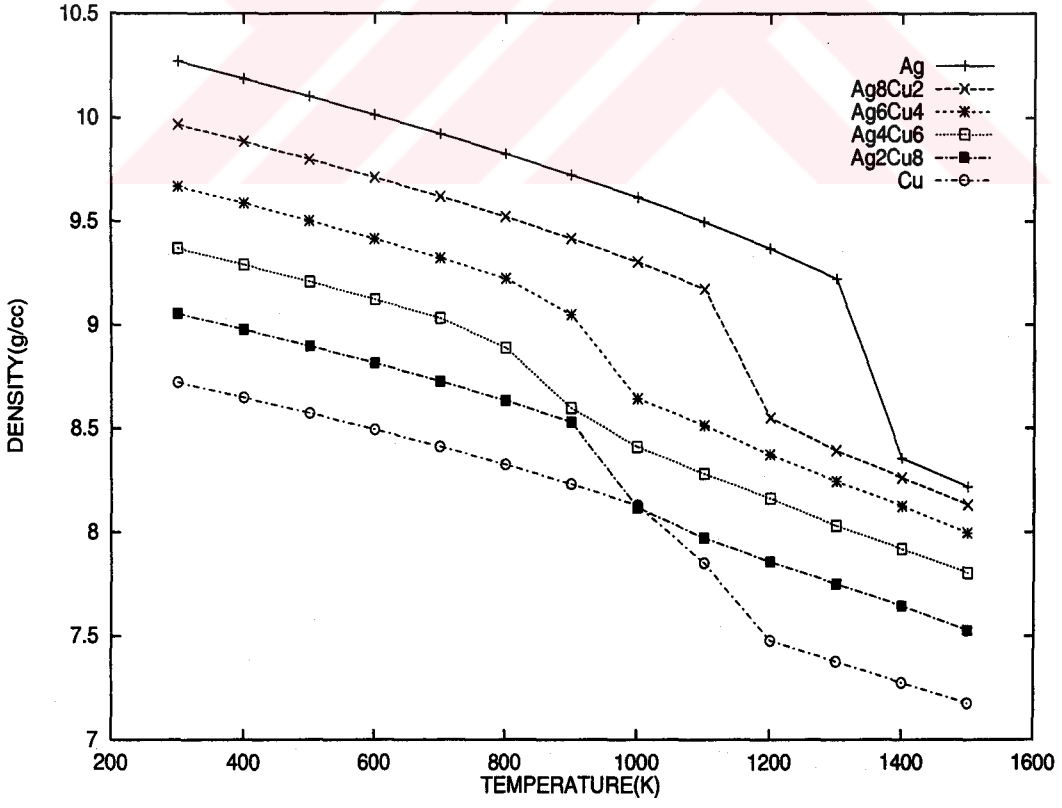

Figure 7.22: Density of Ag, Cu and their alloys with respect to temperatures ranging from 300K to 1500K.

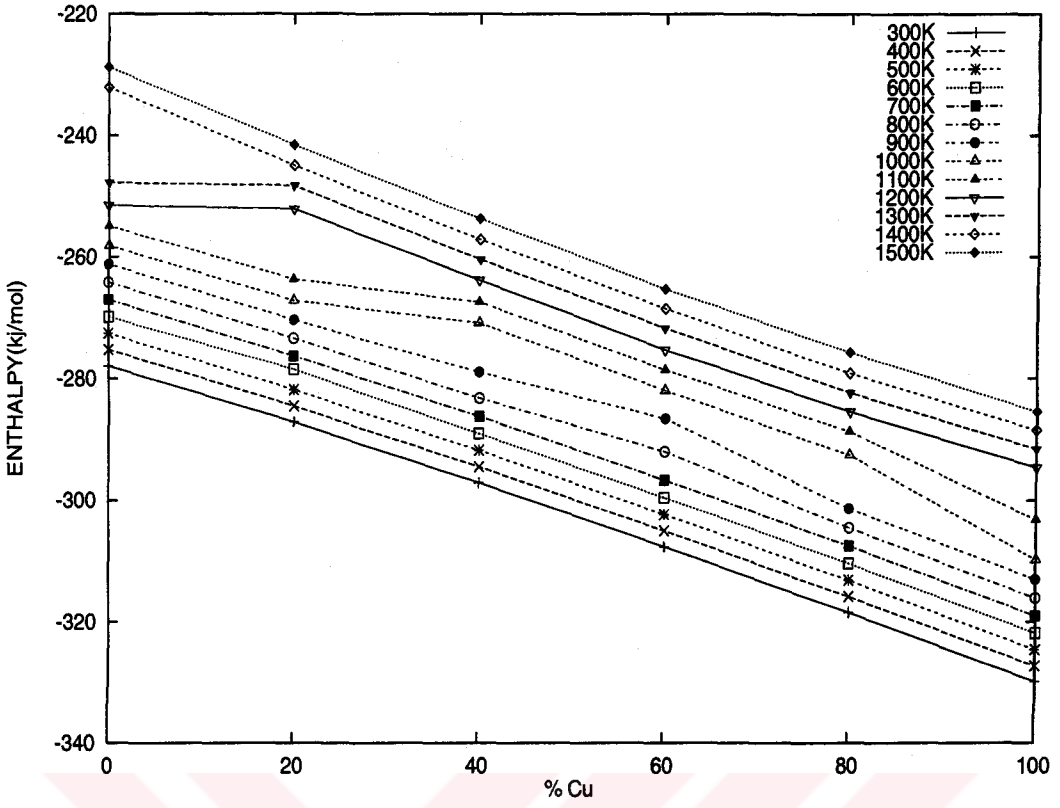

Figure 7.23: Enthalpy of Ag, Cu and their alloys with respect to percentage concentration of Cu in Ag .

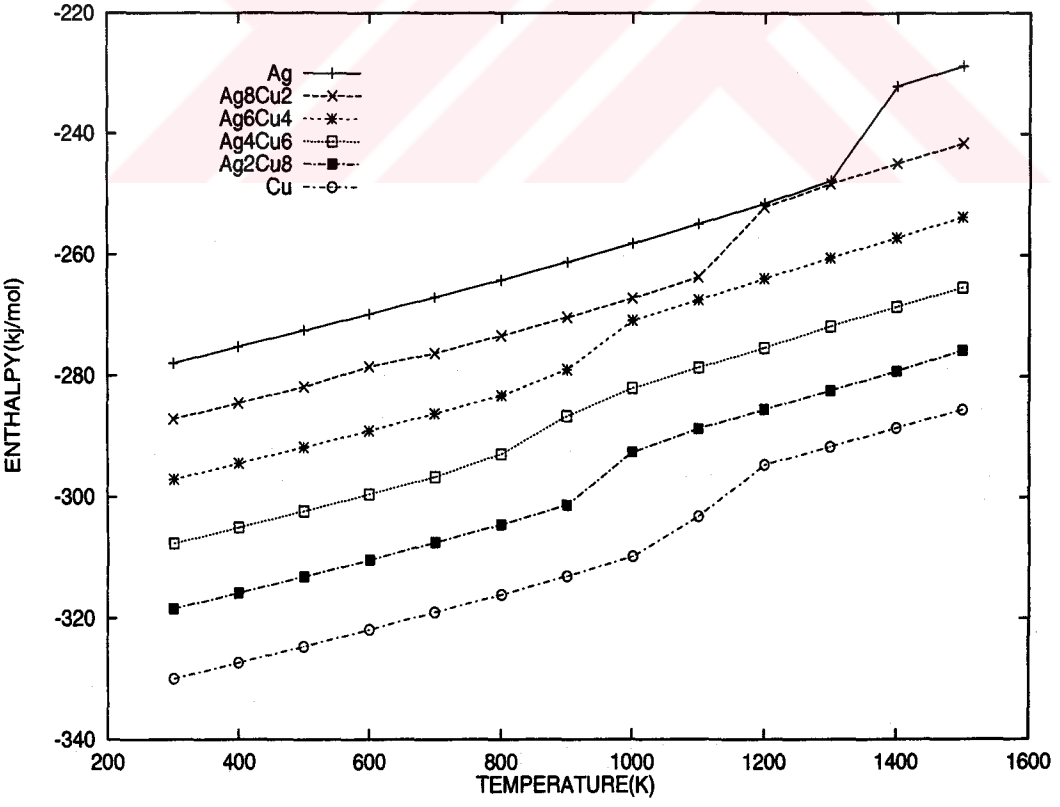

Figure 7.24: Enthalpy of Ag, Cu and their alloys with respect to temperatures ranging from 300K to 1500K.

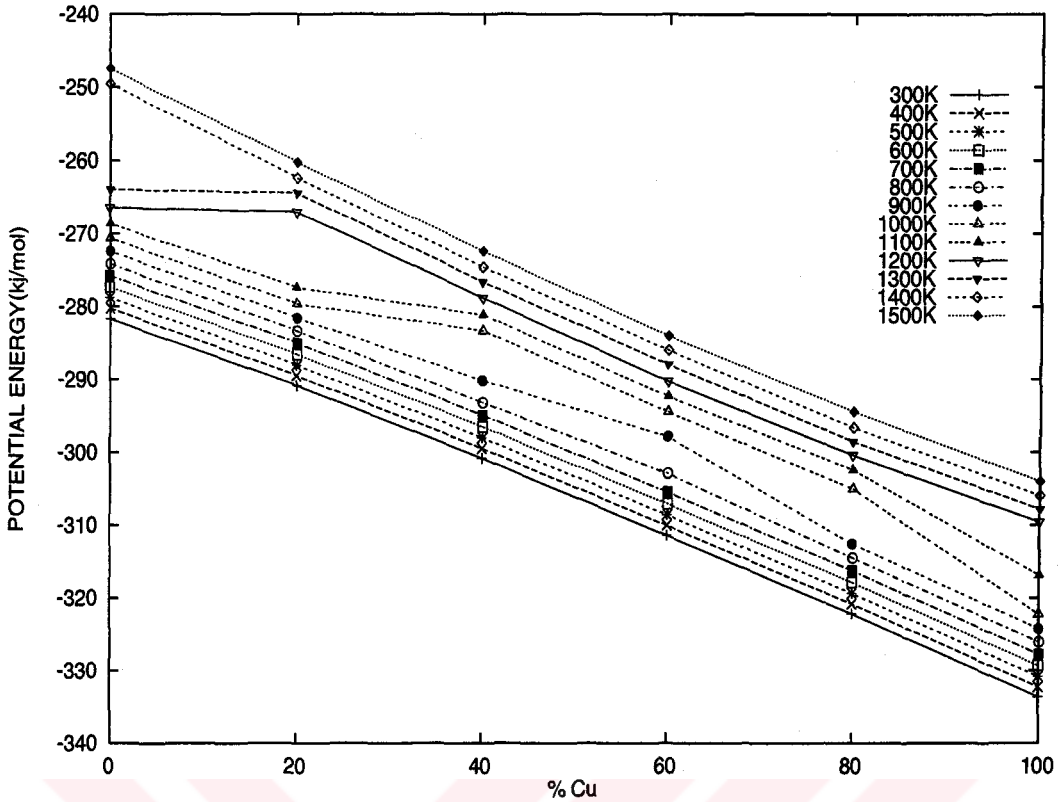

Figure 7.25: Potential energy of Ag, Cu and their alloys with respect to percentage concentration of Cu in Ag .

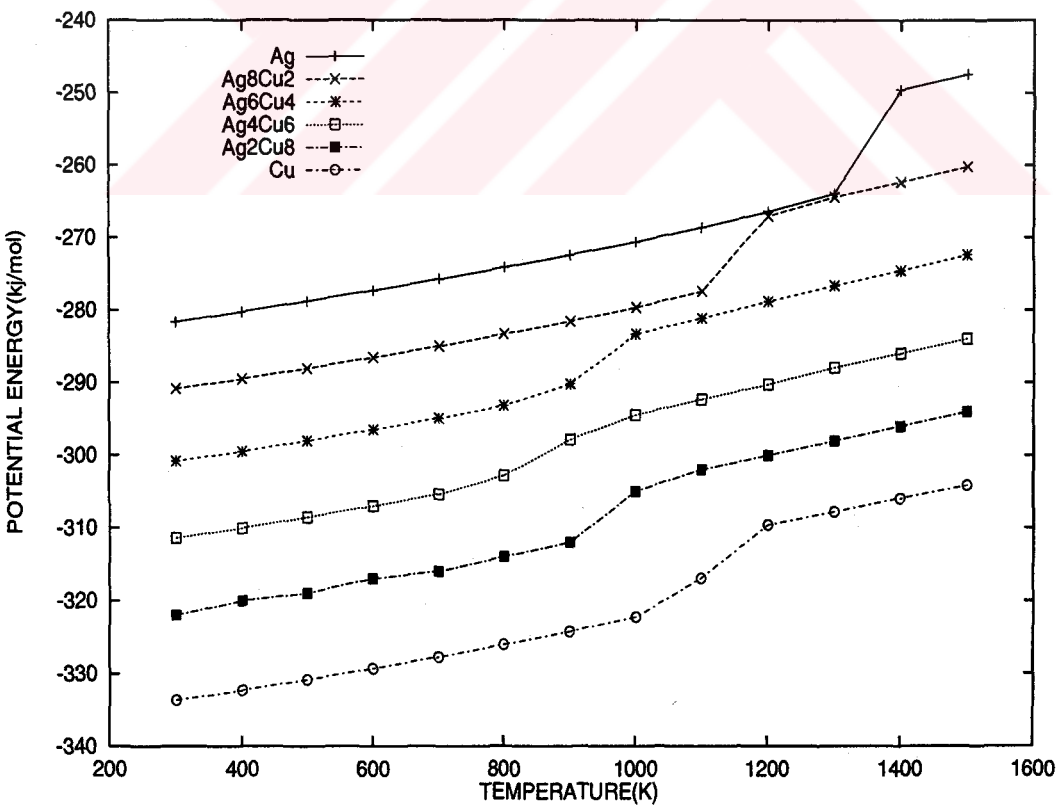

Figure 7.26: Potential energy of Ag, Cu and their alloys with respect to temperatures ranging from 300K to 1500K.

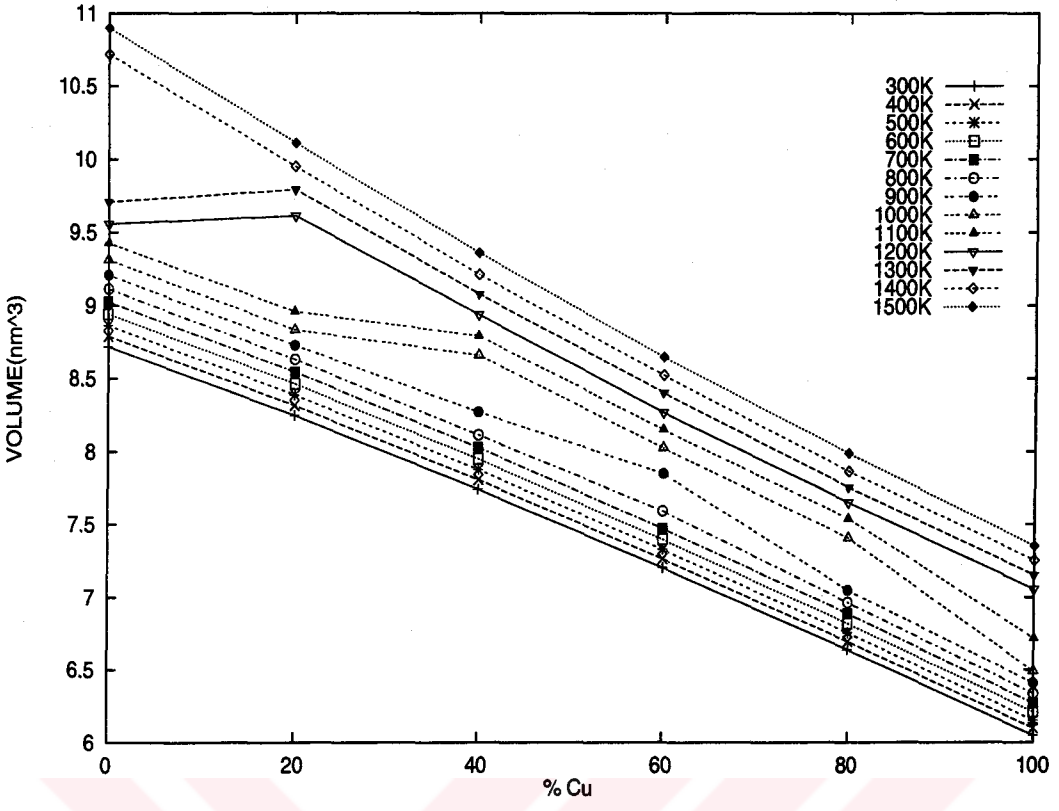

Figure 7.27: Volume of Ag, Cu and their alloys with respect to percentage concentration of Cu in Ag .

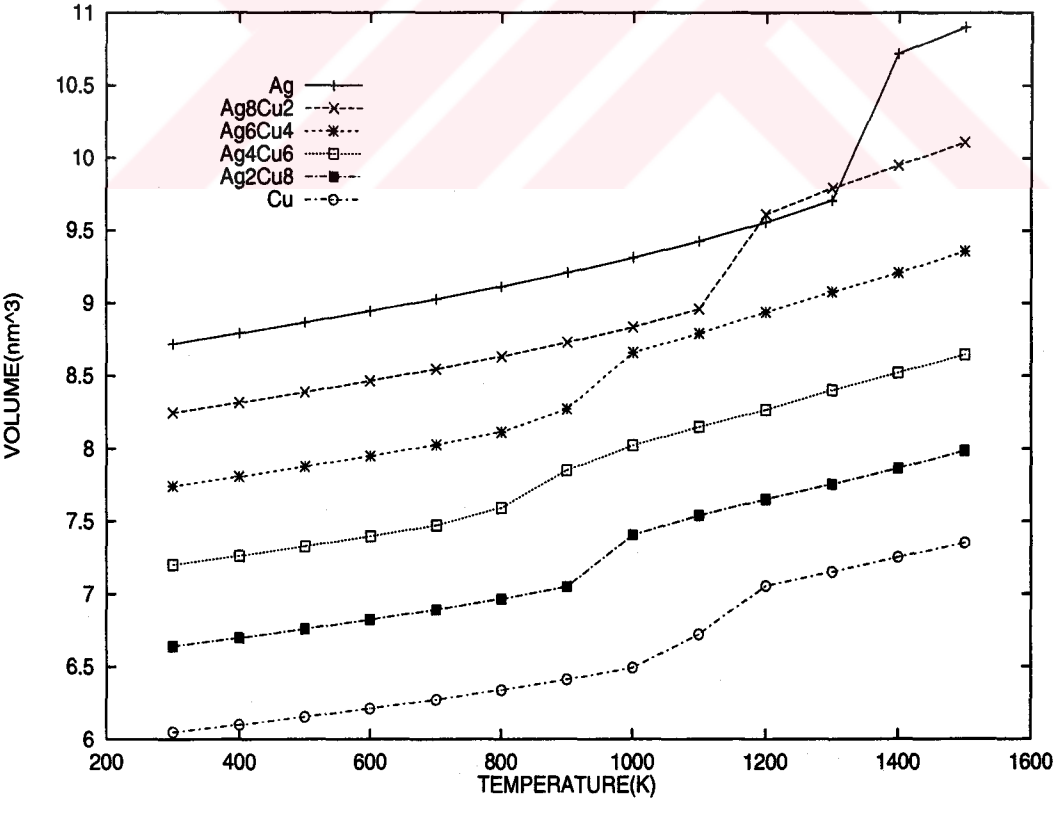

Figure 7.28: Volume of Ag, Cu and their alloys with respect to temperatures ranging from 300K to 1500K.

Table 7.13: The lattice distance in $\AA$ for the Ag-Pd binary alloy at temperatures ranging from 300K to 2000K .

T(K)	Ag	Pd2Ag8	Pd4Ag6	Pd6Ag4	Pd8Ag2	Pd
300	4.1165	4.0735	4.0315	3.9905	3.9505	3.9112
400	4.1277	4.0841	4.0412	3.9995	3.9587	3.9187
500	4.1393	4.0947	4.0510	4.0086	3.9671	3.9264
600	4.1514	4.1061	4.0615	4.0181	3.9758	3.9343
700	4.1642	4.1180	4.0723	4.0280	3.9848	3.9425
800	4.1777	4.1304	4.0839	4.0385	3.9943	3.9510
900	4.1923	4.1433	4.0959	4.0495	4.0043	3.9599
1000	4.2078	4.1581	4.1089	4.0612	4.0146	3.9692
1100	4.2251	4.1744	4.1229	4.0735	4.0257	3.9791
1200	4.2444	4.1905	4.1379	4.0866	4.0373	3.9894
1300	4.2668	4.2098	4.1550	4.1008	4.0501	4.0004
1400	4.4098	4.2437	4.1751	4.1184	4.0639	4.0126
1500	4.4345	4.3737	4.3133	4.1388	4.0796	4.0252
1600	4.4584	4.3964	4.3361	4.2612	4.0984	4.0396
1700	4.4866	4.4196	4.3570	4.2963	4.2364	4.0563
1800	4.5124	4.4450	4.3800	4.3163	4.2550	4.1864
1900	4.5380	4.4687	4.4023	4.3406	4.2758	4.2146
2000	4.5705	4.4975	4.4302	4.3642	4.2980	4.2345

The lattice distance values are calculated using the values of volumes as $a = \sqrt[3]{V}$. These can be seen in Tables 7.13, 7.14 and 7.15 and in Figures 7.29, 7.30, 7.31, 7.32, 7.33 and 7.34. Although in liquid phases lattice distance can not be defined, they are represented in order to see changes when the alloys melt.

At room temperatures, the lattice constants of Ag, Pd, Pb and Cu are 4.09, 3.89, 4.95 and 3.61 and simulation results at 300K deviates from experimental values by 0.6%, 0.5%, 1.3% and 0.9%, respectively. Simulated lattice distances are slightly longer than their experimental values.

Table 7.14: The lattice distance in $\AA$ for the Ag-Pb binary alloy at temperatures ranging from 300K to 1500K .

T(K)	Ag	Pb2Ag8	Pb4Ag6	Pb6Ag4	Pb8Ag2	Pb
300	4.1164	4.3263	4.5188	4.7012	4.8639	5.0150
400	4.1277	4.3404	4.5370	4.7256	4.8883	5.0407
500	4.1393	4.3552	4.5610	4.7539	4.9157	5.0692
600	4.1514	4.3712	4.5928	4.8078	4.9991	5.1024
700	4.1642	4.3883	4.6380	4.8441	5.0540	5.1462
800	4.1777	4.4083	4.6725	4.8834	5.0914	5.3080
900	4.1927	4.4796	4.7030	4.9164	5.1312	5.3489
1000	4.2078	4.5202	4.7337	4.9522	5.1724	5.3934
1100	4.2251	4.5477	4.7653	4.9890	5.2128	5.4497
1200	4.2444	4.5721	4.7945	5.0213	5.2543	5.4887
1300	4.2667	4.6047	4.8281	5.0573	5.2962	5.5457
1400	4.4098	4.6291	4.8562	5.0993	5.3429	5.5988
1500	4.4345	4.6605	4.8907	5.1359	5.3904	5.6620

Table 7.15: The lattice distance in $\AA$ for the Ag-Cu binary alloy at temperatures ranging from 300K to 1500K .

T(K)	Ag	Cu2Ag8	Cu4Ag6	Cu6Ag4	Cu8Ag2	Cu
300	4.1165	4.0408	3.9563	3.8622	3.7592	3.6441
400	4.1277	4.0519	3.9674	3.8731	3.7698	3.6543
500	4.1393	4.0636	3.9791	3.8846	3.7810	3.6651
600	4.1514	4.0759	3.9914	3.8968	3.7927	3.6764
700	4.1642	4.0888	4.0045	3.9098	3.8055	3.6884
800	4.1777	4.1027	4.0188	3.9307	3.8193	3.7012
900	4.1923	4.1178	4.0446	3.9747	3.8346	3.7153
1000	4.2078	4.1343	4.1070	4.0040	3.8984	3.7307
1100	4.2251	4.1539	4.1276	4.0247	3.9219	3.7740
1200	4.2444	4.2525	4.1506	4.0441	3.9409	3.8358
1300	4.2668	4.2790	4.1723	4.0659	3.9587	3.8532
1400	4.4098	4.3018	4.1925	4.0850	3.9772	3.8712
1500	4.4345	4.3246	4.2147	4.1049	3.9979	3.8887

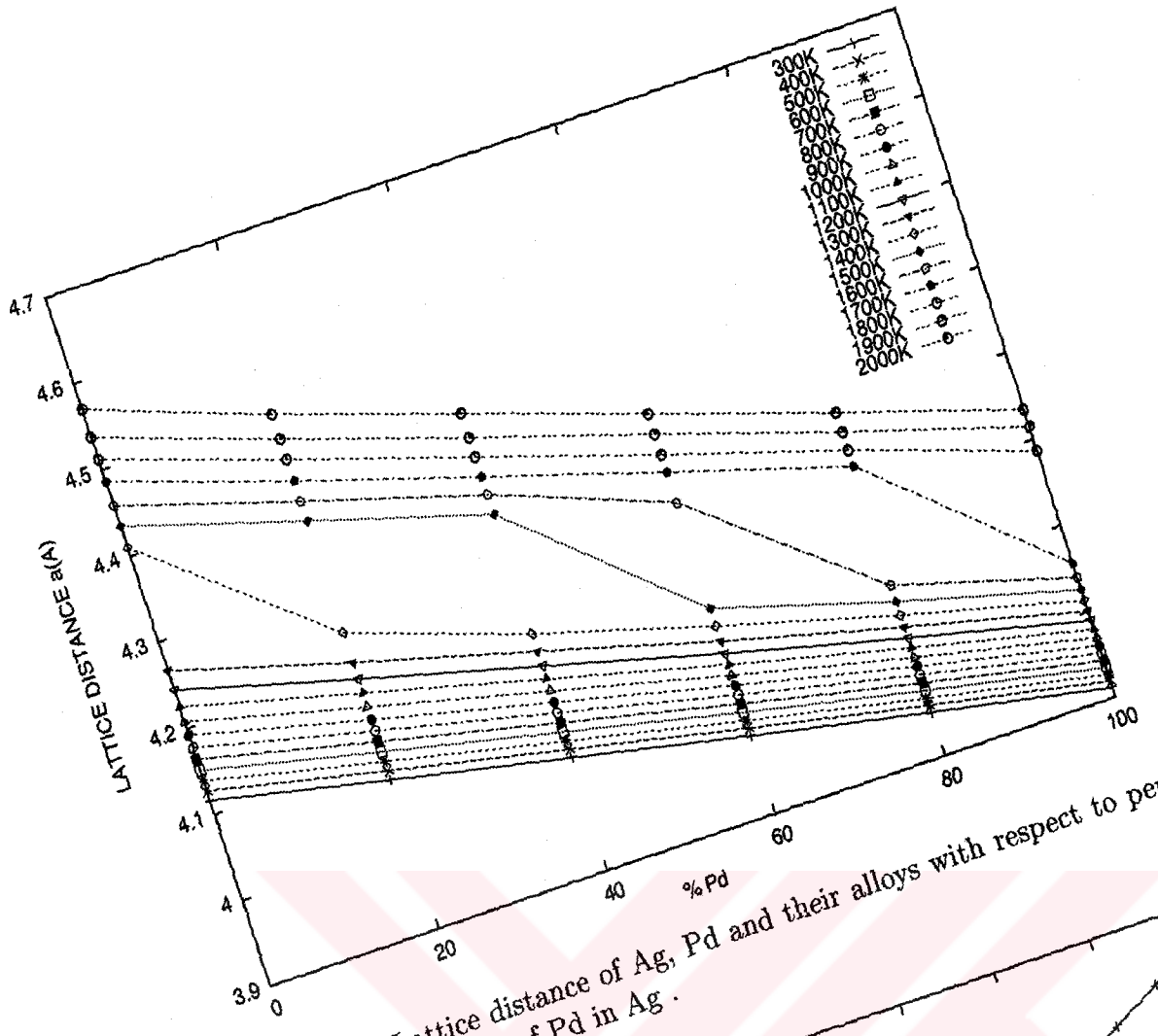

Figure 7.29: Lattice distance of Ag, Pd and their alloys with respect to percentage concentration of Pd in Ag .

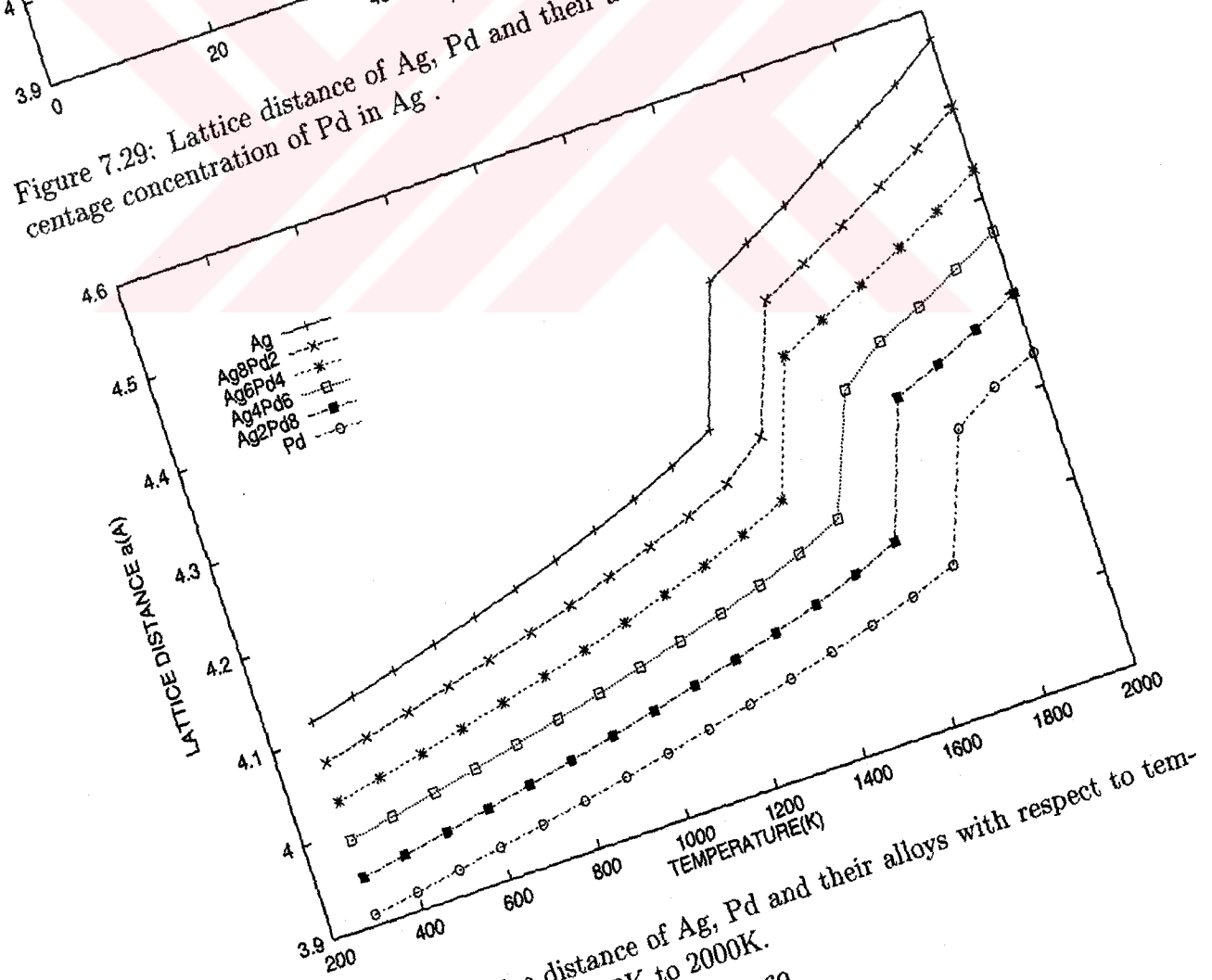

Figure 7.30: Lattice distance of Ag, Pd and their alloys with respect to temperatures ranging from 300K to 2000K.

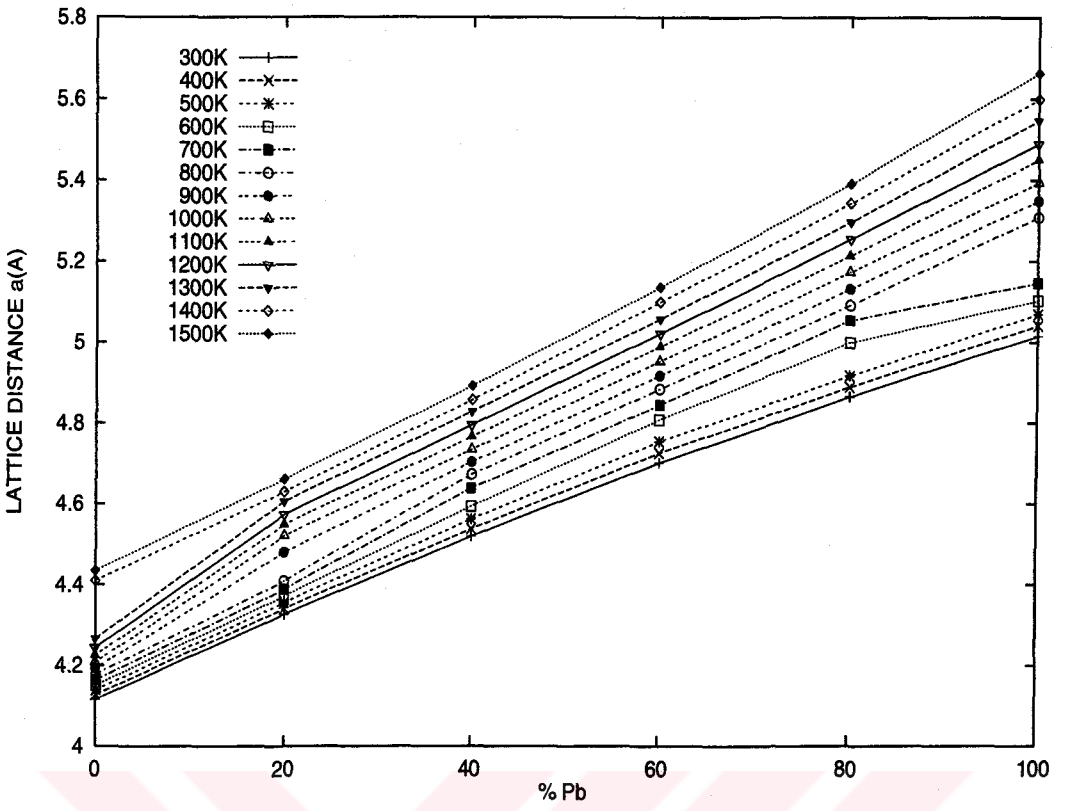

Figure 7.31: Lattice distance of Ag, Pb and their alloys with respect to percentage concentration of Pb in Ag .

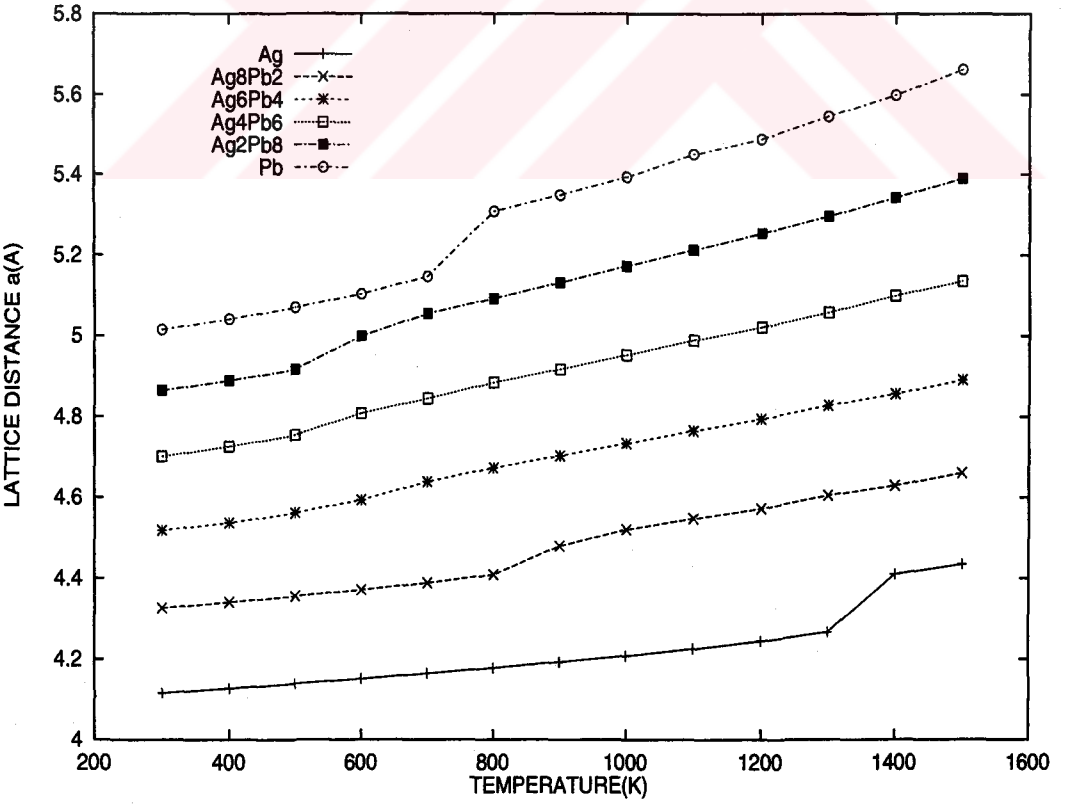

Figure 7.32: Lattice distance of Ag, Pb and their alloys with respect to temperatures ranging from 300K to 1500K.

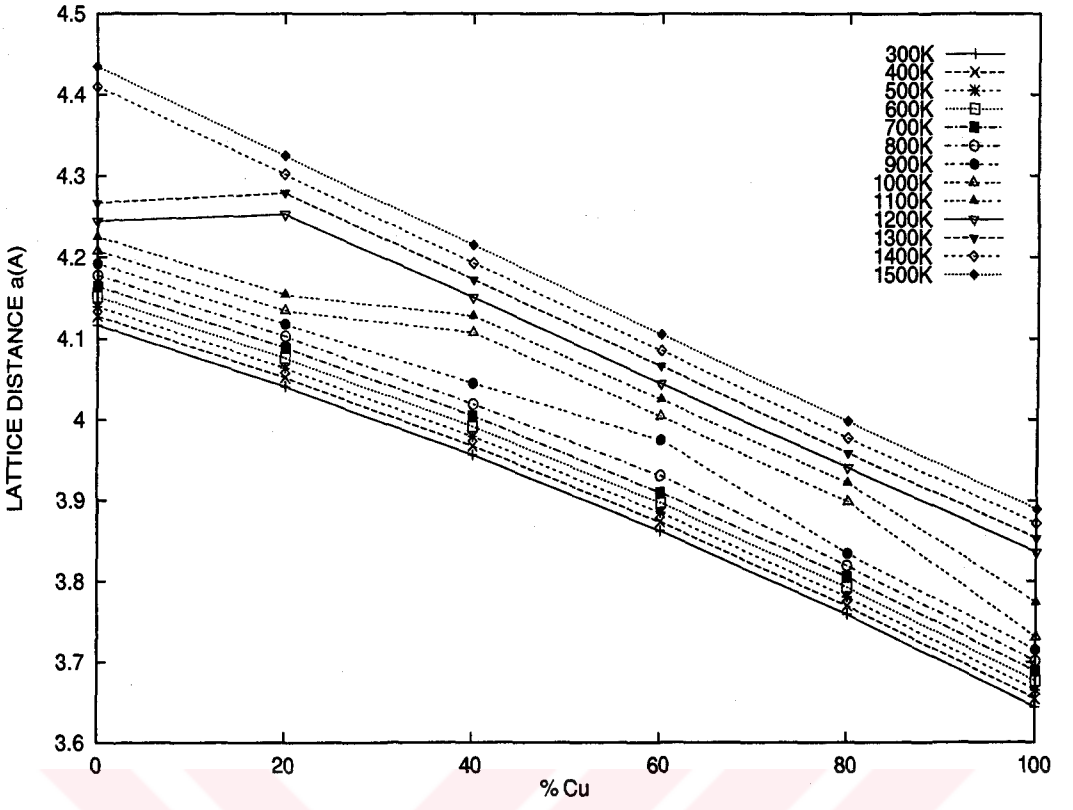

Figure 7.33: Lattice distance of Ag, Cu and their alloys with respect to percentage concentration of Cu in Ag .

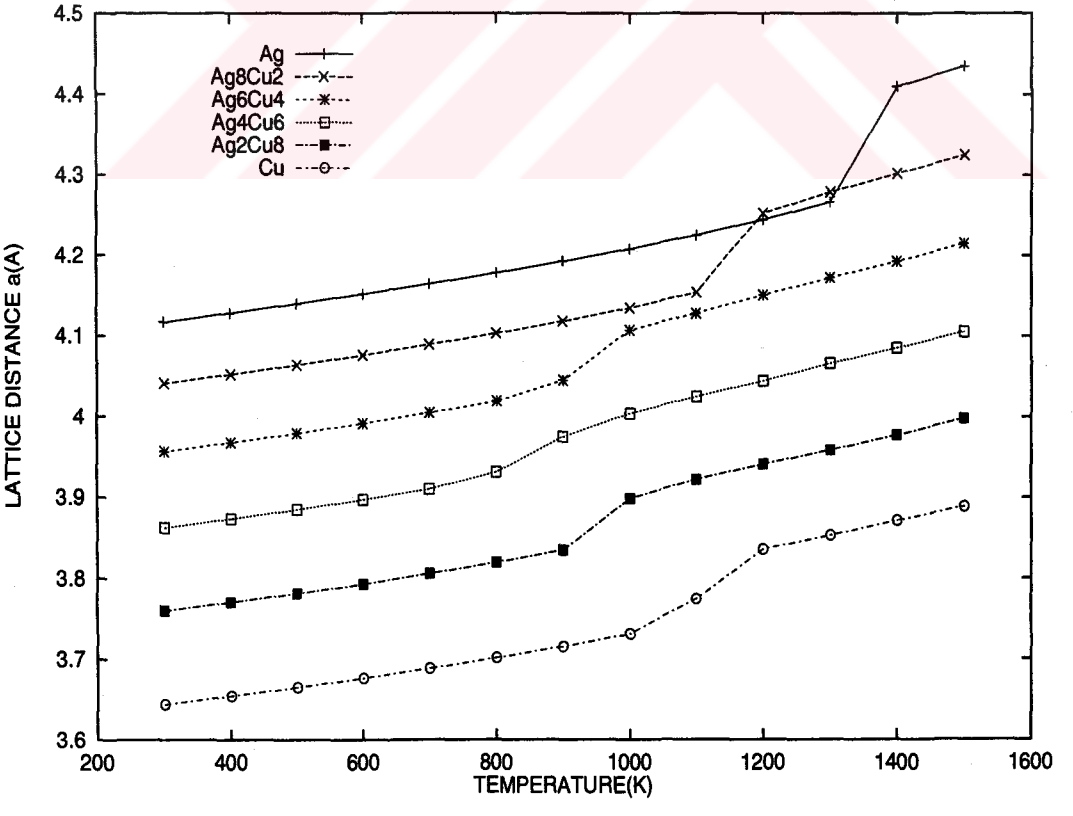

Figure 7.34: Lattice distance of Ag, Cu and their alloys with respect to temperatures ranging from 300K to 1500K.

In Tables 7.16 and 7.17 we list the available experimental density and enthalpy values found for pure metals. Next we present the comparison of our simulated values for pure metals with experiment. Our density values are consistently lower than the corresponding experimental results. We have calculated the deviation from the experimental values. In solid forms of Ag, Pb, and Cu our simulated values show approximately 2.2%, 4.9% and 4.9% deviation, respectively, from the experimental values. In liquid forms of these pure metals deviations are even bigger.

In Figures 7.35, 7.36, 7.37 and 7.38 we show the simulated and experimental enthalpy values for pure metals Ag, Pd, Pb and Cu. Enthalpy values are evaluated taking 300K values as reference. Simulated enthalpy values are in good agreement with experimental values in solid form. However as the metal melts simulated values show different behaviour from the experimental values because enthalpy of melting values differ. In liquid form again a reasonable agreement is observed.

Simulation results for enthalpy show approximately 4.1% and 5.4% deviation from the experimental enthalpy values of solid and liquid Ag, 2.3% and 1.3% deviation from the experimental values of solid and liquid Pd, 3.5% and 10.0% deviation from the experimental enthalpy values of solid and liquid Pb and 5.4% and 17.3% deviation from the experimental enthalpy value of solid and liquid Cu.In the simulations, Cu melts exactly at 1100K. Therefore the values at this temperature are between solid and liquid ones. Since the values should step down at this temperature, a dashed line is used to show the change in the properties when Cu melts.

Table 7.16: Experimental density values of Ag, Pb and Cu in (g/cm^3).[40]

T(K)	300	1233.5	1273	1365	1468	1573
Ag	10.5	9.30	9.26	9.20	9.10	9.00

T(K)	373	473	573	593	673	773	873	973	1073
Pb	11.35	11.15	11	10.7	10.6	10.45	10.35	10.25	10.15

T(K)	973	1073	1173	1273	1353	1373	1473	1573	1673
Cu	8.60	8.55	8.48	8.40	8.35	7.92	7.85	7.76	7.70

Table 7.17: Simulated and Experimental (in parenthesis) enthalpy values with respect to the enthalpy at 300K of Ag, Pb, Pd and Cu in (kj/mol).[38]

T(K)	Ag	Pd	Pb	Cu
300	0	0	0	0
400	2.72 (2.557)	2.64 (2.637)	2.80 (2.730)	2.60 (2.493)
500	5.39 (5.162)	5.26 (5.334)	5.71 (5.543)	5.29 (5.055)
600	8.13 (7.826)	7.93 (8.084)	8.85 (8.440)	8.04 (7.675)
700	10.93 (10.553)	10.62 (10.888)	12.50 (16.259)	10.87 (10.349)
800	13.78 (13.346)	13.38 (13.745)	21.46 (19.277)	13.79 (13.075)
900	16.77 (16.209)	16.17 (16.655)	24.46 (22.262)	16.86 (15.850)
1000	19.82 (19.153)	19.02 (19.619)	27.75 (25.217)	20.08 (18.685)
1100	23.06 (22.178)	21.95 (22.936)	31.02 (28.141)	26.69 (21.590)
1200	26.50 (25.285)	24.94 (25.706)	34.07 (31.033)	35.28 (24.585)
1300	30.24 (39.873)	28.02 (28.830)	37.07 (33.905)	38.29 (27.712)
1400	45.85 (43.220)	31.26 (32.007)	40.18 (36.768)	41.41 (44.130)
1500	49.21 (46.567)	34.56 (35.240)	43.47 (39.632)	44.43 (47.415)
1600	52.46 (49.914)	38.10 (38.541)		
1700	56.11 (53.261)	41.96 (41.924)		
1800	59.44 (56.518)	60.68 (45.401)		
1900	62.74 (59.956)	65.44 (66.450)		
2000	67.02 (63.303)	69.16 (69.923)		

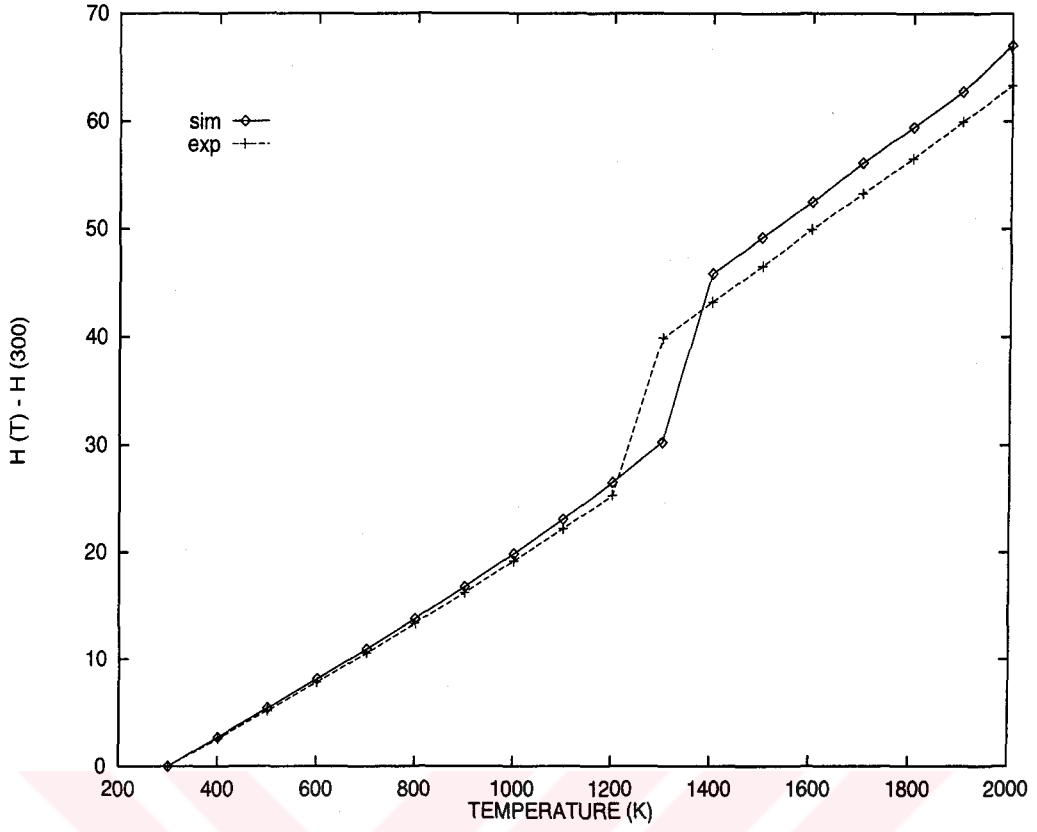

Figure 7.35: Simulated and experimental enthalpy values of Ag in kj/mol.

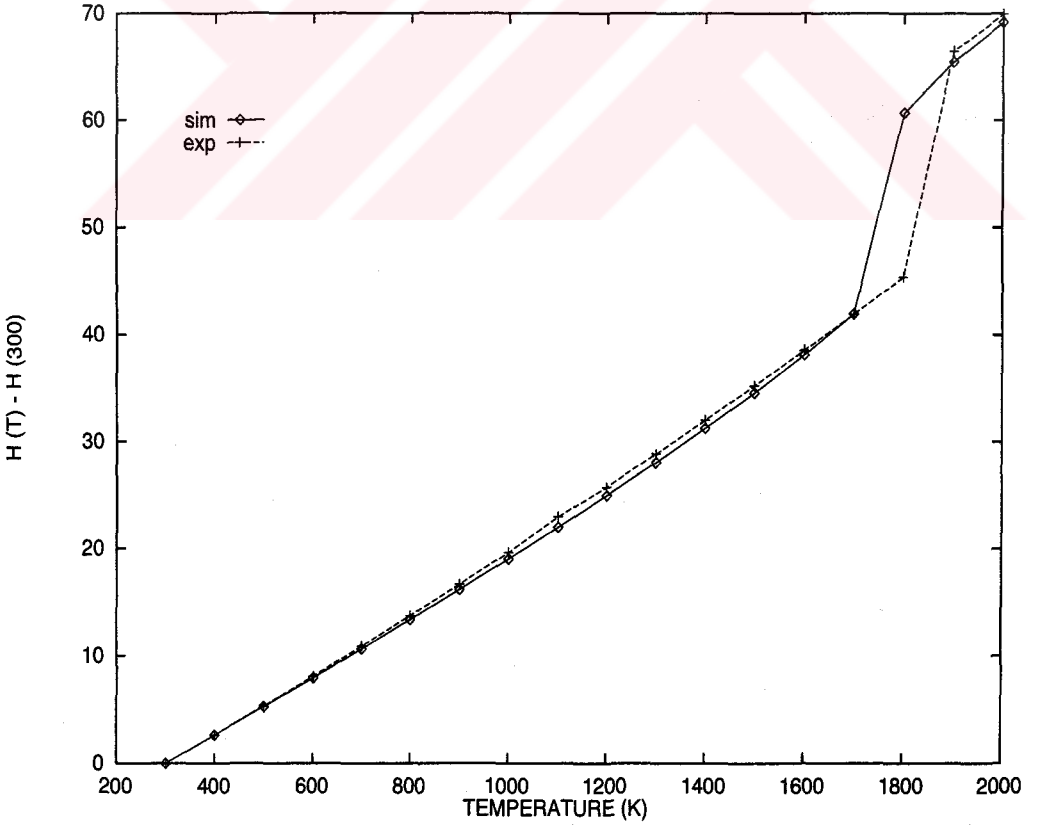

Figure 7.36: Simulated and experimental enthalpy values of Pd in kj/mol.

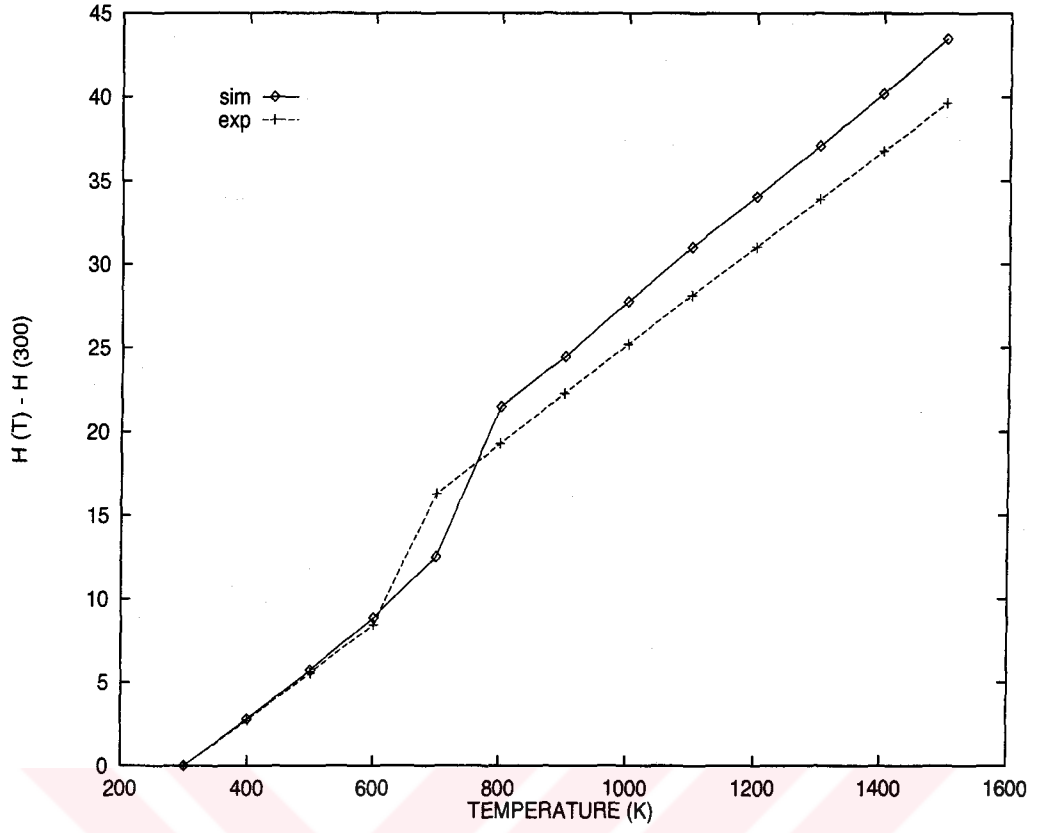

Figure 7.37: Simulated and experimental enthalpy values of Pb in kj/mol.

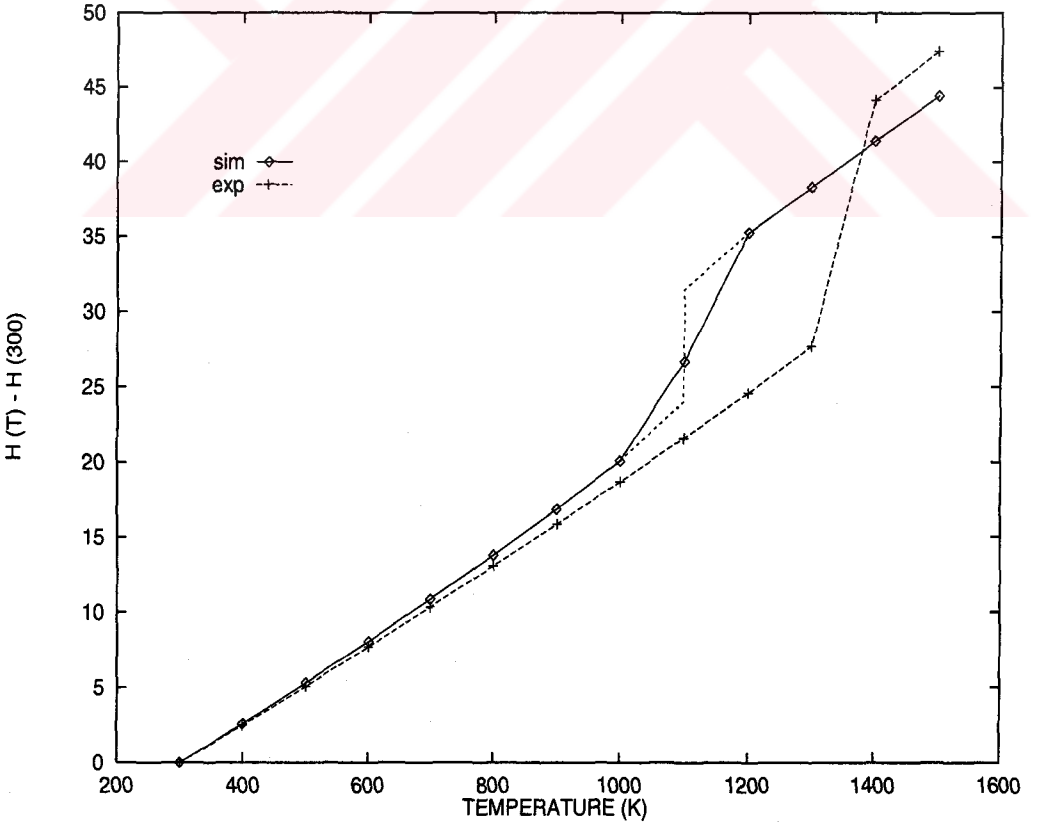

Figure 7.38: Simulated and experimental enthalpy values of Cu in kj/mol.

Next, we have computed the mixing enthalpy ΔH_{mix} of these alloys at each concentration using

$$\Delta H_{mix} = H_{AB} - X_A H^A - X_B H^B \tag{7.1}$$

where X_A and X_B are concentrations of the metals A and B, respectively, with $X_A + X_B = 1$. In Table 7.18 simulated mixing enthalpy values are given for the solid and liquid forms of these alloys. In Figures 7.39, 7.41, 7.43, 7.45, 7.47 and 7.49 we have plotted simulation results of the enthalpy of mixing for Ag-Pd, Ag-Pb and Ag-Cu in solid and liquid forms. Corresponding experimental enthalpy of mixing for these alloys in solid and liquid forms are given in Figures 7.40, 7.42, 7.44, 7.46), 7.48 and 7.50.

For solid Ag-Pd, simulated ΔH^S_{mix} values are positive (with max. at 2 kj/mol). On the other hand the experimental values of enthalpy of mixing for solid Ag-Pd is negative (with min. at 6 kj/mol). Values are taken from Hultgren *et al* [39]. For the same alloy in liquid form simulated ΔH^L_{mix} is positive again (with max. at 1 kj/mol). The experimental values for liquid form of this alloy is taken from Karakaya *et al* [37]. Experimental enthalpy of mixing of liquid Ag-Pd is negative (with min. at 2.5 kj/mol) up to $X_{0.67}$ then it is positive (with max. value at 0.8 kj/mol).

For solid Ag-Pb simulated ΔH^S_{mix} values are positive (with max. at 7 kj/mol). They are in very good agreement with the experimental values [37] (with max. at 7 kj/mol). For the same alloy in liquid form simulated ΔH^L_{mix} values are positive (with max. at 1.3 kj/mol). Also the experimental enthalpy of mixing is positive [37] (with max. at 3.3 kj/mol).

Table 7.18: The simulated solid and liquid enthalpy of mixing values of Ag-Pd, Ag-Pb and Ag-Cu alloys in kj/mol.

T(K)	Ag	Pd2Ag8	Pd4Ag6	Pd6Ag4	Pd8Ag2	Pd
300	0	0.9700	1.9608	1.9807	1.3249	0
400	0	1.2906	1.9598	1.9885	1.3205	0
500	0	1.2807	1.9496	1.9875	1.3230	0
600	0	1.2782	1.9666	1.9831	1.3171	0
700	0	1.2849	1.9605	1.9720	1.3174	0
800	0	1.3060	1.9644	1.9784	1.3224	0
900	0	1.2436	1.9547	1.9836	1.3270	0
1000	0	1.3261	1.9776	1.9862	1.3170	0
1700	0	0.63926	1.18162	1.52978	1.36444	0
1800	0	0.91342	1.48164	1.56006	1.50658	0
1900	0	0.63046	0.91772	1.03498	0.66494	0
2000	0	0.61758	1.19646	1.23664	0.66732	0

T(K)	Ag	Pb2Ag8	Pb4Ag6	Pb6Ag4	Pb8Ag2	Pb
300	0	5.1135	6.5249	5.9692	3.8522	0
400	0	5.1188	6.5637	5.9005	4.0281	0
500	0	5.1145	6.5949	6.1592	3.9431	0
600	0	5.1221	7.1454	6.0487	4.1214	0
700	0	5.0690	6.8363	5.7392	3.6420	0
800	0	5.4082	7.1032	6.0688	4.0344	0
900	0	5.1518	7.1139	6.0759	4.0380	0
1000	0	0.6766	1.1411	1.3646	0.8434	0
1100	0	0.7575	1.2457	1.2475	0.6752	0
1200	0	0.5956	1.1862	1.2393	0.7987	0
1300	0	0.5849	1.0633	1.0372	0.7378	0
1400	0	0.4783	0.9333	1.2066	0.8006	0
1500	0	0.7366	1.1019	1.1652	0.7650	0

T(K)	Ag	Cu2Ag8	Cu4Ag6	Cu6Ag4	Cu8Ag2	Cu
300	0	1.2262	1.6376	1.4624	1.0648	0
400	0	1.1418	1.5800	1.4276	1.0538	0
500	0	1.1445	1.5936	1.4412	1.0662	0
600	0	1.3925	1.6216	1.4860	1.0816	0
700	0	1.1529	1.6396	1.5333	1.1267	0
800	0	1.1883	1.7315	1.3302	1.1996	0
900	0	1.2136	1.4269	0.7954	1.1640	0
1000	0	-1.6000	-2.5681	-2.7782	-2.4366	0
1100	0	-1.6000	-2.6396	-2.8859	-2.0733	0
1200	0	-1.5405	-2.2958	-2.7063	-1.8154	0
1300	0	-1.4924	-2.4831	-2.5650	-1.9269	0
1400	0	-1.5247	-2.4744	-2.5944	-1.9297	0
1500	0	-1.4429	-2.2832	-2.5237	-1.5791	0

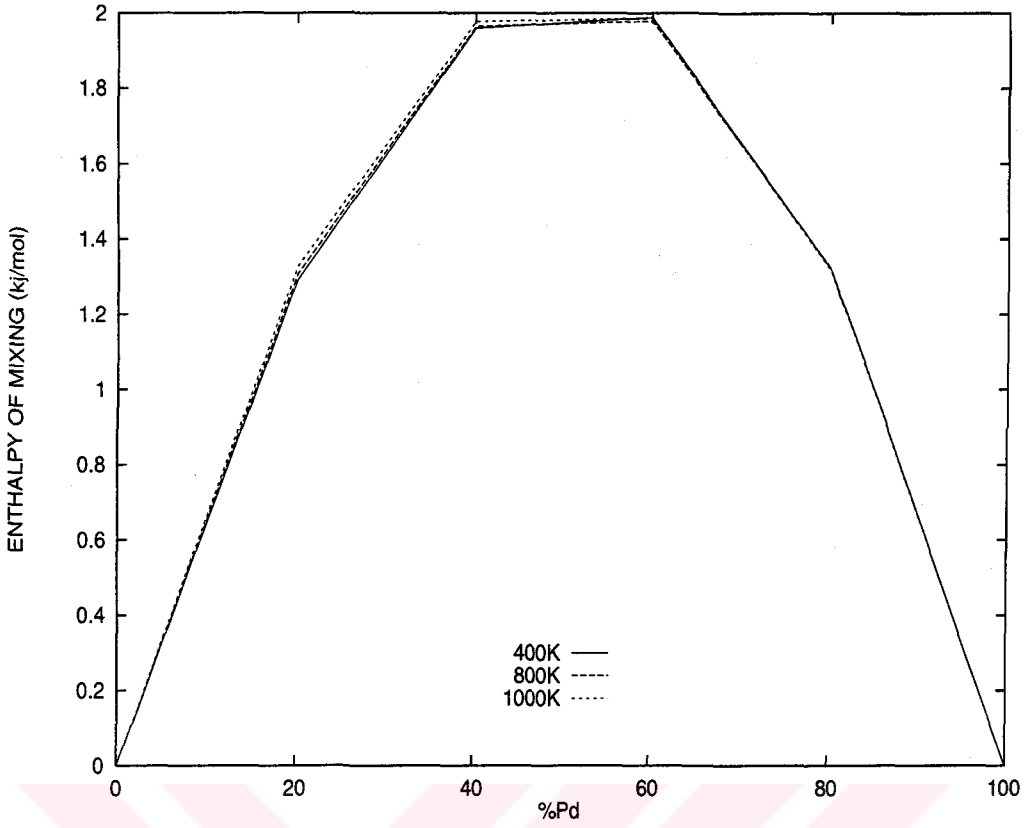

Figure 7.39: Simulated enthalpy of mixing in (kj/mol) for Ag-Pd alloy with respect to percentage concentration of Pd in Ag at solid phase.

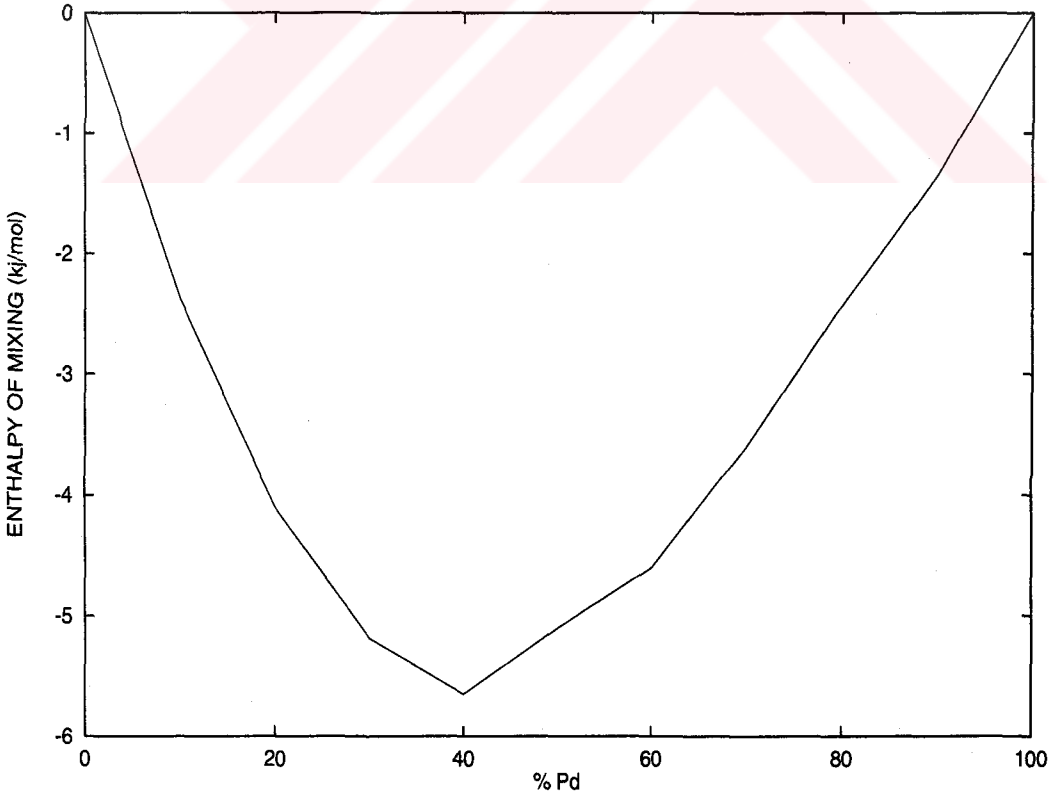

Figure 7.40: Experimental enthalpy of mixing of solid Ag-Pd at 1000K in (kj/mol).[39]

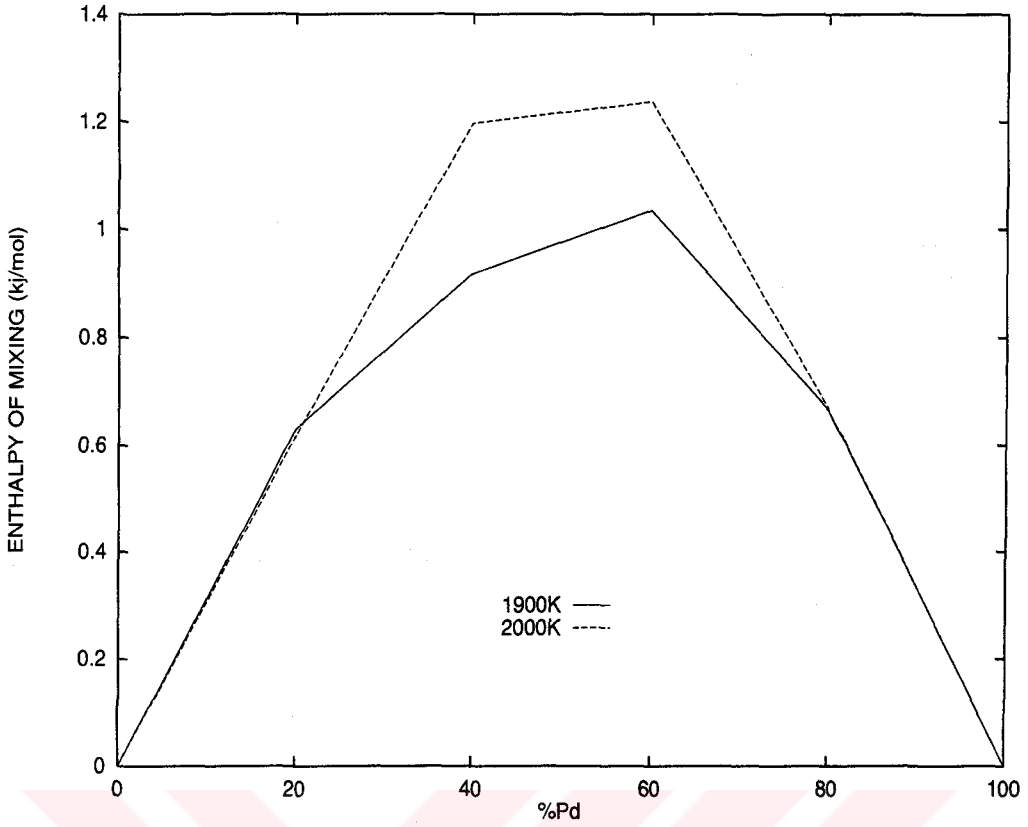

Figure 7.41: Simulated enthalpy of mixing in (kj/mol) for Ag-Pd alloy with respect to percentage concentration of Pd in Ag at liquid phase.

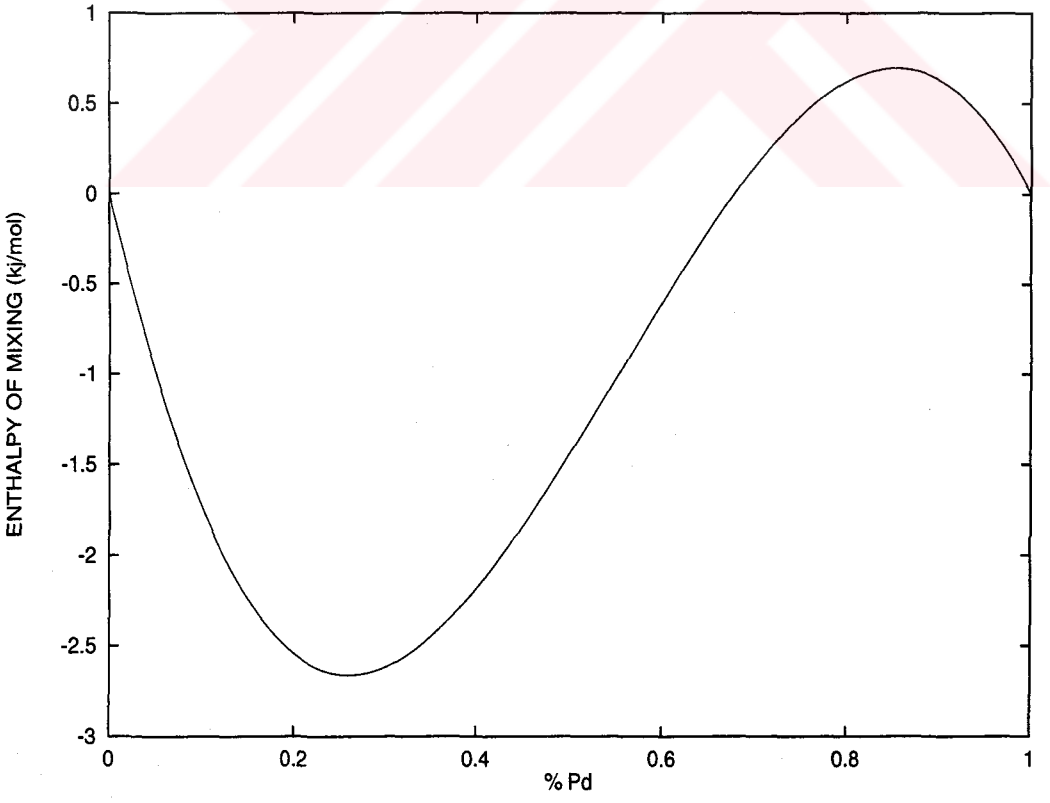

Figure 7.42: Experimental enthalpy of mixing of liquid Ag-Pd in (kj/mol).[37]

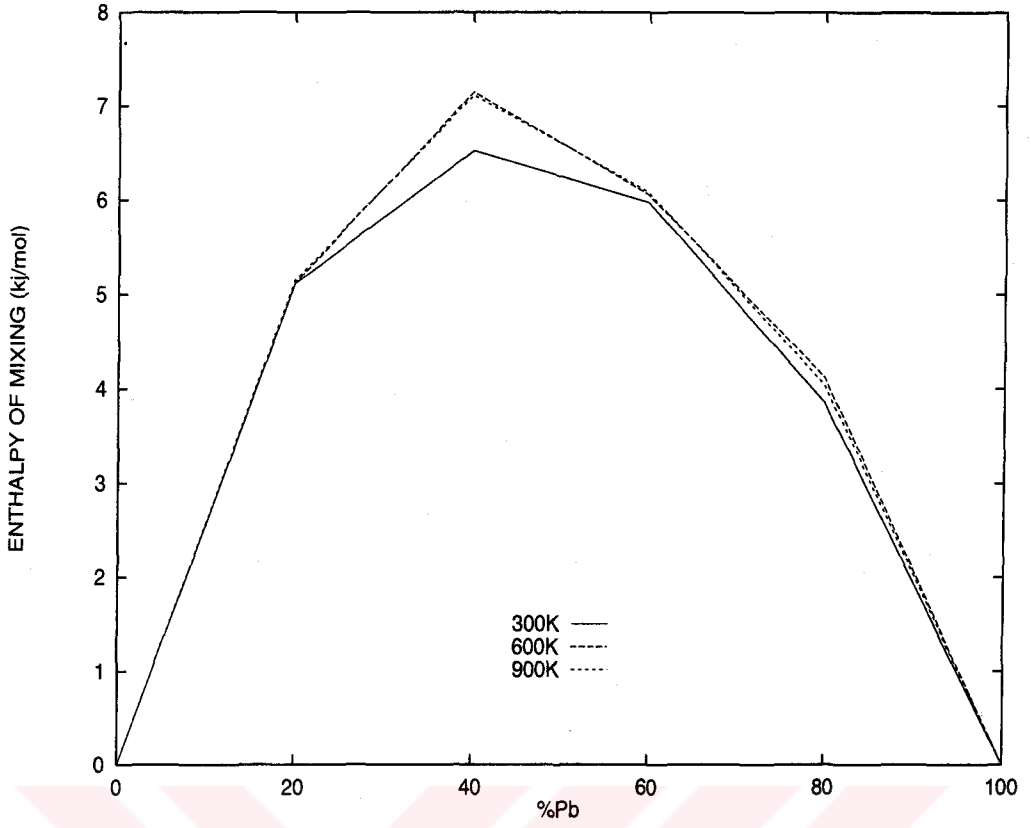

Figure 7.43: Simulated enthalpy of mixing in (kj/mol) for Ag-Pb alloy with respect to percentage concentration of Pb in Ag at solid phase.

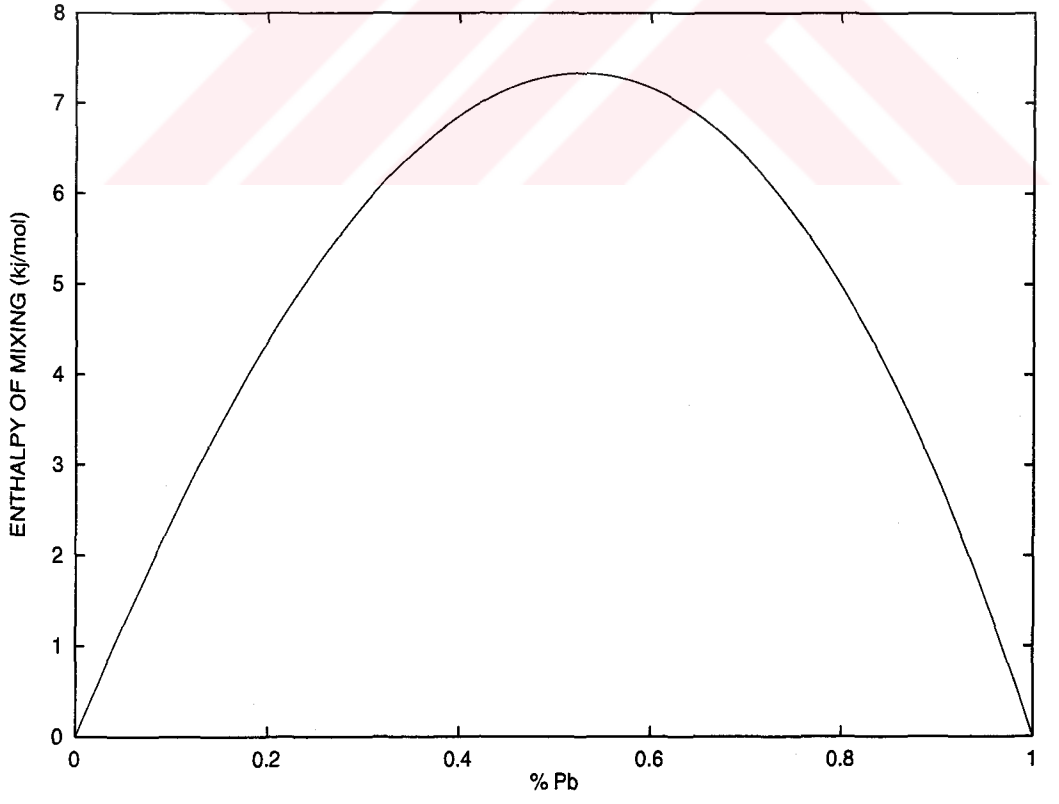

Figure 7.44: Experimental enthalpy of mixing of solid Ag-Pb in (kj/mol).[37]

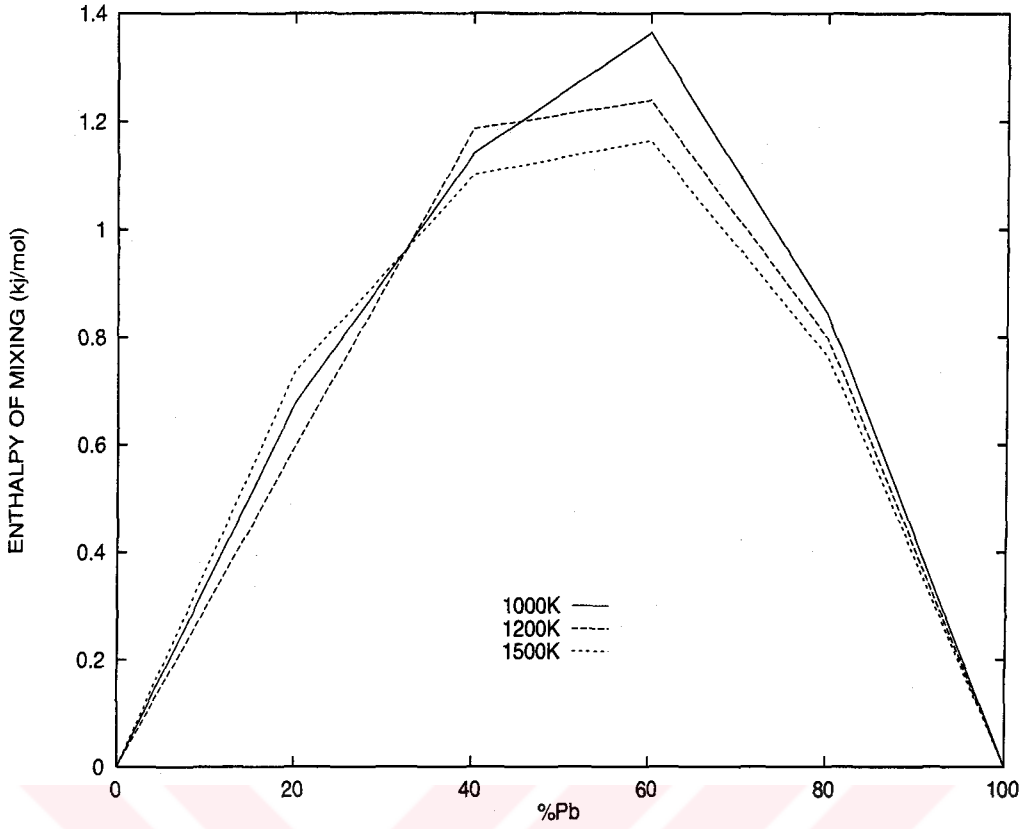

Figure 7.45: Simulated enthalpy of mixing in (kj/mol) for Ag-Pb alloy with respect to percentage concentration of Pb in Ag at liquid phase.

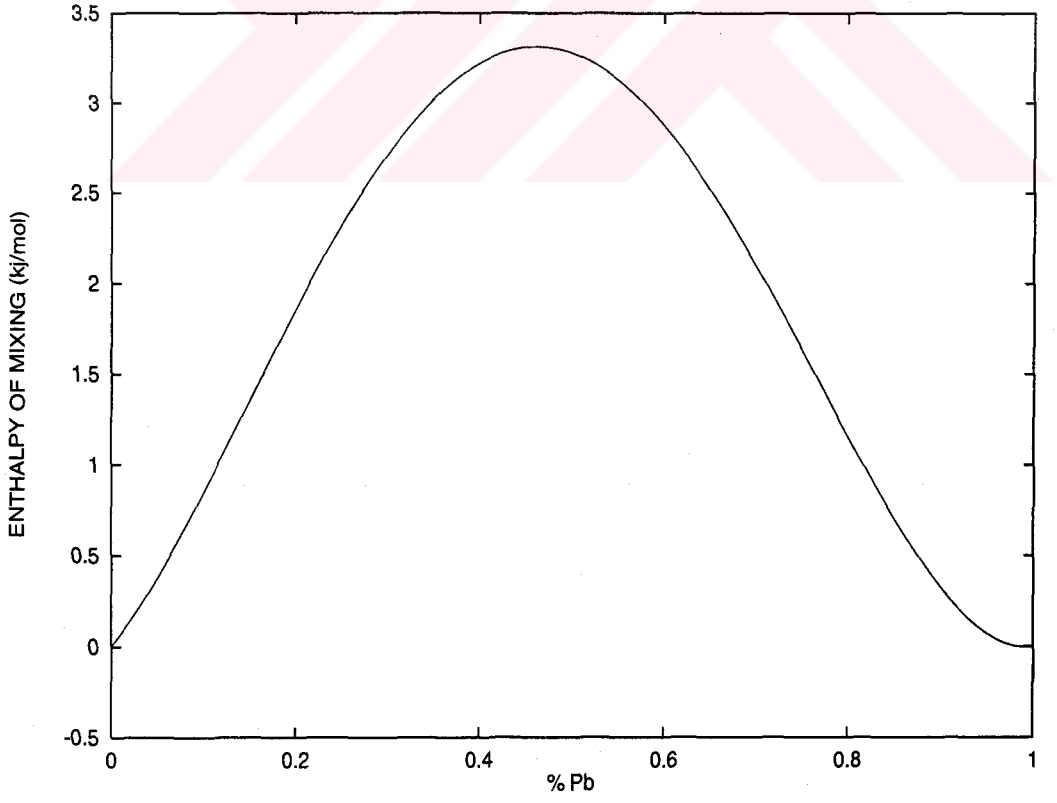

Figure 7.46: Experimental enthalpy of mixing of liquid Ag-Pb in (kj/mol).[37]

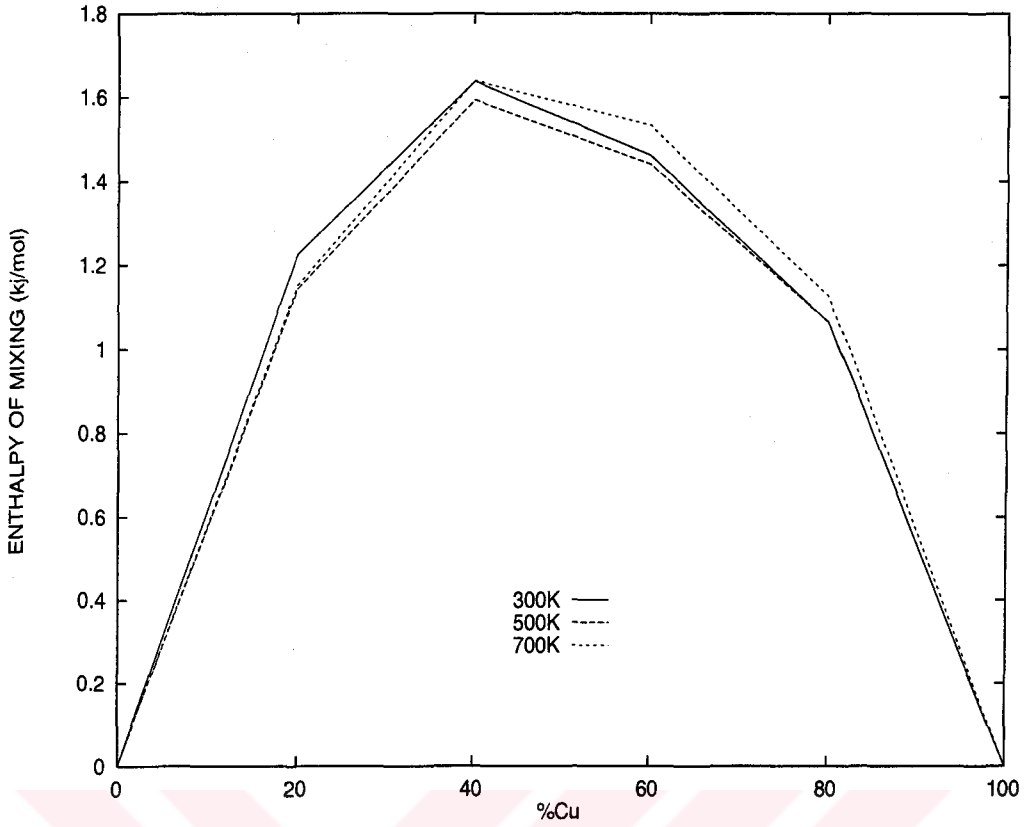

Figure 7.47: Simulated enthalpy of mixing in (kj/mol) for Ag-Cu alloy with respect to percentage concentration of Cu in Ag at solid phase.

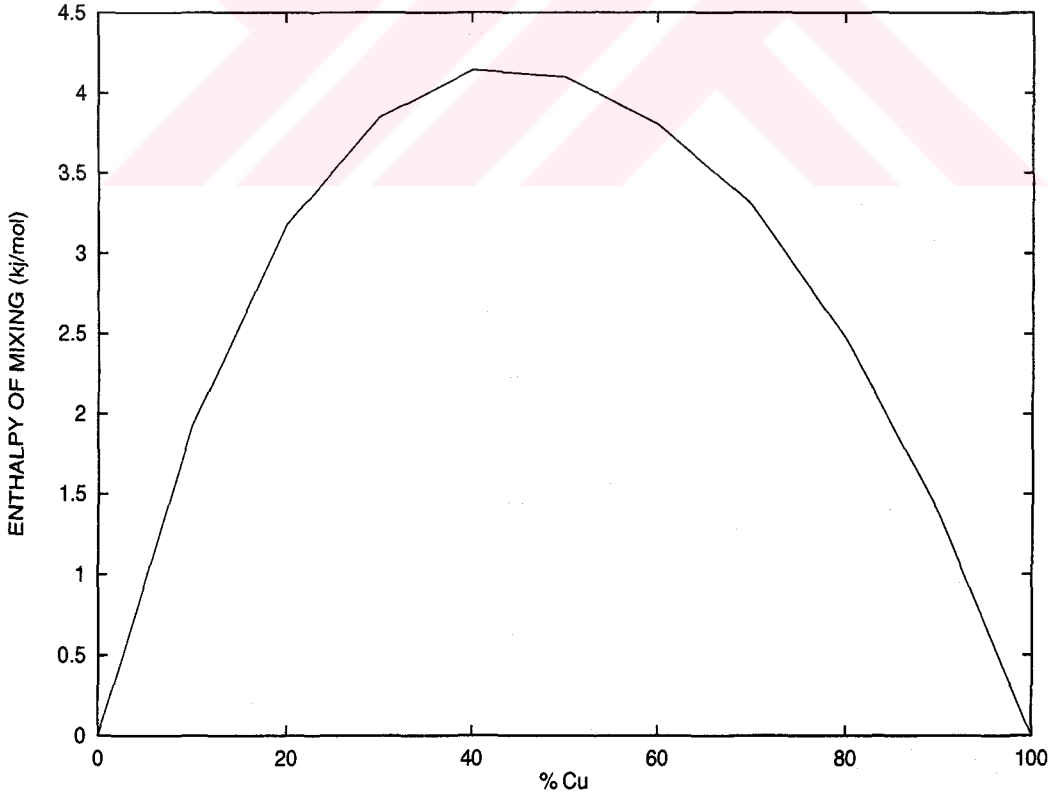

Figure 7.48: Experimental enthalpy of mixing of solid Ag-Cu in (kj/mol).[37]

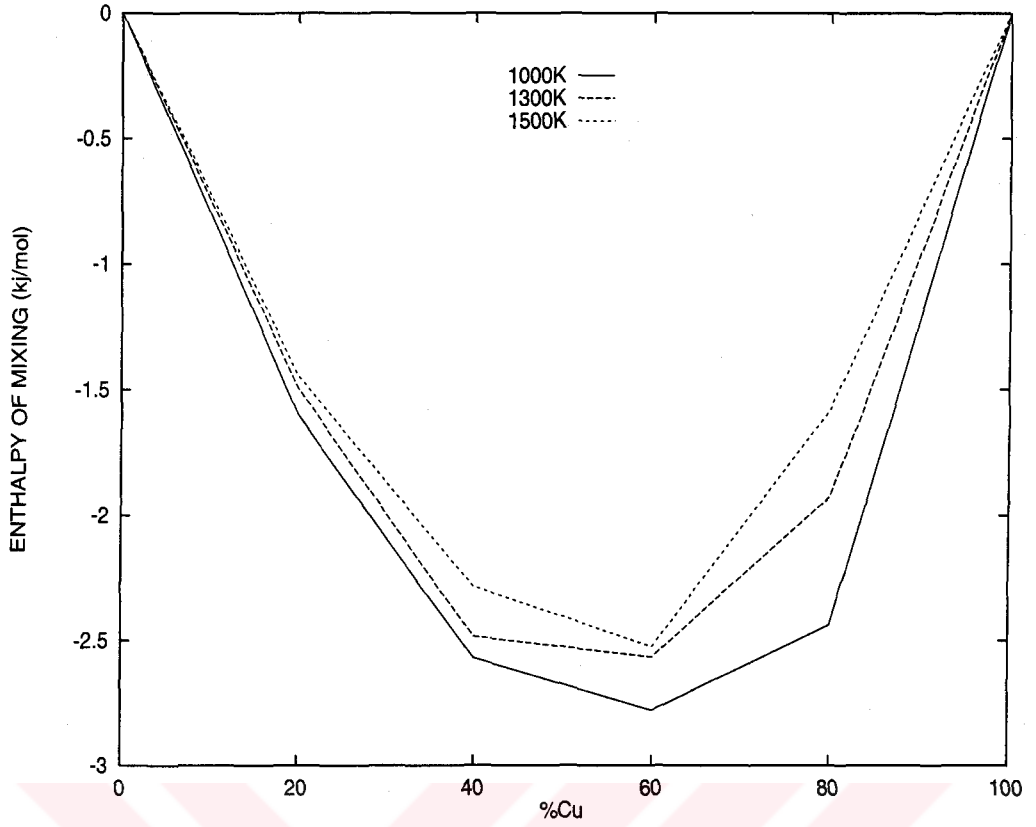

Figure 7.49: Simulated enthalpy of mixing in (kj/mol) for Ag-Cu alloy with respect to percentage concentration of Cu in Ag at liquid phase.

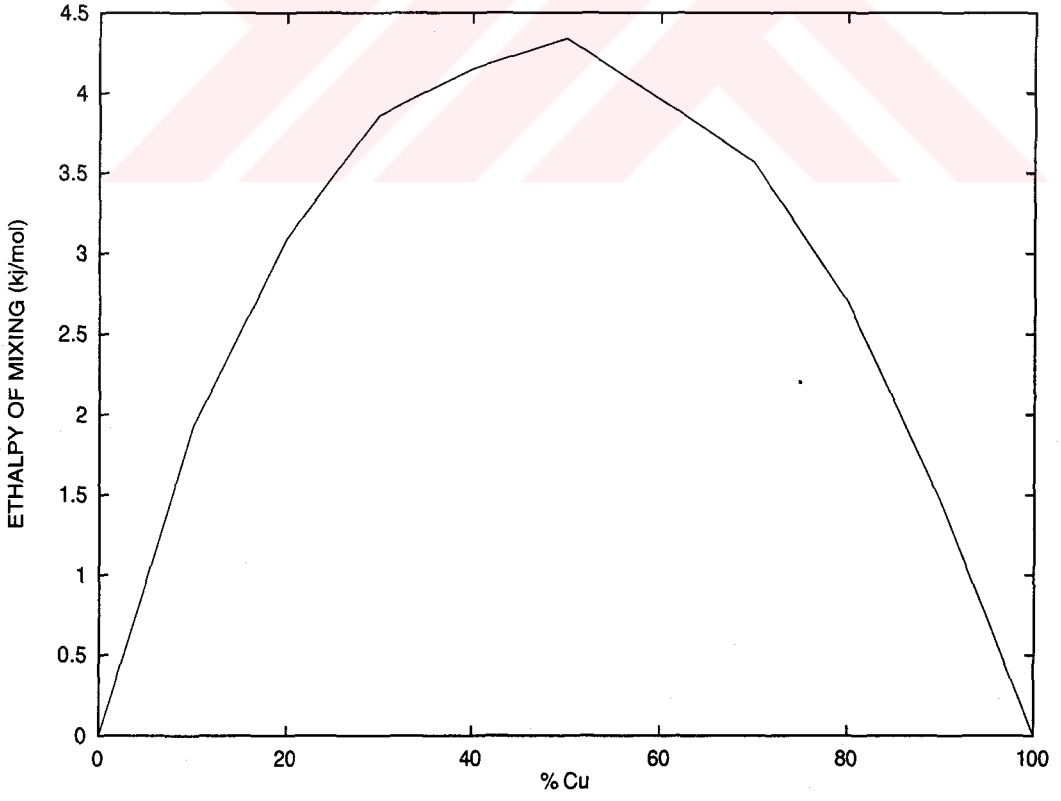

Figure 7.50: Experimental enthalpy of mixing of liquid Ag-Cu at 1400K in (kj/mol).[39]

For solid Ag-Cu simulated ΔH^S_{mix} are positive (with max. at 1.6 kj/mol) and so are the experimental values [24] (with max. at 4 kj/mol). For the same alloy in liquid form ΔH^L_{mix} is negative (with min. at 2.5 kj/mol). The experimental values for this liquid alloy at 1400K give the enthalpy of mixing positive (with max. at 4.3 kj/mol) [39].

Enthalpy of mixing values being negative or positive implies that heat is gained or lost by the system while forming the alloy. It gives information only if mixing is enthalpically favorable. But in order to understand if the alloy is mixed or not we should look at Gibbs free energies of mixing of the alloys.

7.2.2 Gibbs Free Energies and Phase Diagrams

The alloys can form different type of mixing depending on their Gibbs free energies. In order to find the phase form of Ag-Pd, Ag-Pb and Ag-Cu we have found Gibbs free energy of mixing $\Delta G_{mix} = \Delta H_{mix} - T\Delta S_{mix}$ using the simulated enthalpy of mixing values and entropy of random mixing.

Simulated enthalpy of mixing values of Table 7.18 are averaged to get analytic forms depending on the concentration X for solid and liquid phases.

The enthalpy of mixing formulas for solid and liquid Ag-Pd:

$$\Delta H^S_{mix} = 8140 X_{Ag} X_{Pd} \tag{7.2}$$

$$\Delta H^L_{mix} = 4299 X_{Ag} X_{Pd} \tag{7.3}$$

The enthalpy of mixing formulas for solid and liquid Ag-Pb:

$$\Delta H^S_{mix} = (33500 - 12036_{Pb}) X_{Ag} X_{Pb} \tag{7.4}$$

$$\Delta H^L_{mix} = (4595 + 630X_{Pb})X_{Ag}X_{Pb} \tag{7.5}$$

The enthalpy of mixing formulas for solid and liquid Ag-Cu:

$$\Delta H^S_{mix} = (7715 - 1578X_{Cu})X_{Ag}X_{Cu} \tag{7.6}$$

$$\Delta H^L_{mix} = (-8658 - 3354X_{Cu})X_{Ag}X_{Cu} \tag{7.7}$$

The simulation mixes the atoms randomly so the entropy of mixing is

$$\Delta S_{mix} = -R(X \ln X + (1 - X) \ln(1 - X)) \tag{7.8}$$

where X is concentration.

The Gibbs free energy of melting of the metals Ag, Pd, Pb and Cu are experimentally calculated [41]:

$$\Delta G^{Ag}_{melt} = 1218.86 + 90.7247T + 0.4799\ 10^{-2}T^2 \tag{7.9}$$
$$-13.74T \ln T + 266500/T$$

$$\Delta G^{Pd}_{melt} = -21890.5. + 230.357T + 0.7598\ 10^{-2}T^2 \tag{7.10}$$
$$-31.208T \ln T + 7121600/T$$

$$\Delta G^{Pb}_{melt} = 4799 - 7.99T \tag{7.11}$$

$$\Delta G^{Cu}_{melt} = 7683 + 38.844T + 1.8933\ 10^{-3}T^2 \tag{7.12}$$
$$-6.527T \ln T$$

Finally, the functional forms of Gibbs free energies of solid and liquid A-B type alloys are:

$$\Delta G^S_{mix}(T, X) = \Delta H^S_{mix}(X) - T\Delta S_{mix}(X) \tag{7.13}$$

$$\Delta G'^{L}_{mix}(T,X) = \Delta H^{L}_{mix}(X) - T\Delta S_{mix}(X) + X\Delta G^{B}_{melt}(T) \qquad (7.14)$$
$$+(1-X)\Delta G^{A}_{melt}(T)$$

where T is temperature in K and the concentration of metal B for the A-B type alloy is $X(= X_B = 1 - X_A)$.

In this section we present the simulation results of Gibbs free energy of mixing and phase diagrams of Ag-Pd, Ag-Pb and Ag-Cu are given. Phase diagrams are obtained using the method of lowest common tangent line of the Gibbs free energies of solid and liquid alloys and the program FACT is used to implement this method [44]. A comparison is made between the phase diagrams drawn from our simulations and the phase diagrams obtained from experimental results [37].

Ag-Pd alloy mixes completely in solid and liquid phases. In Figure 7.51 the alloy at 1200K is completely in solid form since solid Gibbs free energy line of solid Ag-Pd is entirely below that of liquid Ag-Pd. But at 1400K these lines cross each other (Figure 7.52). The alloy is in liquid form up to $X_{Pd} = 0.35$ and it is in solid form after $X_{Pd} = 0.5$. Between these concentration Ag-Pd is in an intermediate phase having solid-liquid phase mixtures. Here Gibbs free energy of the mixture is the lowest common tangent line of these two curves. In Figure 7.53 solid-liquid mixture forms between $X_{Pd} = 0.8$ and $X_{Pd} = 0.9$. Finally, in Figure 7.54 at 1900K it is completely in liquid form since solid Gibbs free energy line of solid Ag-Pd is entirely above that of liquid Ag-Pd.

In Figures 7.55 and 7.56 Gibbs free energies of solid and liquid Ag-Pb are all positive so there is no possibility to form solid or liquid alloy below

the temperature about 525K. They start to mix when liquid phase appears. At 525K liquid curve touches to the zero level at about $X_{Pb} = 0.9$ (Figure 7.57). Above this temperature liquid curve goes down and the alloy start to melt. In Figure 7.58 at 600K, it is a mixture of Ag rich solid and Ag-Pb liquid alloy up to about $X_{Pb} = 0.66$. After that the alloy is completely liquid. At 800K and 1000K it is again a mixture of Ag rich solid and Ag-Pb liquid alloy up to about $X_{Pb} = 0.53$ and $X_{Pb} = 0.3$, respectively and after these concentrations the alloy is in liquid form (Figures 7.59 and 7.60). In Figure 7.61 the intermediate phase is about to disappear at 1200K and in Figure 7.62 the alloy is totally melted at 1400K.

The experimentally obtained phase diagram in Figure 7.70 contains Ag rich solid phase and Pb rich solid phase up to some concentration. In fact between these concentrations the solid is the mixture of these Ag rich and Pb rich solid phases. The Ag rich and Pb rich solid solutions appears in the Ag-Pb phase diagram obtained from simulated values but they are so small that they are left within the thickness of the lines in the phase diagram shown in Figure 7.69. Therefore we can say that the Ag-Pb show complete immiscibility at all concentrations.

Our simulated phase diagram of Ag-Cu in Figure 7.71 is not in complete agreement with the experimentally obtained phase diagram given in Figure 7.72. Because we have obtained that Ag-Cu mixes well in solid form although it does not show complete miscibility in solid state.

In Figure 7.63 Ag-Cu is completely in solid form at 800K since solid curve lies entirely below liquid curve. Having a U-shape curve, the solid Ag-Cu

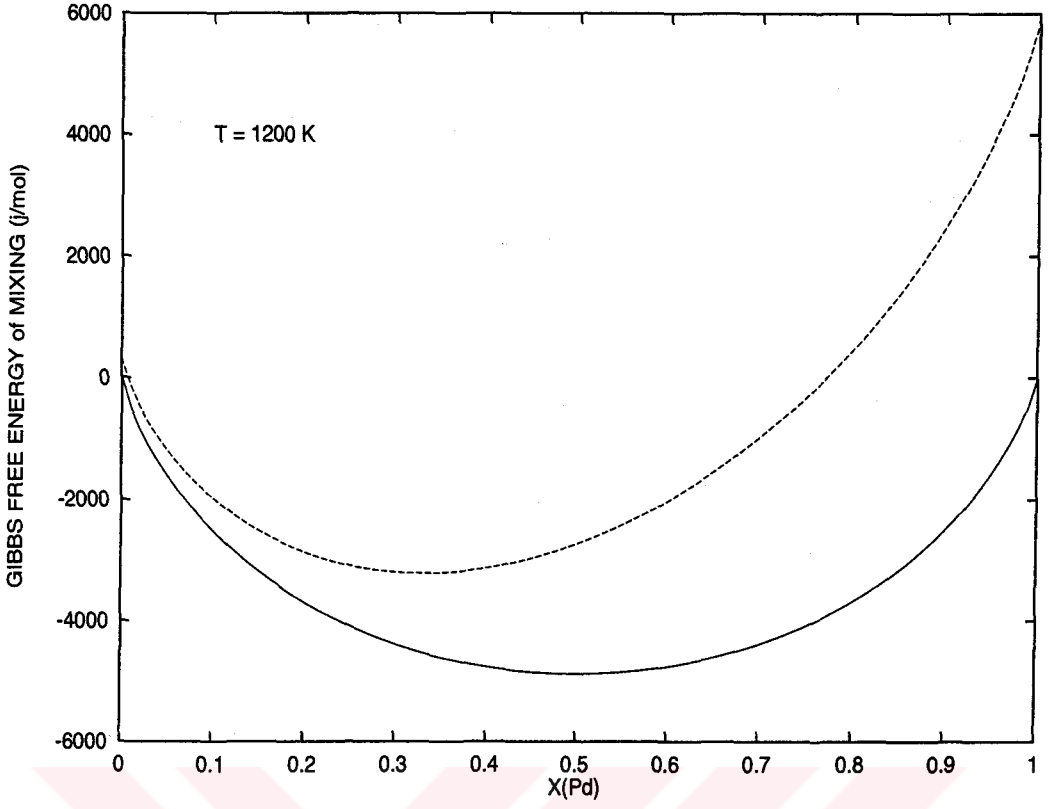

Figure 7.51: Gibbs free energy of mixing of solid (solid line) and liquid (dashed line) Ag-Pd alloy at 1200K in j/mol.

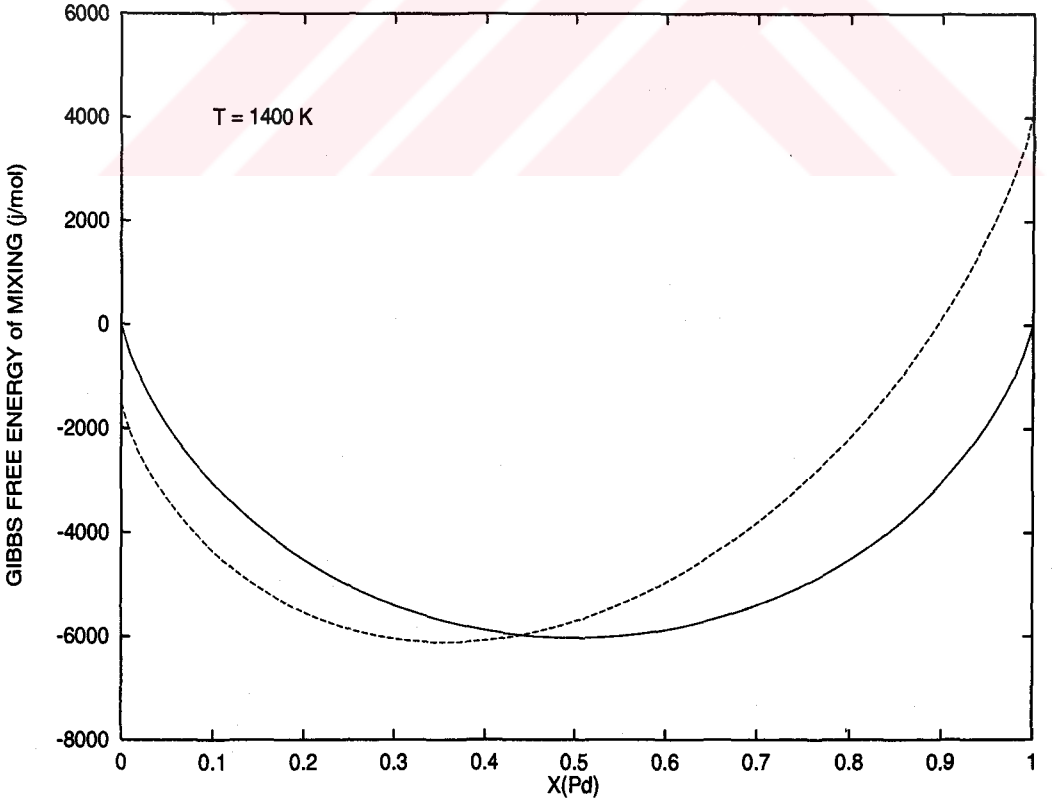

Figure 7.52: Gibbs free energy of mixing of solid (solid line) and liquid (dashed line) Ag-Pd alloy at 1400K in j/mol.

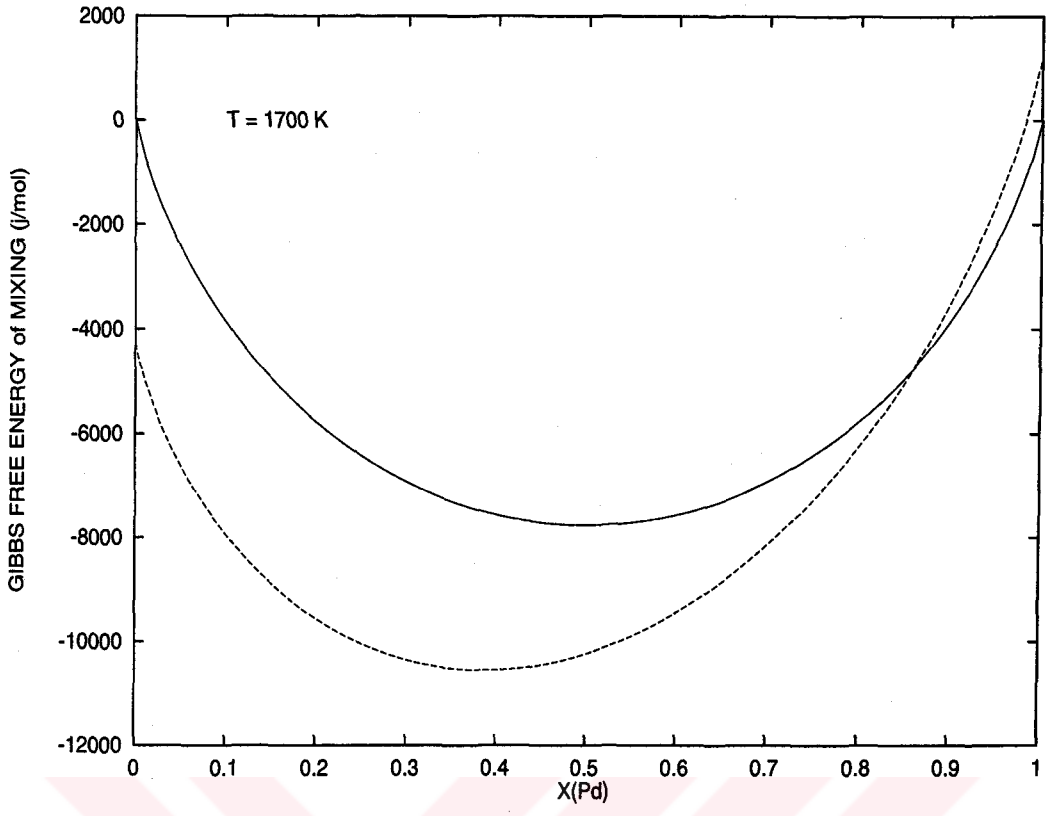

Figure 7.53: Gibbs free energy of mixing of solid (solid line) and liquid (dashed line) Ag-Pd alloy at 1700K in j/mol.

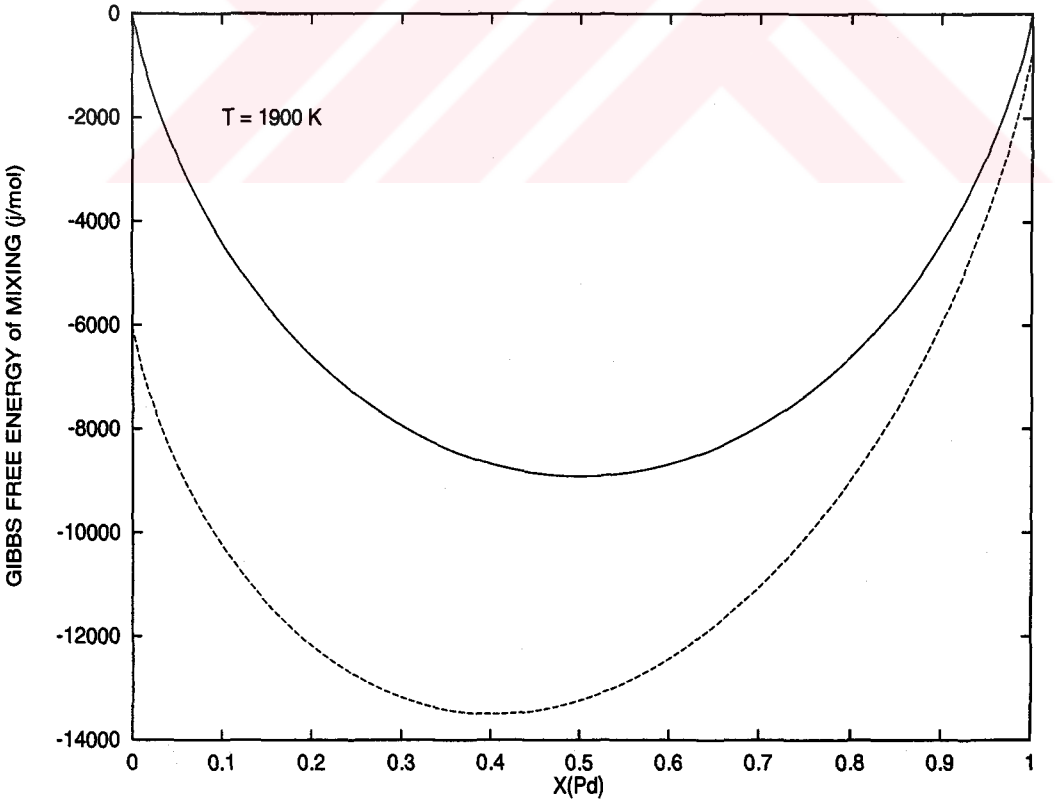

Figure 7.54: Gibbs free energy of mixing of solid (solid line) and liquid (dashed line) Ag-Pd alloy at 1900K in j/mol.

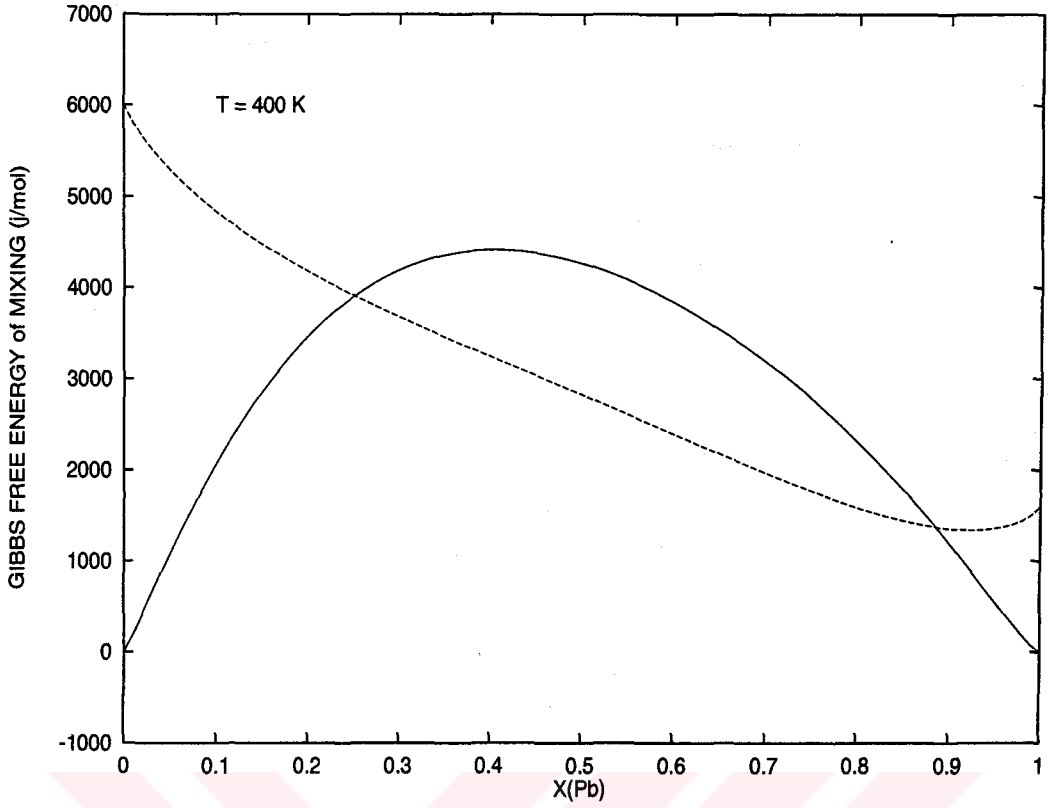

Figure 7.55: Gibbs free energy of mixing of solid (solid line) and liquid (dashed line) Ag-Pb alloy at 300K in j/mol.

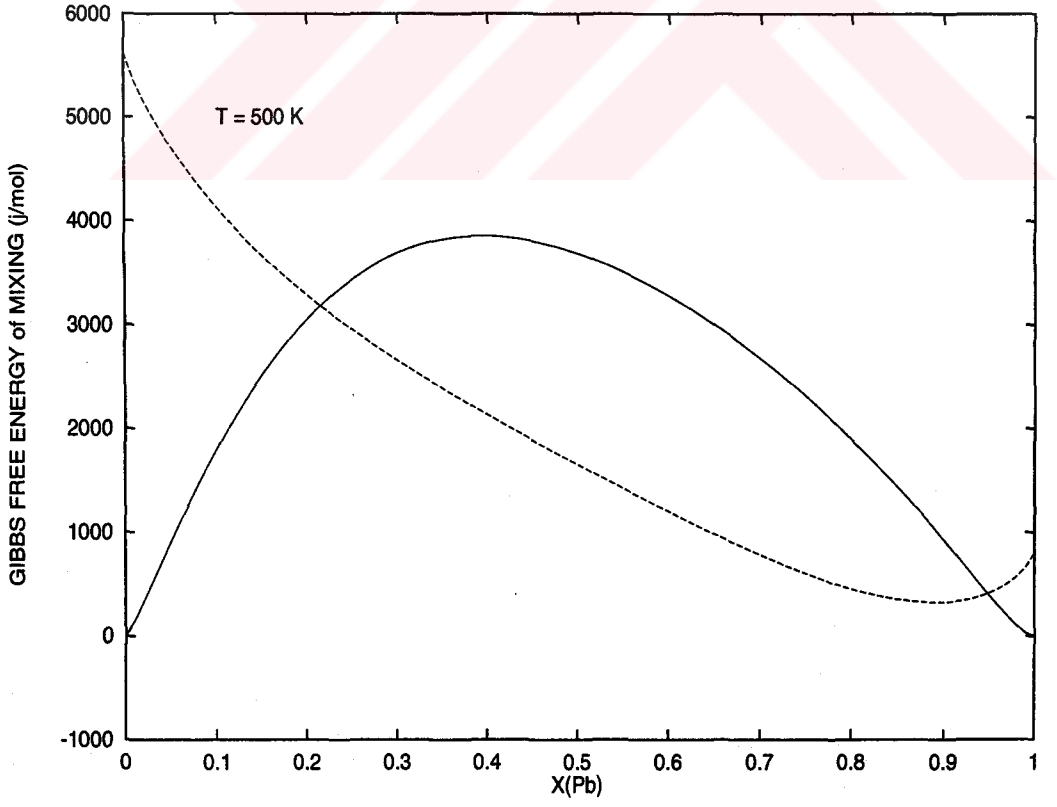

Figure 7.56: Gibbs free energy of mixing of solid (solid line) and liquid (dashed line) Ag-Pb alloy at 375K in j/mol.

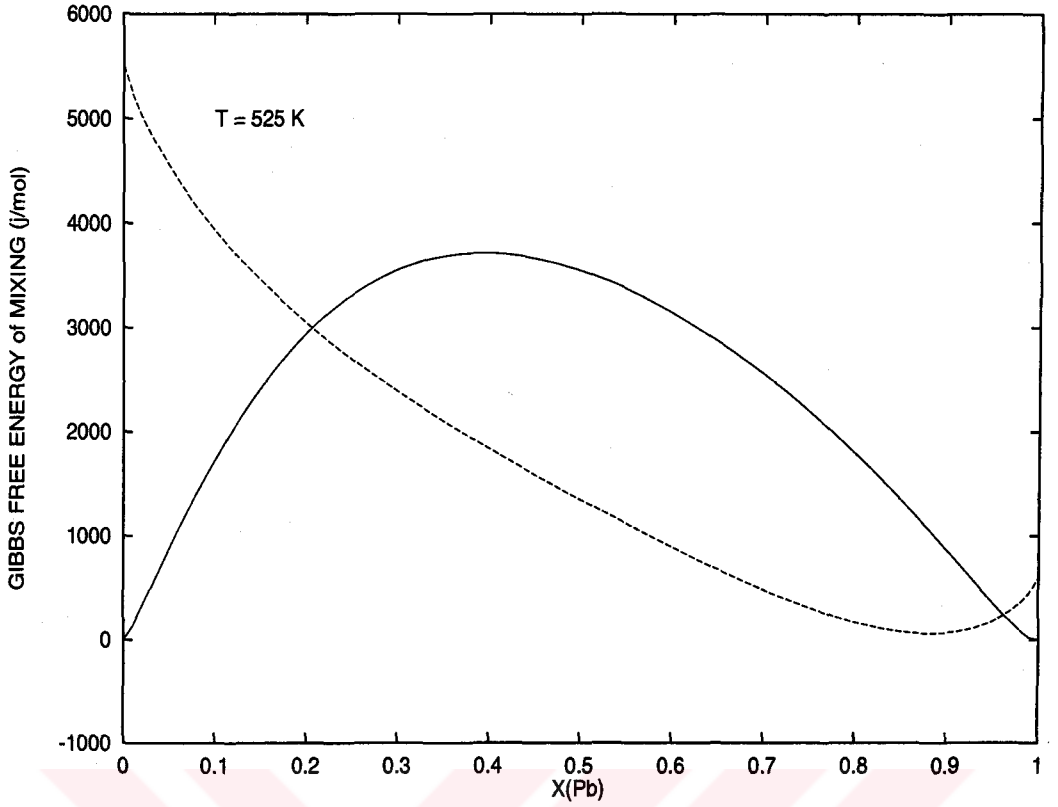

Figure 7.57: Gibbs free energy of mixing of solid (solid line) and liquid (dashed line) Ag-Pb alloy at 400K in j/mol.

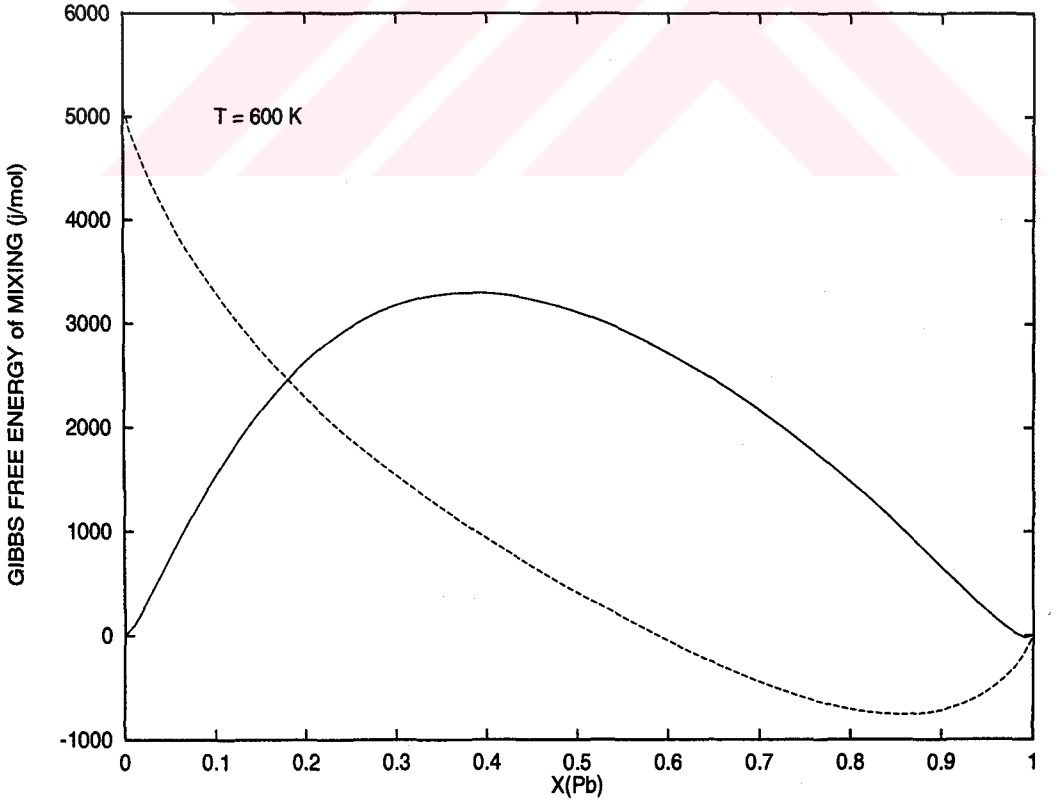

Figure 7.58: Gibbs free energy of mixing of solid (solid line) and liquid (dashed line) Ag-Pb alloy at 600K in j/mol.

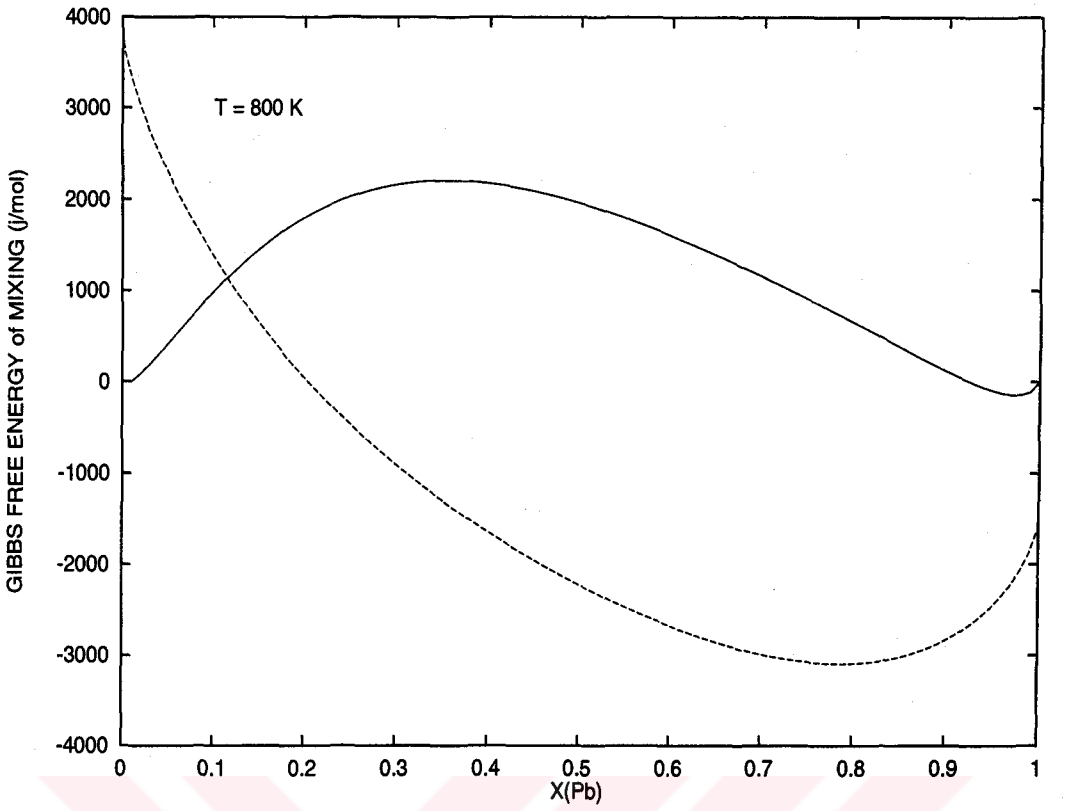

Figure 7.59: Gibbs free energy of mixing of solid (solid line) and liquid (dashed line) Ag-Pb alloy at 800K in j/mol.

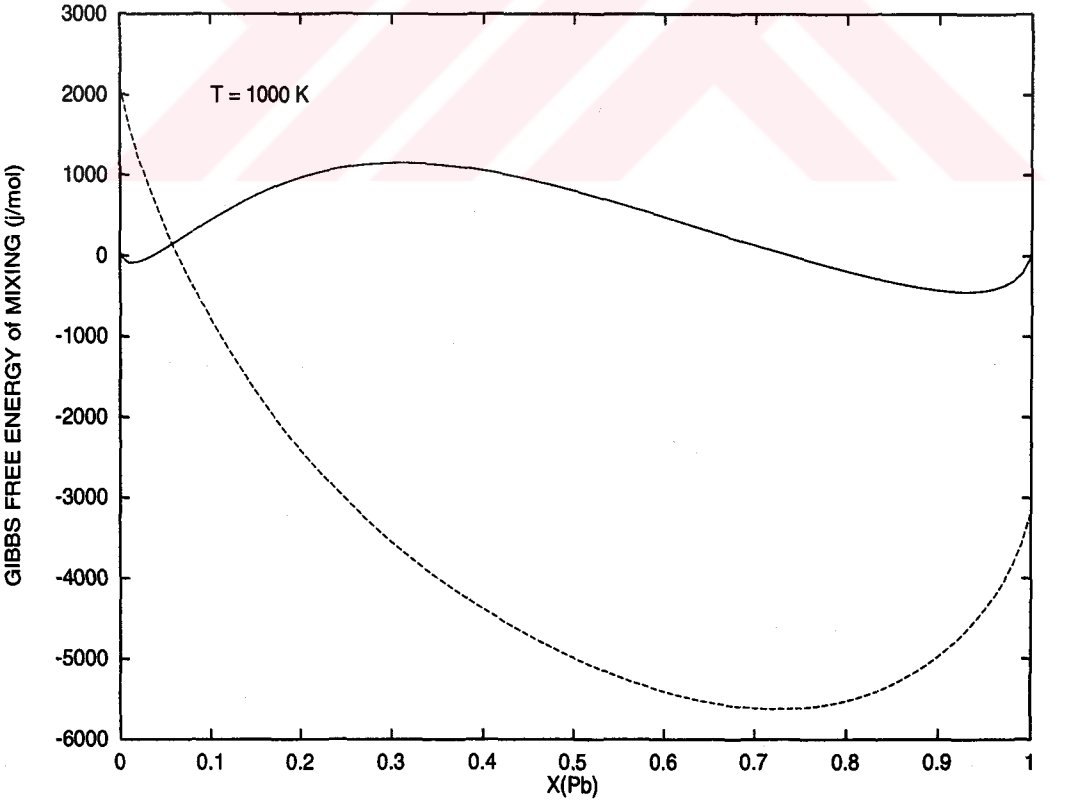

Figure 7.60: Gibbs free energy of mixing of solid (solid line) and liquid (dashed line) Ag-Pb alloy at 1000K in j/mol.

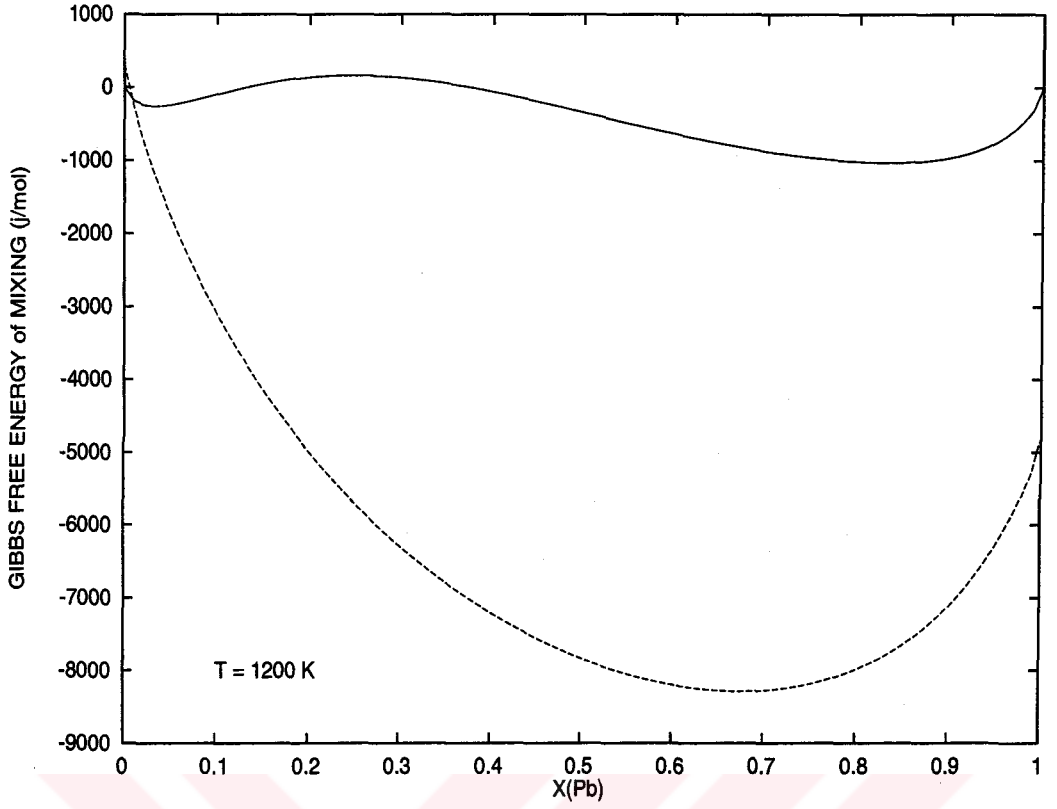

Figure 7.61: Gibbs free energy of mixing of solid (solid line) and liquid (dashed line) Ag-Pb alloy at 1200K in j/mol.

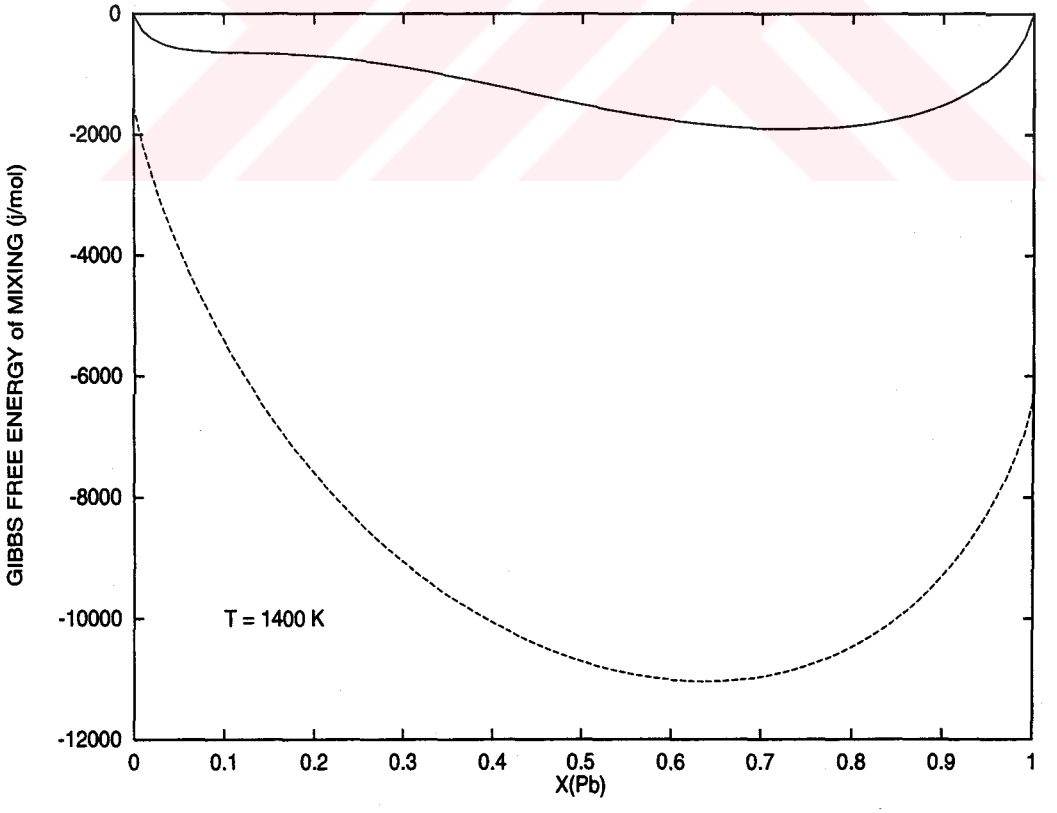

Figure 7.62: Gibbs free energy of mixing of solid (solid line) and liquid (dashed line) Ag-Pb alloy at 1400K in j/mol.

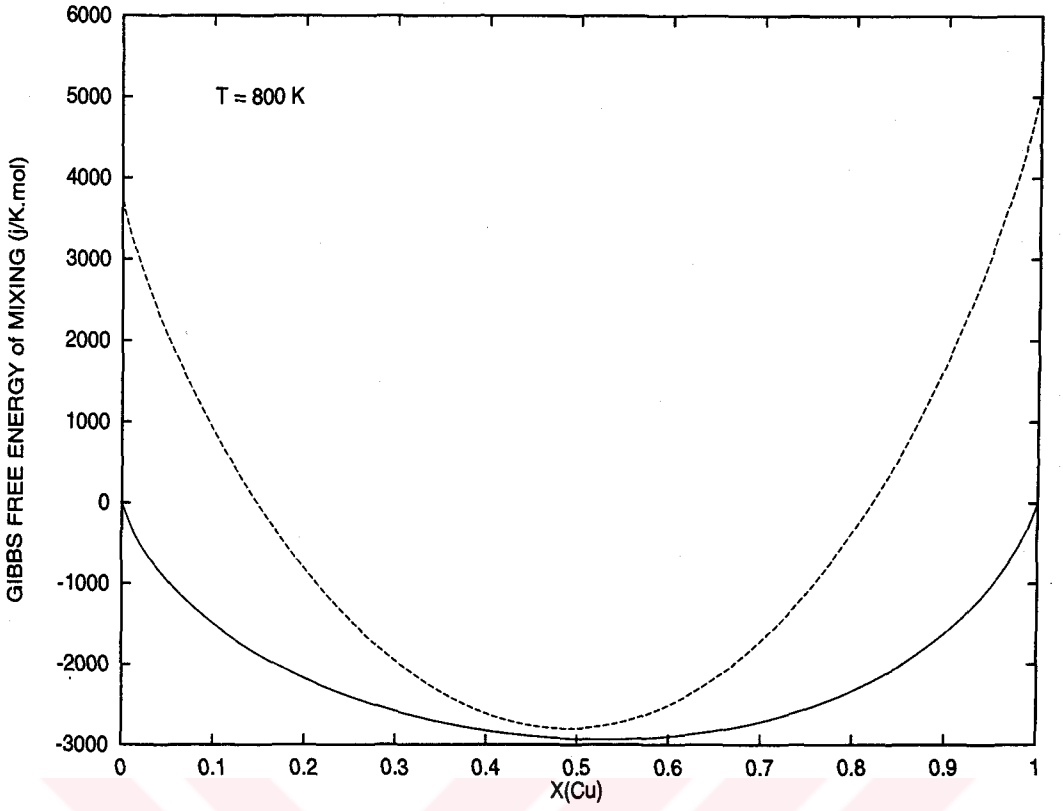

Figure 7.63: Gibbs free energy of mixing of solid (solid line) and liquid (dashed line) Ag-Cu alloy at 800K in j/mol.

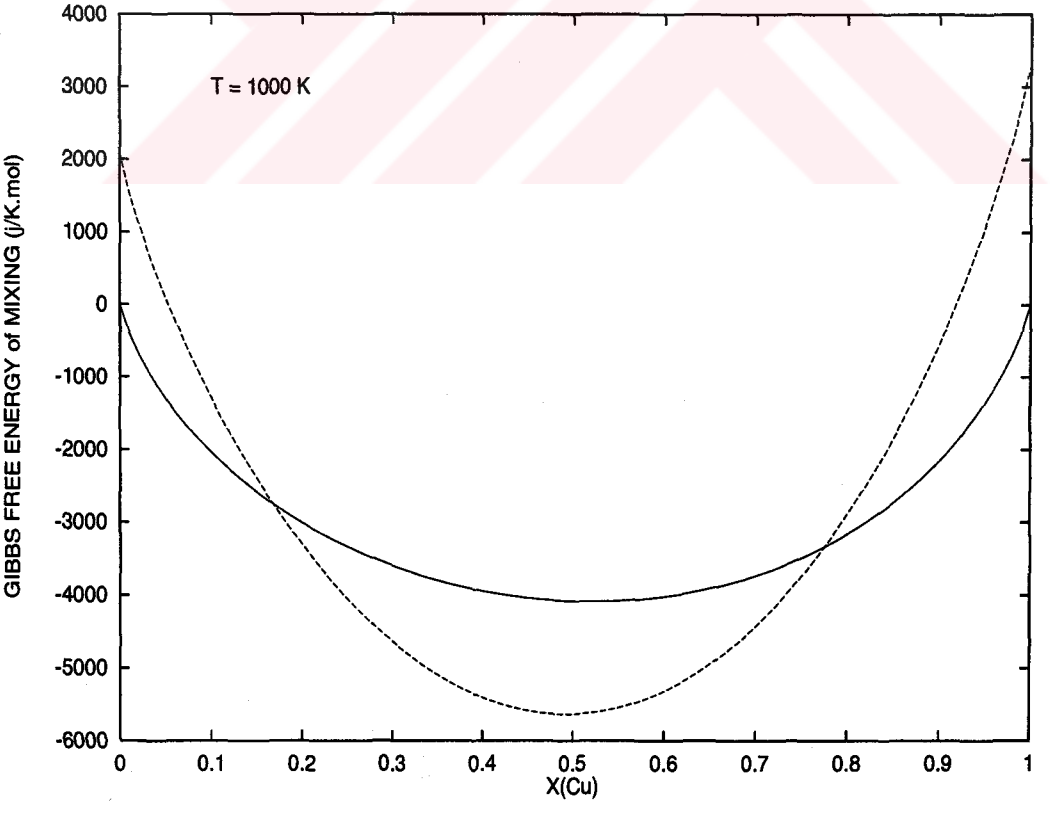

Figure 7.64: Gibbs free energy of mixing of solid (solid line) and liquid (dashed line) Ag-Cu alloy at 1000K in j/mol.

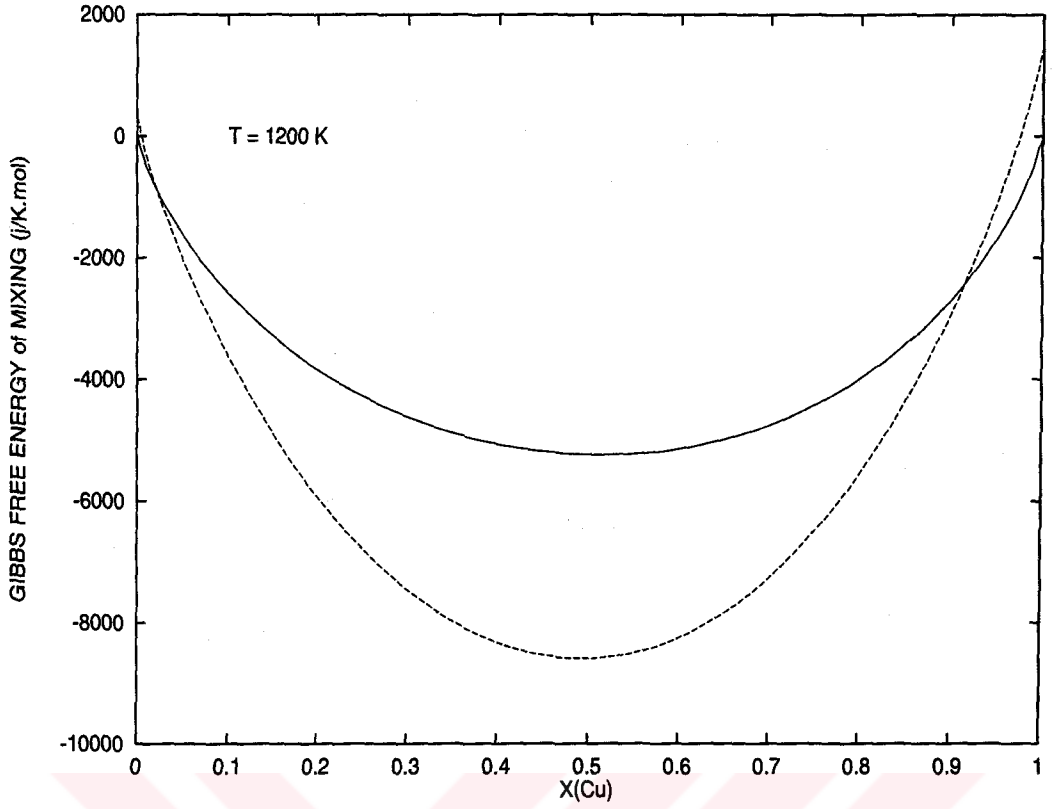

Figure 7.65: Gibbs free energy of mixing of solid (solid line) and liquid (dashed line) Ag-Cu alloy at 1200K in j/mol.

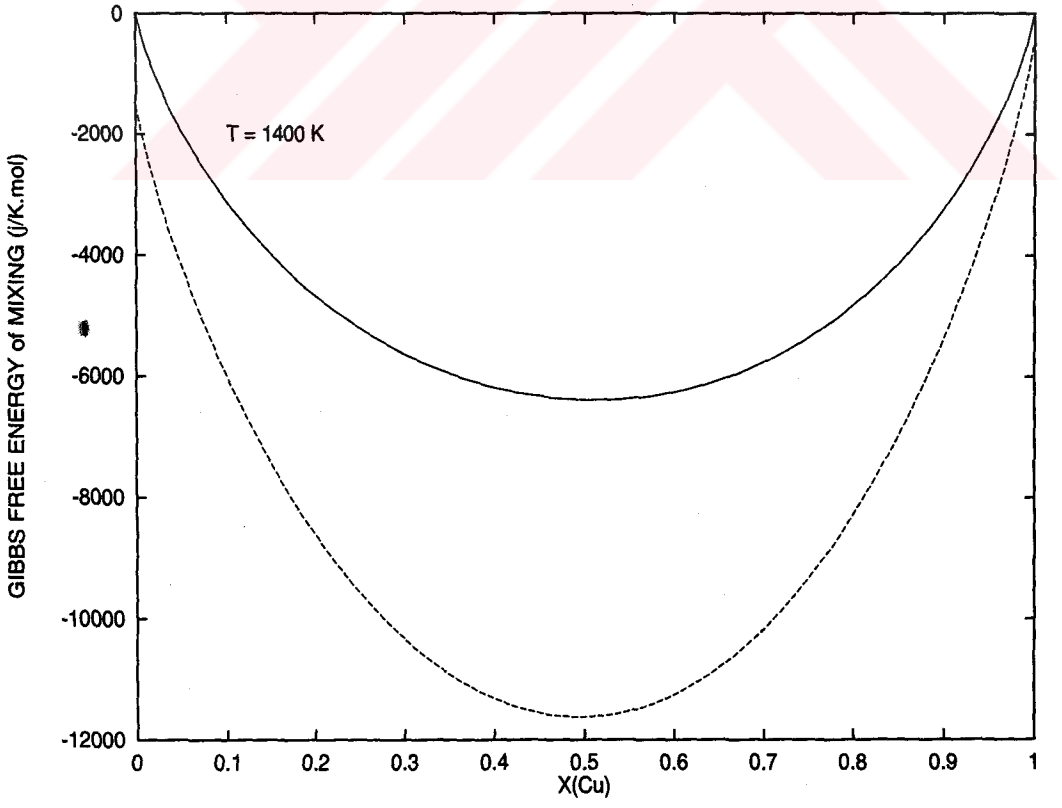

Figure 7.66: Gibbs free energy of mixing of solid (solid line) and liquid (dashed line) Ag-Cu alloy at 1400K in j/mol.

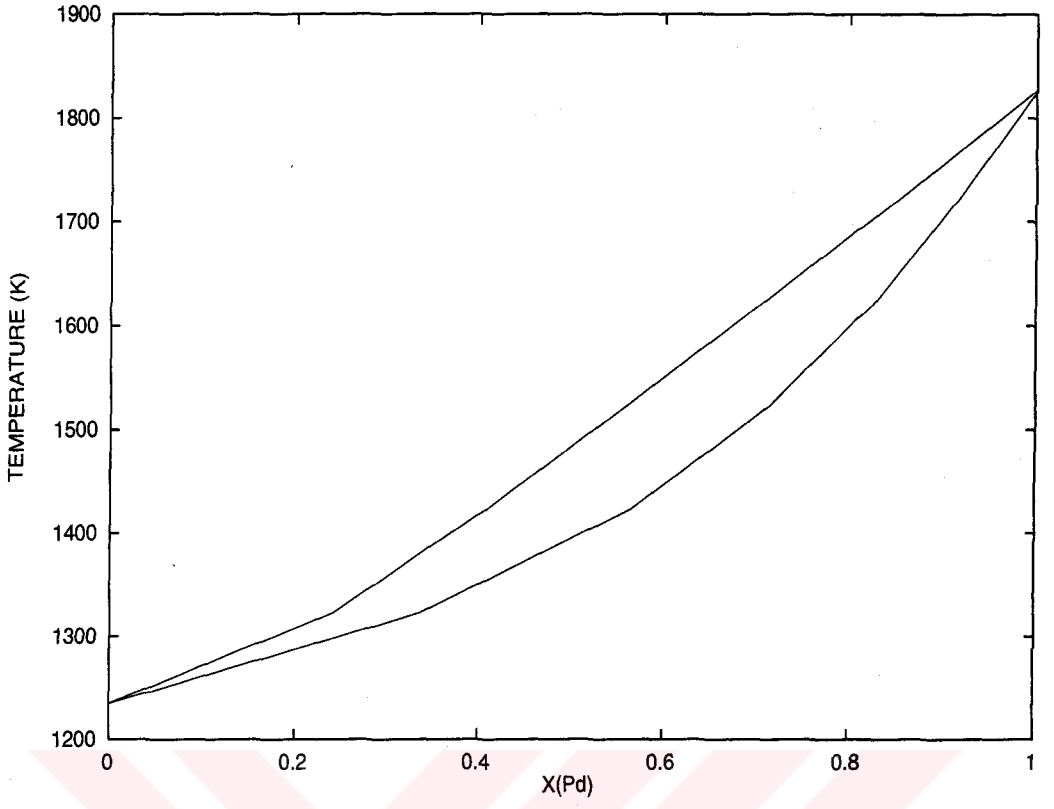

Figure 7.67: Phase diagram of Ag-Pd drawn using simulation results .

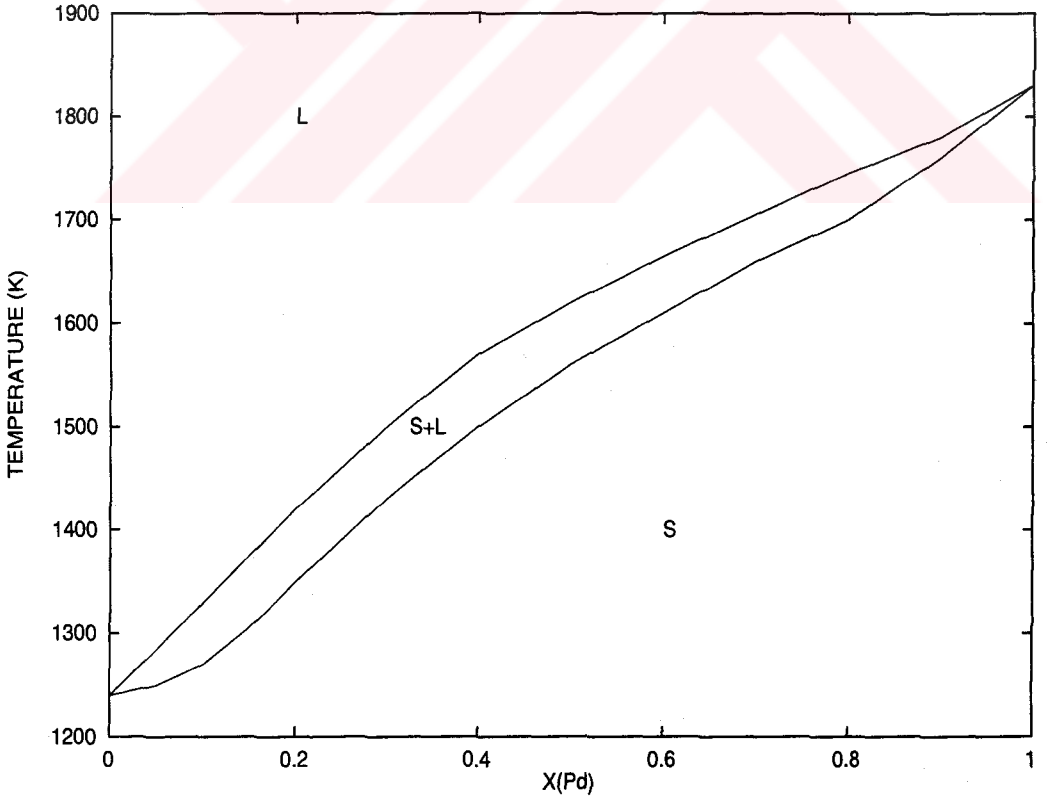

Figure 7.68: Phase diagram of Ag-Pd [37].

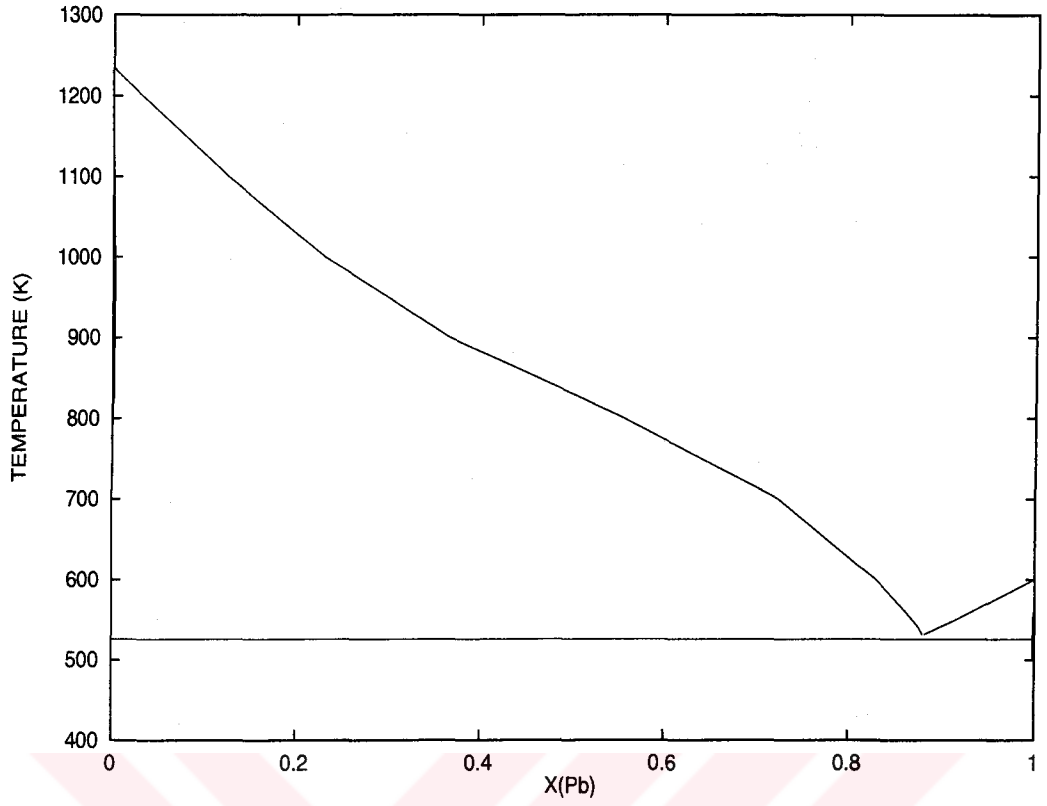

Figure 7.69: Phase diagram of Ag-Pb drawn using simulation results .

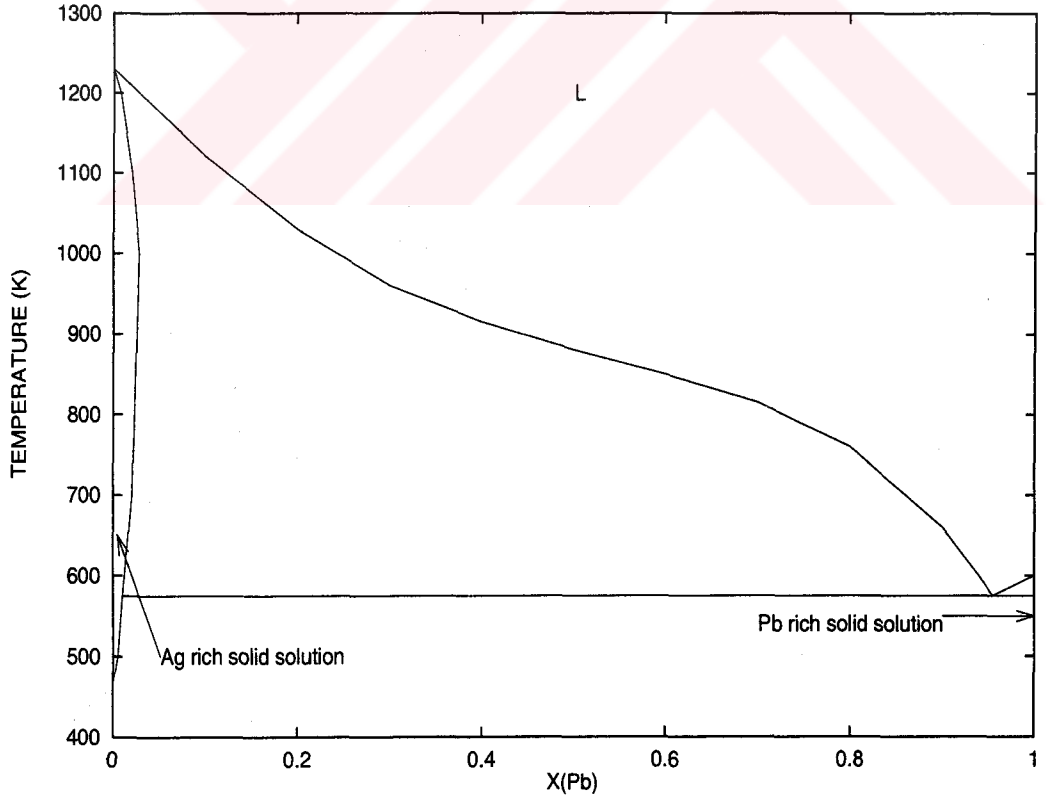

Figure 7.70: Phase diagram of Ag-Pb [37].

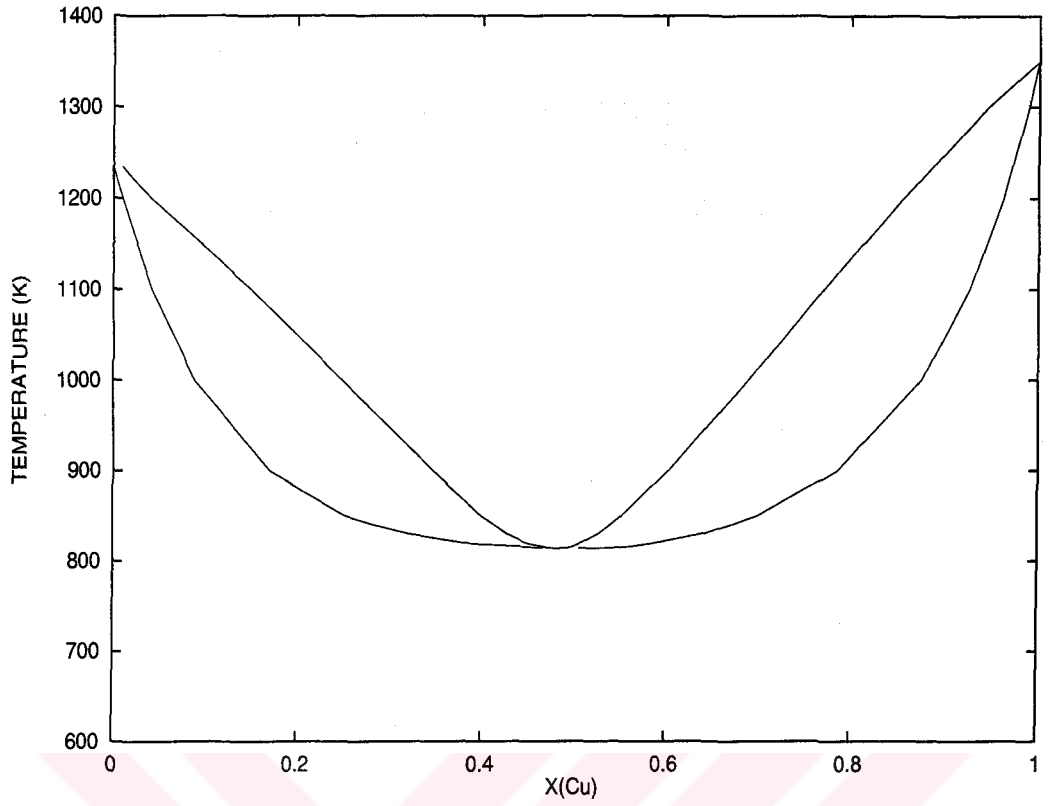

Figure 7.71: Phase diagram of Ag-Cu drawn using simulation results.

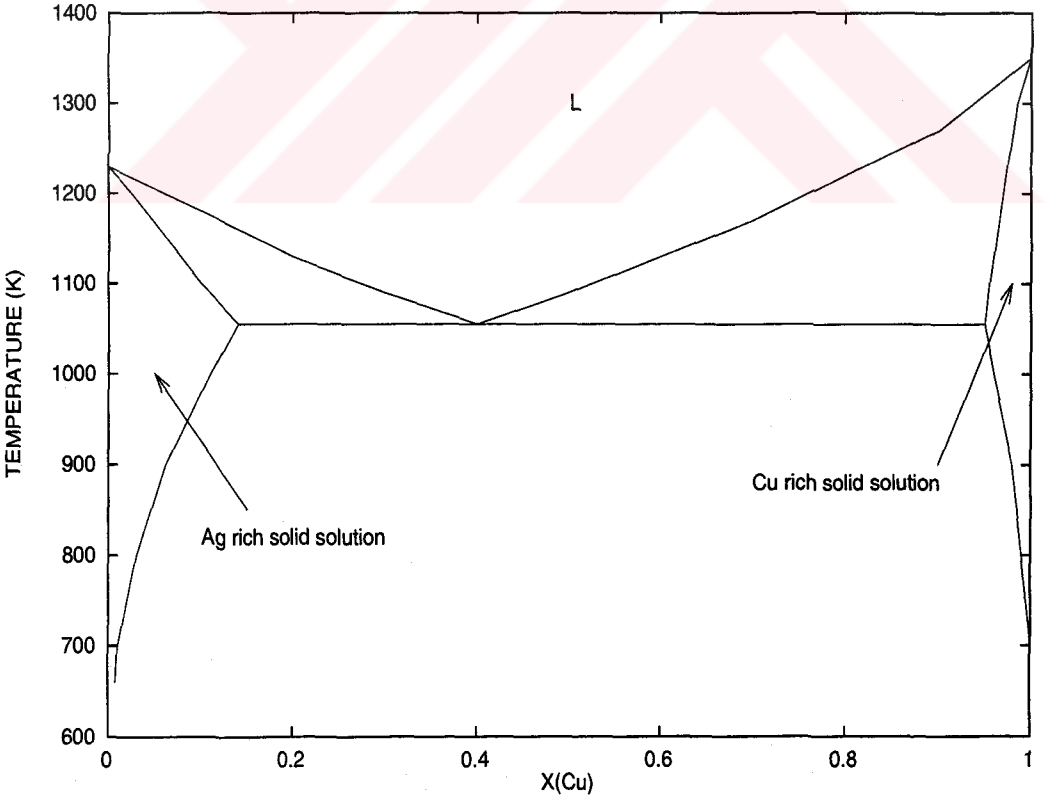

Figure 7.72: Phase diagram of Ag-Cu [39].

completely mixes in solid form. At about 825K liquid curve touches solid curve and after that temperature the alloy starts to melt. In Figures 7.64 and 7.65 we see that liquid phase appears at 1000K and 1200K and in Figure 7.66 the alloy is completely melted at 1400K.

7.3 Conclusion

In this thesis, results of computer simulation on solid and liquid forms of Ag-Pd, Ag-Pb and Ag-Cu are presented. These data and the simulation strategy will be very useful in material science. The many-body empirical Sutton-Chen potential is used to present the interactions of 500 number of fcc metal atoms that mix randomly. In order to simulate the ordinary experimental conditions (constant pressure, constant temperature) TPN MD is used. System is thermalized through the use of (constant enthalpy, constant pressure) HPN MD.

The density, volume, enthalpy and potential energy values and radial distribution functions giving the structure of the system have been examined as functions of temperature and concentration. The solid liquid phase transition can be seen in the figures. The phase diagrams are obtained in order to get more information about the miscibility of these alloys in solid and liquid forms.

The parameters of the Sutton-Chen potential in Table 3.1 used in these simulations are for the pure metals with potential cut-off radius of 2 lattice parameters [24]. This potential has given good results for pure solid metals [33]. For alloys, we have just used the combination rule for the parameters [23] [35]. Third derivatives of this potential are continuous and the continuity of

the third derivatives is essential in modeling the thermodynamic properties of these metals at high temperatures [42].

Information about the structure of these alloys are given in terms of radial distribution functions. This is a correct choice in studying solid and liquid forms of these alloys. The radial distribution functions presented at selected temperatures indicate that fcc structure is preserved in solid form. Solid to liquid transition behaviour is predicted correctly and at higher temperatures functions have the expected shape for liquids.

We have found the density values a little less than from the experimental values but this difference is not too much. Deviation from the experimental density values is about 4%. In fact our simulated lattice distances are about 1% more than experimental values at room temperature. Source of this error may be due to the Sutton-Chen potential length parameter 'a' in Table 3.1.

Although we did not find the exact melting temperatures of the metals, we can see in the Figures 7.5 to 7.28 that these values differ less than 100K from the corresponding experimental values. This again depends on the potential used in the simulations. Also Figures 7.35, 7.36, 7.37 and 7.38 show that the simulated enthalpy of melting values differ from experimental values. Simulated and experimental (in parenthesis) enthalpy of melting values of Ag, Pd, Pb and Cu are about 13.9 (11.3), 16.1 (17.6), 6.4 (4.8) and 9.4 (13.1) kj/mol, respectively. The differences may be due to the potential depth which depend on the energy parameter ϵ in Table 3.1. However, our simulations give good results of enthalpy values of solid forms of these alloys (Figures 7.35, 7.36, 7.37 and 7.38).

Our simulation results for enthalpy of mixing (Figures 7.39 to 7.50) predict reasonable heats of formation for these alloys. For the Ag-Pb alloy sign of the enthalpy of mixing is in agreement with experiment both in the solid and liquid forms. Especially for solid Ag-Pb, simulation values are in excellent agreement with experiment. For the solid alloy Ag-Pd, sign of the enthalpy of mixing is positive while experiment predicts a negative sign. For the liquid form of this alloy simulation gives positive values while experiment shows positive value after 60% of Pd. For the alloy of Ag-Cu simulation results agrees with experiment only for the solid case.

The enthalpy of mixing is sensitive to local relaxation [42]. Relaxation time is related to the computer power. Our relaxations were around 40 ps. For the solid solutions, the enthalpy of mixing is also sensitive to the existence of short order which is ignored in the random alloy model.

Metals and alloys form grain structures. Especially when alloy is a heterogeneous solution, grains can contain different concentrations of metals. For example if we look at the phase diagram of Ag-Cu alloy in Figure 7.72, at 0.4 concentration of Cu and at 900K the alloy is a mixture of 63% Ag0.94Cu0.06 solid alloy and 37% Ag0.14Cu0.86 solid alloy which is not observed in our phase diagram .

We can see the effects of this in the formation of phase diagrams. Since simulation does not have the ability to form grain structured alloy with two phases together, it will have two choices: the atoms will mix or not. The difference between the shapes of experimental and simulated phase diagrams of Ag-Cu in Figures 7.71 and 7.72 is due to this fact. Our simulations completely

mixes the Ag and Cu atom while actually they are miscibile up to some extend. Since we cannot see clearly the region of Ag rich and Pb rich solid alloys in the phase diagram in Figure 7.69, we can say that our simulations do not mix Ag and Pb atoms completely. This is also clear in Figure 7.56. Gibbs free energies of this alloy at 500K are both positive. But Pb is miscibile in solid Ag up to some concentration between about 470K and 1220K in Figure 7.70 and this region is not seen in the simulated phase diagram in Figure 7.69.

Finally, we can say that our simulation results give successfully the mixing behaviour of the Ag-Pd and Ag-Pb alloys. The differences between the shapes of the solidius and liquidus lines in experimental and simulated phase diagrams is due to the differences between the experimental and simulated melting temperatures of the metals.

REFERENCES

[1] S. Pal, K. A. Fichthorn, Chemical Engineering Journal. **74**, 77 (1999).

[2] M. I. Mendelev, Journal of Non-Crystalline Solids, 232-234, 560 (1998).

[3] A. N. Al-Rawi, A. Kara, T. S. Rahman, Surface Science, **446**,17 (2000).

[4] M. Grujicic, P. Dang, Material Science and Engineering, **A205**, 153 (1996).

[5] M. I. Mendelev, Physica, **40 B**, 262 (1999).

[6] A. A. Baumketner, Ya. Chushak, Journal of Non-Crystalline Solids, **354**, 250 (1999).

[7] X. Liu, H.Liu, J. Dong, X. Xie, Scripta Mater., **42**,189 (2000).

[8] W. C. Morrey, L.T. Wille, Material Science and Engineering, **B37**, 181 (1996).

[9] M. Canales, A. Giró, J. Á. Padró, Journal of Non-Crystalline Solids, **907**, 205 (1996).

[10] B. José, C. Cabral, J. L. Martins, Journal of Molecular Structure (Theochem), **463**, 145 (1999).

[11] Meunier G., Treglia B., Legrand R., Tetot B., Aufray J.,M. Gay, Applied Surface Science, **219**, 162 (2000).

[12] R. C. Longo, C. Rey, L. J. Gallego, Surface Science, **459**, 441 (2000).

[13] T. J. Colla, H. M. Urbassek, R. S. Averback, Nuclear Instruments and Methods in Physics Research, **B 153**, 369 (1999).

[14] T. Ohkubo, Y. Hirotsu, Material Science and Engineering, **A217/218**, 388 (1996).

[15] D.J. Bacon, F. Gao, Yu.N. Osetsky, Journal of Nuclear Materials, **276**, 1 (2000).

[16] M. M. G. Alemany, M. Calleja, C. Rey, L. J. Gallego , J. Casas, L. E. González, Journal of Non-Crystalline Solids, **53**, 250 (1999).

[17] T. Aihara Jr., Y. Kawazoe, T. Masumoto, Journal of Non-Crystalline Solids, **875** 205, (1996).

[18] M. P. Allen and d. J. Tildeslay, Computer Simulation of Liquids, Clarendon Press, Oxford (1987).

[19] W. G. Hoover, Molecular Dynamics, Springer-Verlag (1986).

[20] D. C. Rapaport, The Art of Molecular Dynamics Simulation, Cambridge University Press (1995).

[21] D. W. Heermann, Computer Simulation Methods in Theoretical Physics, Springer Heidelberg (1990).

[22] L. Verlet, Phys. Rev., **159**, 98 (1967).

[23] G. Dereli, T. Çağın, M. Uludoğan, M. Tomak, Phil. Mag. Let., **75**, 209 (1997).

[24] H. Rafii-Tabar, A. P. Sutton, Phil. Mag. Lett., **63**, 217 (1991).

[25] A. P. Sutton, J. Chen, Phil. Mag. Lett., **61**, 139 (1990).

[26] J. M. Haile, Molecular Dynamics Simulation Elementary Methods, John Willey & Sons, Inc., (1991).

[27] R. K. Pathria, Statistical Mechanics, Butterworth-Heinemann (1996).

[28] S. Nosé, J. Chem. Phys., **81**, 511 (1984).

[29] H.C. Andersen, J.Chem.Phys., **72**, 2384 (1980).

[30] M. Parinello and A. Rahman, Phys. Rev. Lett., **15**, 1196 (1980).

[31] W. G. Hoover, Phys. Rev. A **31**, 1965 (1985).

[32] T. Çağın and B.M. Pettitt, Mol. Phys., **72**, 169 (1991); Mol. Sim., **6**, 5 (1991).

[33] G. Dereli, M. Uludoğan, M. Tomak, Phys. Rev., **B 59**, 3468 (1999).

[34] T. Çağın, J. R. Ray, Phys. Rev. A **37**, 247 (1988); 4510 (1988).

[35] Y. Qi, T. Çağın, Y. Kimura, W. A Goddard, Phys. Rev., **B 59**, 3527 (1999).

[36] P. Gordon, Princibles of Phase Diagrams in Materials System, McGraw-Hill (1968).

[37] I. Karakaya, W. T. Thompson, Bulletin of Alloy Phase Diagram, **9**, 237 (1988); **8**, 326 (1987).

[38] I. Barin, Thermodynamical Data of Pure Substances, **1**, **2** (1989).

[39] R. Hultgren, R. L. Orr, P. D. Anderson, K. K. Kelley, Selected Values of Thermodynamic Properties of Metals and Alloys, John Willey & Sons, Inc., (1963).

[40] Metals Handbook, Properties and Selection: Nonferrous Alloys and Pure Metals, **2** (1979).

[41] I. Barın, O. Knacke, O. Kubaschewski, Thermodynamical Properties of Inorganic Substances, Springer-Verlag, Berlin (1977).

[42] G. J. Ackland, V. Vitek, Phys. Rev., **B 41**, 10324 (1990).

[43] M. J. Assael, J. P. M. Trusler, T. F. Tsolakis, Thermophysical Properties of Fluids, Imperial College Press (1996).

[44] W. T. Thompson, A. D. Pelton, C. W. Bale, F*A*C*T Facility for the Analysis of Chemical Thermodynamics, McGill University, Montreal (1977).